

Suitably impressive thesis title



Your Name

Your College

University of Oxford

A thesis submitted for the degree of

Doctor of Philosophy

Michaelmas 2014

This thesis is dedicated to
someone
for some special reason

Acknowledgements

Personal

This is where you thank your advisor, colleagues, and family and friends.

 Lorem ipsum dolor sit amet, consectetur adipiscing elit. Vestibulum feugiat et est at accumsan. Praesent sed elit mattis, congue mi sed, porta ipsum. In non ullamcorper lacinia. Quisque volutpat tempus ligula ac ultricies. Nam sed erat feugiat, elementum dolor sed, elementum neque. Aliquam eu iaculis est, a sollicitudin augue. Cras id lorem vel purus posuere tempor. Proin tincidunt, sapien non dictum aliquam, ex odio ornare mauris, ultrices viverra nisi magna in lacinia. Fusce aliquet molestie massa, ut fringilla purus rutrum consectetur. Nam non nunc tincidunt, rutrum dui sit amet, ornare nunc. Donec cursus tortor vel odio molestie dignissim. Vivamus id mi erat. Duis porttitor diam tempor rutrum porttitor. Lorem ipsum dolor sit amet, consectetur adipiscing elit. Sed condimentum venenatis consectetur. Lorem ipsum dolor sit amet, consectetur adipiscing elit.

 Aenean sit amet lectus nec tellus viverra ultrices vitae commodo nunc. Mauris at maximus arcu. Aliquam varius congue orci et ultrices. In non ipsum vel est scelerisque efficitur in at augue. Nullam rhoncus orci velit. Duis ultricies accumsan feugiat. Etiam consectetur ornare velit et eleifend.

 Suspendisse sed enim lacinia, pharetra neque ac, ultricies urna. Phasellus sit amet cursus purus. Quisque non odio libero. Etiam iaculis odio a ex volutpat, eget pulvinar augue mollis. Mauris nibh lorem, mollis quis semper quis, consequat nec metus. Etiam dolor mi, cursus a ipsum aliquam, eleifend venenatis ipsum. Maecenas tempus, nibh eget scelerisque feugiat, leo nibh lobortis diam, id laoreet purus dolor eu mauris. Pellentesque habitant morbi tristique senectus et netus et malesuada fames ac turpis egestas. Nulla eget tortor eu arcu sagittis euismod fermentum id neque. In sit amet justo ligula. Donec rutrum ex a aliquet egestas.

Institutional

If you want to separate out your thanks for funding and institutional support, I don't think there's any rule against it. Of course, you could also just remove the subsections and do one big traditional acknowledgement section.

 Lorem ipsum dolor sit amet, consectetur adipiscing elit. Ut luctus tempor ex at pretium. Sed varius, mauris at dapibus lobortis, elit purus tempor neque,

facilisis sollicitudin felis nunc a urna. Morbi mattis ante non augue blandit pulvinar. Quisque nec euismod mauris. Nulla et tellus eu nibh auctor malesuada quis imperdiet quam. Sed eget tincidunt velit. Cras molestie sem ipsum, at faucibus quam mattis vel. Quisque vel placerat orci, id tempor urna. Vivamus mollis, neque in aliquam consequat, dui sem volutpat lorem, sit amet tempor ipsum felis eget ante. Integer lacinia nulla vitae felis vulputate, at tincidunt ligula maximus. Aenean venenatis dolor ante, euismod ultrices nibh mollis ac. Ut malesuada aliquam urna, ac interdum magna malesuada posuere.

Abstract

Your abstract text goes here. Check your departmental regulations, but generally this should be less than 300 words. See the beginning of Chapter ?? for more.

 Lorem ipsum dolor sit amet, consectetur adipiscing elit. Pellentesque sit amet nibh volutpat, scelerisque nibh a, vehicula neque. Integer placerat nulla massa, et vestibulum velit dignissim id. Ut eget nisi elementum, consectetur nibh in, condimentum velit. Quisque sodales dui ut tempus mattis. Duis malesuada arcu at ligula egestas egestas. Phasellus interdum odio at sapien fringilla scelerisque. Mauris sagittis eleifend sapien, sit amet laoreet felis mollis quis. Pellentesque dui ante, finibus eget blandit sit amet, tincidunt eu neque. Vivamus rutrum dapibus ligula, ut imperdiet lectus tincidunt ac. Pellentesque ac lorem sed diam egestas lobortis.

 Suspendisse leo purus, efficitur mattis urna a, maximus molestie nisl. Aenean porta semper tortor a vestibulum. Suspendisse viverra facilisis lorem, non pretium erat lacinia a. Vestibulum tempus, quam vitae placerat porta, magna risus euismod purus, in viverra lorem dui at metus. Sed ac sollicitudin nunc. In maximus ipsum nunc, placerat maximus tortor gravida varius. Suspendisse pretium, lorem at porttitor rhoncus, nulla urna condimentum tortor, sed suscipit nisi metus ac risus.

 Aenean sit amet enim quis lorem tristique commodo vitae ut lorem. Duis vel tincidunt lacus. Sed massa velit, lacinia sed posuere vitae, malesuada vel ante. Praesent a rhoncus leo. Etiam sed rutrum enim. Pellentesque lobortis elementum augue, at suscipit justo malesuada at. Lorem ipsum dolor sit amet, consectetur adipiscing elit. Praesent rhoncus convallis ex. Etiam commodo nunc ex, non consequat diam consectetur ut. Pellentesque vitae est nec enim interdum dapibus. Donec dapibus purus ipsum, eget tincidunt ex gravida eget. Donec luctus nisi eu fringilla mollis. Donec eget lobortis diam.

 Suspendisse finibus placerat dolor. Etiam ornare elementum ex ut vehicula. Donec accumsan mattis erat. Quisque cursus fringilla diam, eget placerat neque bibendum eu. Ut faucibus dui vitae dolor porta, at elementum ipsum semper. Sed ultrices dui non arcu pellentesque placerat. Etiam posuere malesuada turpis, nec malesuada tellus malesuada.

Contents

List of Figures	xiii
List of Abbreviations	xxi
1 Introduction	1
1.1 Motivation	1
1.2 Contribution	3
2 Robustness of electron charge shuttling: Architectures, pulses, charge defects and noise thresholds	5
2.1 Introduction	5
2.2 Description of the Shuttling Device	6
2.3 Voltage profiles for conveyor-belt Shuttling	11
2.4 Numerical Simulations	13
2.5 Performance metrics	15
2.6 Noiseless Shuttling	17
2.7 Sensitivity to Johnson-Nyquist noise	18
2.8 Sensitivity to Charge Defects	24
2.9 Advanced non-adiabatic ultra-fast shuttling	28
2.10 Implications for coherent qubit transport	30
2.11 Conclusions	32
3 Noise-aware Time-optimal Quantum Control	41
3.1 Introduction	41
3.2 Time Optimisation in Quantum Optimal Control	43
3.2.1 Chopped Random Basis (CRAB)	43
3.2.2 Noisy Simulation of CRAB	45
3.2.3 Implementation of Time-optimised CRAB	48
3.3 Numerical Simulations	49
3.3.1 State-to-State Transfer	49
3.3.2 Gate Compilation	52
3.4 Discussion	55
3.5 Conclusion	57

Appendices

A Appendix of Robustness of electron charge shuttling: Architectures, pulses, charge defects and noise thresholds	63
A.1 Details of Conveyor-Belt Shuttling	64
A.1.1 Energy Evolution	64
A.1.2 Two Possible Phase Variations	64
A.1.3 The Effect of Finite Extent of the QD in the perpendicular direction	68
A.1.4 The Comparison of 1D and 2D Simulations for the Shuttling	70
A.2 Details of Numerical Simulations	70
A.2.1 Boundary Conditions	70
A.2.2 Numerical Methods	73
A.2.3 Definition of Model	74
A.2.4 Convergence Studies of the model	78
A.2.5 Numerical Precision	79
A.2.6 Lumped Element Model of a Voltage Source connected to Clavier Gates	80
A.2.7 Generation of Johnson-Nyquist Noise	81
A.3 Additional Results of the Conveyor-Belt Mode Shuttling	81
A.3.1 Noise-free Shuttling: Target Speed	81
A.3.2 Sensitivity to step-changes in voltage control	81
A.3.3 Sensitivity to Classical Johnson Nyquist Noise	86
A.3.4 Speed Vs. Adiabaticity	87
A.3.5 Sensitivity to Charge Defects: Two Defects of Varying Separations.	91
A.4 Results of Advanced Non-Adiabatic Ultra-fast shuttling	91
B Appendix of Noise-aware Time-optimal Quantum Control	99
B.1 Commutation between unitary and dissipative part	100
B.2 Commutation and Fidelity of Pauli channel	101
B.2.1 Pauli channel from Lindblad master equation	101
B.2.2 Transformation between Pauli transfer matrix and Pauli channels	103
B.2.3 Example: dephasing noise	104
B.2.4 Group channels	105
B.2.5 Example: Depolarising channel	107
B.2.6 Example: Two-qubit Dipole-Dipole Noise Channel	108
B.2.7 The Application of Noise channels for Gate Compilation	108
B.3 Choi States	109

B.4 Numerical Simulations	110
B.4.1 Implementation of CRAB and TCRAB	110
B.4.2 Hyper-parameters	114
B.5 Additional Numerics	115
B.6 Oscillation of Optimised Fidelity	115
B.7 Identity Test	118

List of Figures

- 2.1 Conceptual illustration of the conveyor-belt shuttling device studied in this paper. The electrons are confined near a silicon-oxide interface below a periodic array of gates to which external potentials can be applied via voltage lines A, B and C. In this paper we consider devices with three repeating electrodes, as depicted, as well as four [1] and five. 7
- 2.2 Illustration of (a) the shuttling device in 3D and (b) its cross-section in the xz plane. The yellow boxes are clavier gates with width and height of 30 nm along the x and z direction and the length of 75 nm along the y direction. The gap between the gates is 5 nm. The size of this unit cell with three gates is 105 nm along the shuttling direction, i.e the x -direction. The clavier gates are implanted in the oxide layer (blue). Below the oxide layer, there is a Si layer (magenta), whose base is grounded. 8
- 2.3 Illustration of the voltage pulses applied to the gates in conveyor-belt shuttling for three gates per unit cell, i.e. $N = 3$. (a) Every 3rd gate is connected to the same voltage source (denoted as red, green and blue lines). (b) The three independent pulses are sinusoidal with $2\pi/3$ phase difference. (c) The position, x , of the potential minimum as a function of time when the average shuttling speed is 10 m/s. The lines correspond to different choices of phase variation, $\phi(t)$: linearly varying phase $\phi(t) = k \cdot t$ (blue line), and phase obtained by using a look-up table, f^{-1} , $\phi(t) = f^{-1}(x(t))$ (orange line). The detailed arguments are given in Appendix A.1.2. (d) The resulting time-evolution of the potential and approximate position of the electron wave packet. The red, green, and blue boxes above denote the same clavier gates of the corresponding colour in (a) and (b). (e) Variation of the curvature at the potential minimum, κ , obtained by fitting the slice of potential energy at $y = 0$ with a quadratic function (see also the plots of the full potential in Figure 2.4). Note that panels (a),(b), and (c) relate the panels (e), (f), and (g) of Figure 2 of Langrock et al.[1]. 10

2.4	3D and contour plots of the potential energy, $V(x, y)$, generated by the gates for $N = 4$ with $A = 100$ mV. (a) 3D and (b) contour plots of the potential energy for one unit cell centred around the potential minimum when the curvature near the potential minimum, $\kappa(\phi)$, is maximum (corresponding to a potential well directly below an electrode). (c) 3D and (d) contour plots of the potential energy for one unit cell centred around the potential minimum when $\kappa(\phi)$ is a minimum (corresponding to a potential well between two electrodes).	11
2.5	Illustration of the definition of the loss probability as the integrated probability density (orange line) over the shaded region ν , defined as the region outside the well in potential energy (blue line) being used to shuttle the electron.	15
2.6	The loss probability and excitation fraction for different noiseless shuttling scenarios: (a) loss probability and (b) excitation fraction as a function of voltage signal amplitude, A , for a shuttling distance of $1.4 \mu\text{m}$; (c) loss probability and (d) excitation fraction as a function of target distance, D , for a signal amplitude of 100 mV. Results for different numbers of electrodes per unit cell ($N = 3, 4, 5$) are shown.	17
2.7	(a) the power spectral density, S , of the classical (blue) and quantum (orange) Johnson-Nyquist noise, and (b) random instances of classical (blue) and quantum (orange) Johnson-Nyquist noise, V_{noise} , at $T = 4$ K, and $\gamma = 10$ THz	20
2.8	Loss probability and excitation fraction: (a, b) as a function of temperature with three different cut-off frequencies, i.e. $\gamma = 10, 100, 1000$ GHz for three gates per unit cell ($N = 3$) and (c, d) as a function of cut-off frequency γ with varying number of gates per unit cell, N	22
2.9	Probability of excitation outside of the ground state (blue) and excitation fraction during the shuttling (orange) for a target distance of $1.4 \mu\text{m}$ at 10 m/s. Other parameters were set as follows: The amplitude of voltage signals was 50 mV, i.e. $A = 50$ mV, the temperature was 2 K, i.e. $T = 2$ K, and there were three gates per unit cell, i.e. $N = 3$	23
2.10	The loss probability of electron wave function with varying number of charge defects, $N_{defects}$, in the channel. Note that, for each number of charge defects, 100 random configurations of charges were simulated. Up to $N_{defects} = 4$, the loss probability remains nearly zero while we start to see cases with high loss probability with more than 6 defects present. The blue line connects the mean loss probability for each $N_{defects}$	25

2.11 Contour plots of the potential energies with varying number of charge defects: (a) one, (b) two, and (c) three. Note that, for (b) and (c), the charges were aligned in the middle of the channel to form a wall to repel the electron. The distance from the interface to the charge defects was set to 5 nm.	27
2.12 (a) The probability to remain in the instantaneous ground state of the potential formed by the gates alone for a shuttling speed of 10 m/s and varying numbers of charge defects, $N_{defects}$: one (blue), two (orange), and three (green). The electron is closest to the defects in the middle of the shuttling. Note that, for one and two charge defects, the probability decreases temporarily below 0.2 as the electron passes the defects but rises back to approximately 1; for three charge defects, shuttling fails as the probability decreases to almost zero at the end of shuttling. The distance from the interface to the charge defects was set to 5 nm. (b) The loss probability and excitation fraction of the electron wave function in the presence of two charge defects, separated by Δy , for a shuttling speed of 10 m/s. $\Delta y = 0$ corresponds to two charges at the same location, equivalent to one charge defect with twice the charge. As Δy increases the peak loss probability and excitation fraction are about 0.04 and 4 respectively.	37
2.13 The cross-section of the potential in the xz plane (at $x = 0$ nm in Figur 2.11b) in the presence of two charge defects of varying separations $\Delta y = 2, 12, 25, 30$ nm. Each defect has charge of $-e$	38
2.14 The excitation fraction with various shuttling speeds when one charge defect is present. The blue and orange lines correspond to excitation fraction when the charge defect is 2 nm and 5 nm away from the interface.	39
2.15 The illustration of snap method, where the blue line corresponds to the potential energy, the orange line corresponds to the probability density. Shaded regions were applied when instantaneous changes of the potential energy with displacement Δx were made. The grey line at the $t = 0$ panel represents the potential energy at $t < 0$. In the first panel, the potential is instantaneously shifted to the right by Δx . In the second panel, the potential is static until the wave function has evolved to the other side of the well and comes to a halt. In the last panel, the potential is shifted again to the right by the same amount, Δx . This process continues until the target distance of shuttling is achieved. The time it takes for the electron wavefunction to curl up the other side of the well depends on the local curvature, κ , at the bottom of the well.	40

3.1 The optimised infidelity reached using CRAB (blue) and TCRAB with two optimisation methods, i.e. basin-hopping (red) and bisection search (orange) for (a) entanglement generation of two capacitively coupled Josephson charge qubits; (b) state-to-state transfer from the ground state of paramagnetic phase to a ground state of ferromagnetic phase; (c) CZ gate compilation for spin qubits with SWAP control fields; (d) CZ gate compilation for spin qubits with dipole-dipole control fields. The optimal time, T_{opt} , and optimised infidelity are annotated. In (a), we have basin-hopping and the bisection method both successfully converged to the same global minimum since the cost function is convex. In (b), (c) and (d), due to the presence of oscillations, the bisection search converged to a local minimum instead. Note that there is a small oscillation in the cost function near $T_i = 2$ for (b).	51
3.2 Optimised infidelity using basin-hopping for the state-to-state transfer problem of the LMG model (Sec. 3.3.1). M is the number of basis functions in the pulse. Local traps in optimisation have led to fluctuations in the optimised infidelity. Such fluctuation is more prominent when M is either too small (e.g. $M = 2$) or too large (e.g. $M = 14$).	57
A.1 For $N = 3$, the kinetic energy (blue), the potential energy (orange), and the total energy (green) of electron during conveyor-belt shuttling for a distance of one unit cell, i.e. 105 nm for $N = 3$. with linearly varying phase.	65
A.2 (a) The position, $x(\phi)$, (b) the perturbation of the position, and (c) the local curvature of the potential energy minimum, $\Delta x(\phi)$, was obtained by excluding the linear function from the $x(\phi)$ in Figure 2.3c. As the electron is shuttled for a distance of one unit cell, there are N repeating patterns, where $N = 3$ in this figure. The position curve in (a) and the curvature curve in (b) are the same as the position and curvature curve in Figure 2.3c as a function of the phase, ϕ , instead of time.	66
A.3 An example of voltage signal on the 1st gate in the unit cell for different choices of phase variation $\phi(t)$, i.e. linearly increasing phase, and phase generated by the look-up table(orange line). This is the same as the inset of Figure 2.3c	67
A.4 Probability density of the ground state in the z-direction (blue line). Probability density exists only in $z < -10$ nm, where there is a silicon layer. The probability density tails off at -11 nm, which makes the confinement length 1 nm below the interface (dotted line).	68

A.5 Cross-section of potentials on (a) the $y = 0$ nm and (b) $x = 27.5$ nm planes for the potential sampled at $z = -10$ nm (blue line) and the potential averaged over the probability density of the ground state in the z-direction for the thickness of 1 nm (orange line).	69
A.6 Contour plots of the probability densities of (a) the first, (b) second, and (c) 7th excited states of the 2D potential when $N = 3$ and $A = 100$ mV.	71
A.7 Convergence studies for the spatial resolution: The energy gap of the initial Hamiltonian obtained with different step sizes in (a) x and (b) y direction for $N = 5$	76
A.8 Convergence studies for the temporal resolution: For $N = 4$, (a) the loss probability and (b) excitation fraction obtained after the shuttling of $2.1\ \mu\text{m}$	77
A.9 (a) and (b) are equivalent circuits for lumped element model of a voltage source connected to N clavier gate(s) via a single bondwire. L is the inductance of the bondwire. C_1 is the capacitance of the bondpad, and C_2 is the capacitance of the clavier gates. R is the resistance of the metal connection from the bondpad to the gate.	80
A.10 (a) The loss probability and (b) excitation fraction with varying target speeds and the number of gates per unit cell.	82
A.11 (a) The loss probability and (b) excitation fraction with varying number of fixed potential settings and the number of gates per unit cell.	83
A.12 (a) The loss probability and (b) excitation fraction of digitization mode 1 (Staircase) and digitization mode 2 (Linear Interpolation) .	84
A.13 An example of voltage signal on the 1st gate in the unit cell for digitization mode 1(blue line) and mode 2(orange line).	85
A.14 The loss probability and excitation fraction for classical Johnson-Nyquist noise: (a) loss probability and (b) excitation fraction as a function of cut-off frequency γ , at $T = 4$ K; (c) loss probability and (d) excitation fraction as a function of temperature with three different cut-off frequencies, $\gamma = 10, 100, 1000$ GHz.	88
A.15 The probability of excitation to eigenstates of the instantaneous Hamiltonian for various (a) noise fractions and (b) cut-off frequency.	89
A.16 (a) Probability of excitation outside of the ground state and (b) excitation fraction during the shuttling for a target distance of $1.4\ \mu\text{m}$ at 5 different speeds, i.e. $v = 10, 50, 100, 300, 500$ m/s. The data of $v = 10$ m/s (blue line) in these figures are the same as $1 - P_{gs}$ data in Figure 2.9. Other parameters were set to $A = 50$ mV, $T = 2$ K, and $N = 3$	90

A.17 Contour plots of probability amplitudes of the electron moving through two charge defects for (a) $\Delta y = 2$ nm, (b) $\Delta y = 12$ nm, (c) $\Delta y = 25$ nm, (d) $\Delta y = 30$ nm. When the separation of two charge defects is small, ($\Delta y = 2, 12$ nm), the electron moves around the defects as in (a) and (b). When the separation is large ($\Delta y = 30$ nm) the electron moves through the middle without significant excitation as in (d). When neither of these actions is easy (e.g. $\Delta y = 25$ nm), the tunneling through the barrier produces significant excitation in the state, as in (c).	92
A.18 The average speed of adiabatic shuttling at varying depths with different number of instantaneous updates of the potential(M)	93
A.19 (a) Loss probability and (b) excitation fraction of the non-adiabatic shuttling at the varying depth(z) with different number of instantaneous updates of the potential(M)	94
A.20 Fractional excitation energy in the fast non-adiabatic shuttling method for different values of M : (a) $M = 8$, (b) $M = 16$, (c) $M = 32$, (d) $M = 64$. The method becomes more stable and have a periodic behaviour as the number of instantaneous changes, M , per unit cell increases.	95
A.21 The mean squared error(MSE) between the normalized potential, i.e. $\max V_\phi(x) = 1$ and two different functions: (a) $\cos(x)$ and (b) the quadratic fit at the bottom at three different phases, $\phi = 0, 1, 2$ rad. This shows that the potential becomes more like a sinusoidal function and that quadratic fit becomes better when the potential is sampled at deeper part of the channel.	96
B.1 The tensor network diagram to compare the gate fidelity of two 2-qubit gates, i.e. $\tilde{U}(T, \vec{\alpha})$ and U_{target} , using the Choi state $U_{target} \omega\rangle$. For 2-qubit gates, $ \omega\rangle$, is two Bell pairs, i.e. $ \Psi^+\rangle \otimes \Psi^+\rangle$. The subscripts of the gates denote the qubits that the gate is acting on.	110
B.2 The optimal time, T_{opt} , obtained by the TCRAB algorithm with simultaneous (blue line) and separate (orange line) optimisation of T and $\vec{\alpha}$, for varying initial guesses of evolution time, T_i . The simultaneous optimisation yields more variation in optimal time than the separate optimisation, and it is more likely to be stuck at the local minima for the separate optimisation. The optimisations were performed for entanglement generation of two capacitively coupled Josephson charge qubits (See Sec. 3.3.1.). Note that we used a local optimiser, L-BFGS-B, with 2000 as its maximum number of function evaluations.	111

B.3 Results of the entanglement generation of two capacitively coupled Josephson charge qubits are shown: (a) The number of function evaluations, n_{fev} , to reach the convergence, and (b) The resulting optimal time, T_{opt} , for each initial evolution time (CRAB)/ initial guess of optimal time (TCRAB), T_i . (c) The distribution of optimal time, T_{opt} , found by the TCRAB scheme.	115
B.4 Results of the state-to-state transfer from the ground state of paramagnetic phase to a ground state of ferromagnetic phase are shown: (a) The number of function evaluations, n_{fev} , to reach the convergence, and (b) The resulting optimal time, T_{opt} , for each initial evolution time (CRAB)/ initial guess of optimal time (TCRAB), T_i . (c) The distribution of optimal time, T_{opt} , found by the TCRAB scheme.	116
B.5 Results of the gate compilation of CZ for $\Omega \ll J$ are shown: (a) The number of function evaluations, n_{fev} , to reach the convergence, and (b) The resulting optimal time, T_{opt} , for each initial evolution time (CRAB)/ initial guess of optimal time (TCRAB), T_i . (c) The distribution of optimal time, T_{opt} , found by the TCRAB scheme.	116
B.6 Results of the gate compilation of CZ for $\Omega \gg J$ are shown: (a) The number of function evaluations, n_{fev} , to reach the convergence, and (b) The resulting optimal time, T_{opt} , for each initial evolution time (CRAB)/ initial guess of optimal time (TCRAB), T_i . (c) The distribution of optimal time, T_{opt} , found by the TCRAB scheme.	116
B.7 Results of the identity test for (a) two capacitively coupled Josephson charge qubits, (b) the LMG model, and two spin qubits in Silicon quantum dots in the regime of (c) $\Omega \ll J$ and (d) $\Omega \gg J$. For all four cases, we performed CRAB with varying T_i for the gate compilation of the identity gate using the given drift and control Hamiltonians. For a state-to-state transfer problem, we only need to show the compilation of identity for the given initial state. Thus, we used the initial states specified in Sec. 3.3.1 and set the target states the same as the initial states. On the other hand, we used the Choi state scheme as explained for the gate compilation Sec. B.3.	119

xx

List of Abbreviations

- 1-D, 2-D** . . . One- or two-dimensional, referring in this thesis to spatial dimensions in an image.
- Otter** One of the finest of water mammals.
- Hedgehog** . . . Quite a nice prickly friend.

Neque porro quisquam est qui dolorem ipsum quia dolor sit amet, consectetur, adipisci velit...

There is no one who loves pain itself, who seeks after it and wants to have it, simply because it is pain...

— Cicero's *de Finibus Bonorum et Malorum*

1

Introduction

Contents

1.1	Motivation	1
1.2	Contribution	3

1.1 Motivation

The rapid advance of minimally-invasive cardiac procedures promises improvements in patient safety, procedure efficacy, and access to treatment. While percutaneous coronary intervention (PCI) has become routine and highly effective [bravata_systematic_2007], catheter procedures in areas such as electrophysiology (EP) and valve replacement are still coming of age. This progress is driven by demographics and the improvement in general cardiac care, as patients surviving initial cardiac events go on to require treatment for sequelae [foot_demographics_2000]. The growing need for advanced treatment is being answered by developments in catheter technology and procedures. These tools are continually advancing to access and manipulate an ever-broader range of anatomy [sousa_new_2005].

Lorem ipsum dolor sit amet, consectetur adipiscing elit. Maecenas sagittis dolor at nulla feugiat, vitae iaculis est rutrum. Mauris eu sem eros. Sed id faucibus urna. In egestas eros et sapien egestas imperdiet. In hac habitasse platea dictumst. Phasellus vitae varius tortor. Mauris nec sollicitudin enim. Suspendisse molestie leo nec mauris molestie, nec imperdiet magna vehicula. Phasellus sodales tortor dui, a lacinia turpis congue at. Pellentesque mattis dui non libero commodo, at accumsan ex ultrices. Integer eget ex eget dui cursus euismod et accumsan felis. Nullam laoreet sodales dui, ut finibus elit varius a. Sed elementum orci quis libero ullamcorper, eget egestas enim convallis. Sed nibh libero, tincidunt ultricies nibh quis, lobortis placerat mauris. Maecenas at laoreet risus, nec dictum libero. Donec accumsan, orci eu tempus mattis, nisl arcu auctor turpis, ac sollicitudin justo orci nec nulla.

Nam eget sem sed ligula vehicula iaculis. In non arcu a nisl interdum gravida. Nam egestas erat non turpis sagittis vestibulum. Praesent est metus, facilisis eu commodo sed, sagittis et est. Duis scelerisque luctus erat, elementum pulvinar felis bibendum a. Morbi hendrerit rhoncus consectetur. Vestibulum nec odio finibus, blandit turpis eget, dignissim orci. Curabitur eu ligula auctor, porttitor nulla non, maximus turpis. Nunc sed quam at est varius interdum eu vitae odio. Vestibulum egestas dapibus nulla sit amet fermentum.

Vestibulum ut neque urna. Ut nec odio lobortis, ultricies nulla quis, ultricies tellus. Nam ac iaculis sapien. Vivamus vitae risus id tortor interdum pellentesque. Quisque lorem lectus, sagittis vel metus et, sagittis finibus justo. Curabitur pulvinar odio tellus, eu vehicula est dictum eget. Morbi sed justo justo. Vivamus enim nibh, facilisis pretium luctus quis, ullamcorper quis ipsum. Pellentesque a mi a elit euismod malesuada.

Vestibulum interdum est vel orci tincidunt auctor. Nunc tristique nulla nec blandit fermentum. Maecenas id libero ut justo dictum sodales. Nullam justo sapien, dignissim vel enim at, porta pharetra metus. Integer euismod quam eget ligula gravida euismod. Pellentesque commodo, quam sit amet bibendum tempor, nisi odio varius mauris, et accumsan justo ex sed nunc. Cras bibendum nibh ac dolor volutpat, non elementum orci pulvinar. Maecenas et porttitor nulla. Suspendisse

sapien massa, dapibus at blandit et, rhoncus suscipit velit. Fusce molestie, velit eget sagittis suscipit, est libero aliquam libero, in iaculis mi tellus ac nunc.

1.2 Contribution

Sed in rhoncus lectus. Mauris vulputate purus non malesuada pulvinar. Curabitur ullamcorper hendrerit elit, id vulputate libero sagittis vel. Pellentesque ac faucibus est. Class aptent taciti sociosqu ad litora torquent per conubia nostra, per inceptos himenaeos. Integer venenatis, nisl eleifend pellentesque consequat, sem tortor malesuada ante, ut tincidunt elit tortor sit amet nunc.

Cras vehicula ipsum sit amet dui rutrum ultrices. Integer eu eleifend odio. Praesent tempor, libero id ullamcorper euismod, lectus diam lobortis mauris, id venenatis arcu sem vitae purus. Pellentesque luctus tristique metus quis mollis. Praesent ullamcorper neque velit, sed iaculis est convallis sit amet. Quisque nec massa ut magna lobortis imperdiet. Quisque rhoncus purus eget mollis aliquet. Donec vehicula viverra nisl, sed posuere turpis vulputate non. Donec malesuada, eros id interdum volutpat, ipsum orci luctus quam, non pulvinar urna ipsum eget purus. Nam hendrerit condimentum tristique.

Proin metus velit, tempor at fringilla non, dictum eu felis. Proin volutpat enim ut fermentum aliquam. Nam dictum nisi eu nisl viverra fermentum. Pellentesque tristique arcu non orci congue faucibus. Fusce sit amet nisl fringilla, feugiat turpis vitae, eleifend ante. Suspendisse elementum, lectus non pulvinar bibendum, lectus massa faucibus turpis, vitae porta risus sem quis metus. Maecenas id sapien et dui lobortis imperdiet nec eu mi. Quisque porttitor tincidunt nisi, eget sagittis orci. Nunc mattis erat malesuada facilisis viverra. Maecenas sodales iaculis nisi vel tincidunt. Morbi aliquet nibh ac facilisis consectetur. In ultrices libero quis massa porttitor cursus. Quisque suscipit ac tortor eget aliquet. Ut eget lacus vel orci viverra maximus at at purus.

Nam massa neque, varius nec suscipit id, cursus ac mi. Cum sociis natoque penatibus et magnis dis parturient montes, nascetur ridiculus mus. In hac habitasse platea dictumst. Vivamus facilisis nunc quis dictum consectetur. Sed congue

sed magna non auctor. Vestibulum accumsan sit amet erat non congue. Sed at condimentum mi, sed scelerisque urna. Etiam tristique pulvinar rutrum. Donec semper nulla vitae rutrum semper. Maecenas ultrices nibh at orci sodales tincidunt sit amet vitae arcu. Curabitur interdum tincidunt ipsum, nec tincidunt nunc dapibus in. Nunc sit amet elementum massa, ut ornare lacus. Vivamus convallis fringilla erat, non suscipit sapien convallis eu. Nunc viverra lectus sit amet turpis viverra, eget iaculis purus rhoncus.

Morbi eu lectus arcu. Sed fringilla dui ut magna commodo, a malesuada ante pellentesque. Donec ornare facilisis pellentesque. Nulla vitae fringilla velit. Nunc id tellus nisl. Maecenas pretium elit lectus, nec consectetur nunc vulputate et. Sed facilisis magna nec gravida hendrerit. Sed a cursus nisl, in rhoncus massa. Curabitur ut nibh interdum, tempor risus vel, scelerisque nibh. Mauris quis ipsum sed risus tempor convallis ut a eros.

*Alles Gescheite ist schon gedacht worden.
Man muss nur versuchen, es noch einmal zu denken.*

*All intelligent thoughts have already been thought;
what is necessary is only to try to think them again.*

— Johann Wolfgang von Goethe
[von_goethe_wilhelm_1829]

2

Robustness of electron charge shuttling: Architectures, pulses, charge defects and noise thresholds

Contents

2.1	Introduction	5
2.2	Description of the Shuttling Device	6
2.3	Voltage profiles for conveyor-belt Shutting	11
2.4	Numerical Simulations	13
2.5	Performance metrics	15
2.6	Noiseless Shutting	17
2.7	Sensitivity to Johnson-Nyquist noise	18
2.8	Sensitivity to Charge Defects	24
2.9	Advanced non-adiabatic ultra-fast shuttling	28
2.10	Implications for coherent qubit transport	30
2.11	Conclusions	32

2.1 Introduction

This document introduction won't serve as a complete primer on L^AT_EX. There are plenty of those online, and googling your questions will often get you answers, especially from <http://tex.stackexchange.com>.

Instead, let's talk a little about a few of the features and packages lumped

into this template situation. The `savequote` environment at the beginning of chapters can add some wittiness to your thesis. If you don't like the quotes, just remove that block.

For when it comes time to do corrections, there are two useful commands here. First, the `mccorrect` command allows you to highlight a short correction like this one. When the thesis is typeset normally, the correction will just appear as part of the text. However, when you declare `\correctionstrue` in the main `Oxford_Thesis.tex` file, that correction will be highlighted in blue. That might be useful for submitting a post-viva, corrected copy to your examiners so they can quickly verify you've completed the task.

For larger chunks, like this paragraph or indeed entire figures, you can use the `mccorrection` environment. This environment highlights paragraph-sized and larger blocks with the same blue colour.

Read through the `Oxford_Thesis.tex` file to see the various options for one-and two-sided printing, including or excluding the separate abstract page, and turning corrections and draft footer on or off, and the separate option to centre your text on the page (for PDF submission) or offset it (for binding). There is also a separate option for master's degree submissions, which changes identifying information to candidate number and includes a word count. (Unfortunately, L^AT_EX has a hard time doing word counts automatically, so you'll have to enter the count manually if you require this.)

2.2 Description of the Shuttling Device

Shuttling of an electron is achieved by creating a moving QD using a set of voltage pulses applied to metallic gates. Here, we explore shuttling devices broadly consistent with the Spin Qubit Shuttle (SQS) proposed by Langrock et al.[1]. A significant distinction is that while Langrock et al. focused on a silicon/silicon-germanium device, here we consider devices consistent with silicon/silicon-oxide structures. Figure 2.1 shows a sketch of the device; Figure 2.2 indicates the key dimensions. At the top surface, a periodic array of so-called clavier gates is deposited in the

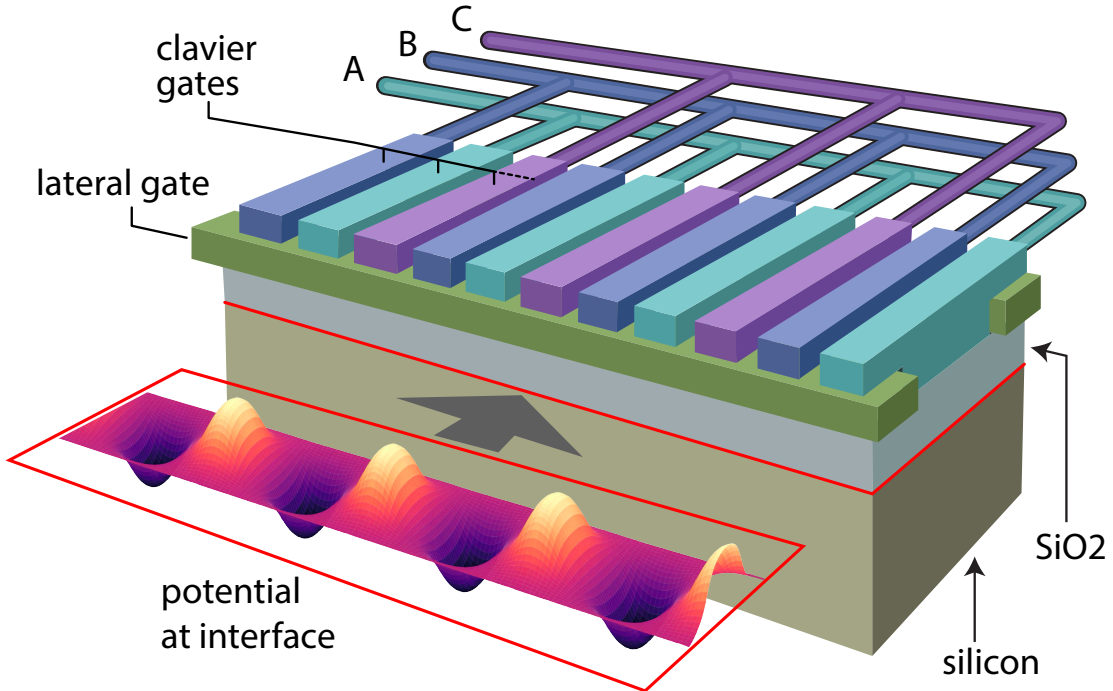
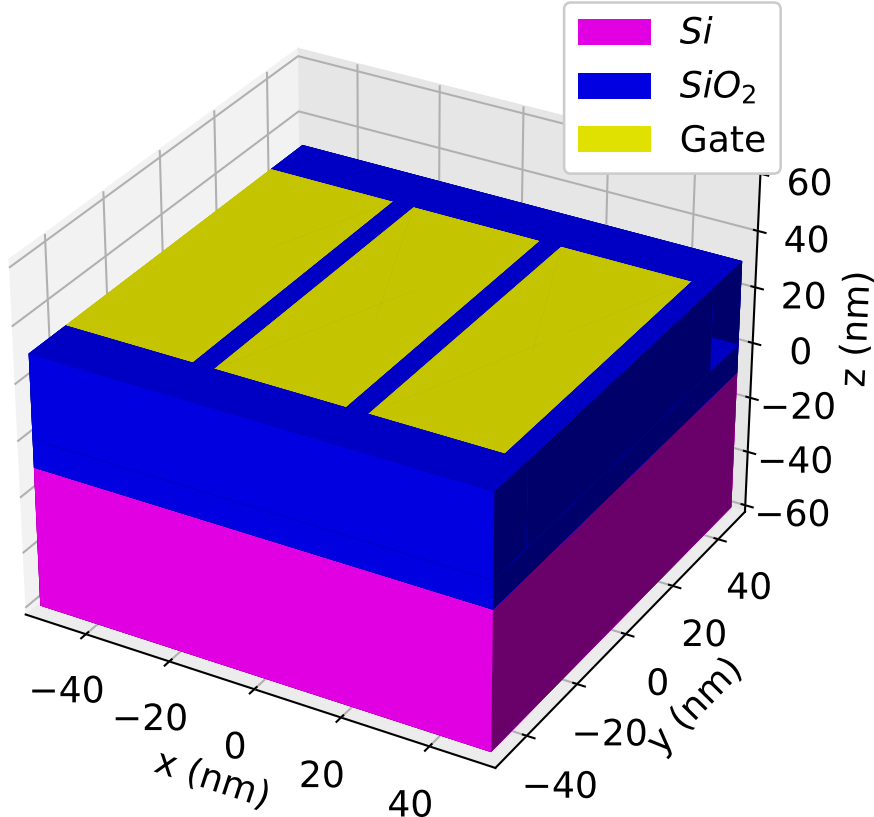


Figure 2.1: Conceptual illustration of the conveyor-belt shuttling device studied in this paper. The electrons are confined near a silicon-oxide interface below a periodic array of gates to which external potentials can be applied via voltage lines A, B and C. In this paper we consider devices with three repeating electrodes, as depicted, as well as four [1] and five.

shuttling direction. The clavier gates are embedded inside the SiO_2 layer. The electron moves in a channel, which is located near the interface of Si and SiO_2 . To confine the electron to move only in one direction, two lateral confinement gates are deposited just below the clavier gates and a large negative voltage (typically around -1 V) is applied to these. Finally, the bottom of the device is grounded, i.e. 0 V . The voltages on the clavier gates form a periodic array of quantum dots along the channel; a single electron is initially loaded from a single-electron transistor (SET) into the leftmost dot, then shuttled along the channel by varying the clavier gate voltages until it reaches a second SET at the right-hand end.

We made a number of simplifications to model this device. First, we assumed that the confinement gates have a sufficiently strong negative voltage that they act like hard walls at the sides of the channel. Second, since the electron moves below the confinement gates, we assumed that the effective potential it experiences is formed only by those parts of the clavier gates that are not screened by the

(a)



(b)

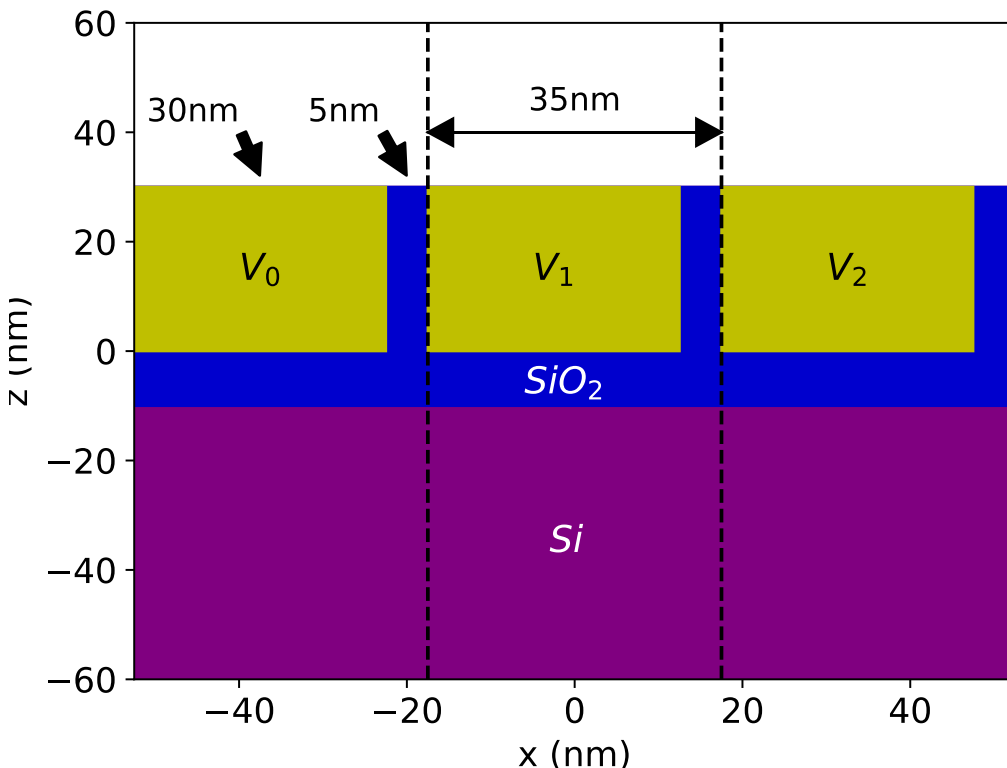


Figure 2.2: Illustration of (a) the shuttling device in 3D and (b) its cross-section in the xz plane. The yellow boxes are clavier gates with width and height of 30 nm along the x and z direction and the length of 75 nm along the y direction. The gap between the gates is 5 nm. The size of this unit cell with three gates is 105 nm along the shuttling direction, i.e. the x-direction. The clavier gates are implanted in the oxide layer (blue). Below the oxide layer, there is a Si layer (magenta), whose base is grounded.

confinement gates. Third, we assume there are infinitely many clavier gates lined up in a row in the shuttling direction. Finally, we assume that the confinement in the z-direction is very strong, and the quantum dots are formed nearly at the interface of the Si and SiO₂[2].

Given these assumptions, our device model is illustrated (for the case of three independent electrode voltages) in Figure 2.2. The yellow boxes denote the clavier gates, the blue area denotes SiO₂, and the magenta box represents the Si. Figure 2.2a shows a 3D illustration of the full device while Figure 2.2b shows a cross-section of the device through the centre of the channel. The dimensions of the clavier gates are $(h, w, l) = 30 \text{ nm} \times 30 \text{ nm} \times 75 \text{ nm}$, while the gap between the electrodes is fixed to 5 nm. Furthermore, the interface between the Si and SiO₂ is 10 nm below the bottom of the clavier gates as shown in Figure 2.2b.

The Hamiltonian of the electron in 3D is given by

$$H = \frac{1}{2}\mathbf{p}^T M^{-1} \mathbf{p} - e\Phi(V_0(t), V_2(t), \dots, V_{N-1}(t)), \quad (2.1)$$

where M is the anisotropic mass tensor in silicon, and N is the number of gates per unit cell. Note that the potential, Φ , is a function of time-dependent gate voltages.

In this paper, we ran simulations in 2D, using only the transverse electron mass, i.e. $m^* = 0.19m_e$ (See section 2.4 and appendix A.1.3). This reduces the Hamiltonian to

$$H = \frac{1}{2m^*}\mathbf{p}^2 - e\Phi_{Si/SiO_2}(V_0(t), V_2(t), \dots, V_{N-1}(t)), \quad (2.2)$$

where we sample the 2D potential Φ_{Si/SiO_2} from the 3D potential, Φ , at the Si–SiO₂ interface (See section 2.4). Aside from our investigation of charge defects in section 2.8, the form of Hamiltonian in equation 2.2 doesn't change; However, the time-dependent gate voltages change due to, e.g., the Johnson-Nyquist noise in section 2.7 or different pulse shapes in section 2.9.

2.3. Voltage profiles for conveyor-belt Shuttling

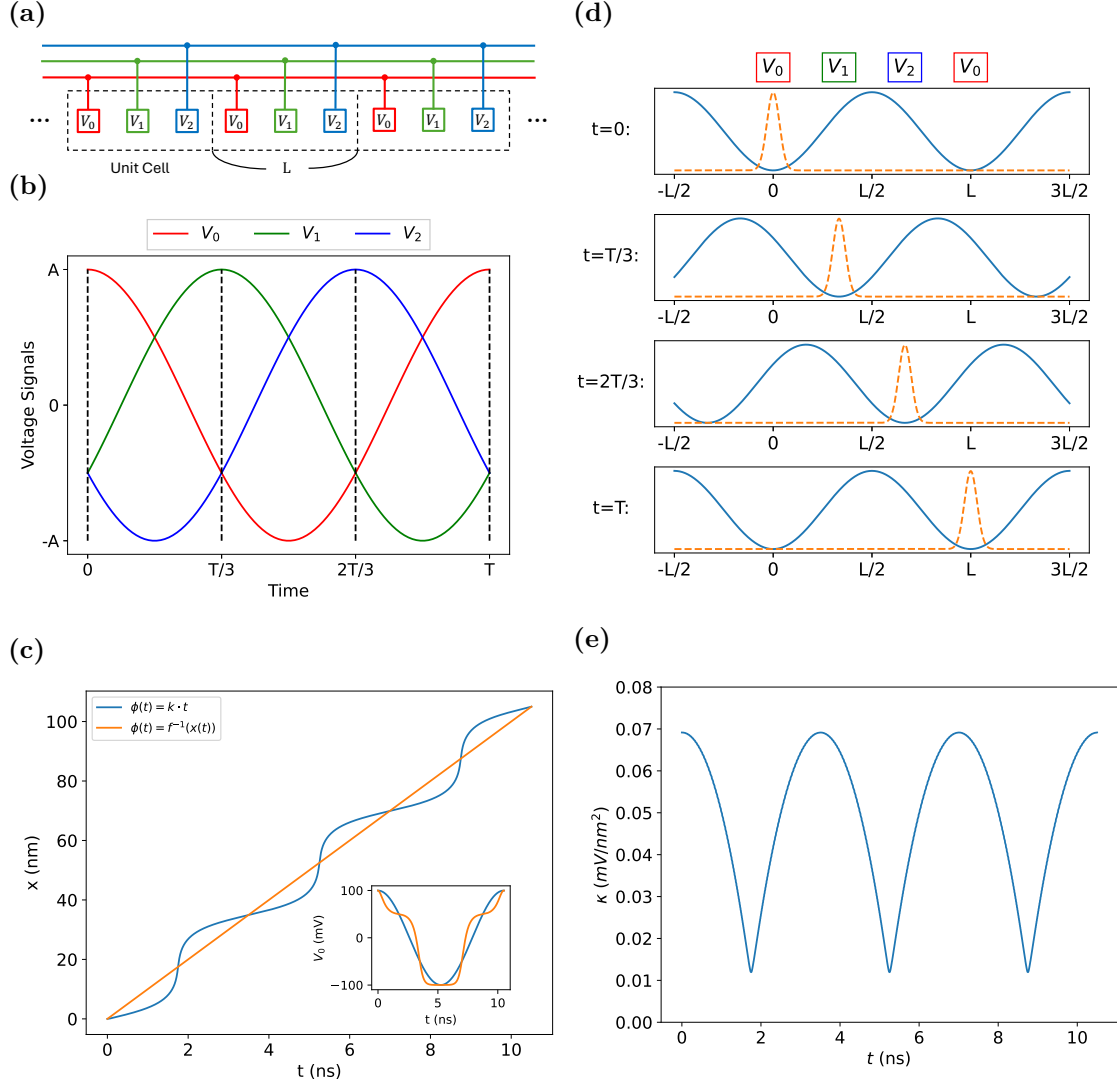


Figure 2.3: Illustration of the voltage pulses applied to the gates in conveyor-belt shuttling for three gates per unit cell, i.e. $N = 3$. (a) Every 3rd gate is connected to the same voltage source (denoted as red, green and blue lines). (b) The three independent pulses are sinusoidal with $2\pi/3$ phase difference. (c) The position, x , of the potential minimum as a function of time when the average shuttling speed is 10 m/s. The lines correspond to different choices of phase variation, $\phi(t)$: linearly varying phase $\phi(t) = k \cdot t$ (blue line), and phase obtained by using a look-up table, f^{-1} , $\phi(t) = f^{-1}(x(t))$ (orange line). The detailed arguments are given in Appendix A.1.2. (d) The resulting time-evolution of the potential and approximate position of the electron wave packet. The red, green, and blue boxes above denote the same clavier gates of the corresponding colour in (a) and (b). (e) Variation of the curvature at the potential minimum, κ , obtained by fitting the slice of potential energy at $y = 0$ with a quadratic function (see also the plots of the full potential in Figure 2.4). Note that panels (a),(b), and (c) relate the panels (e), (f), and (g) of Figure 2 of Langrock et al.[1].

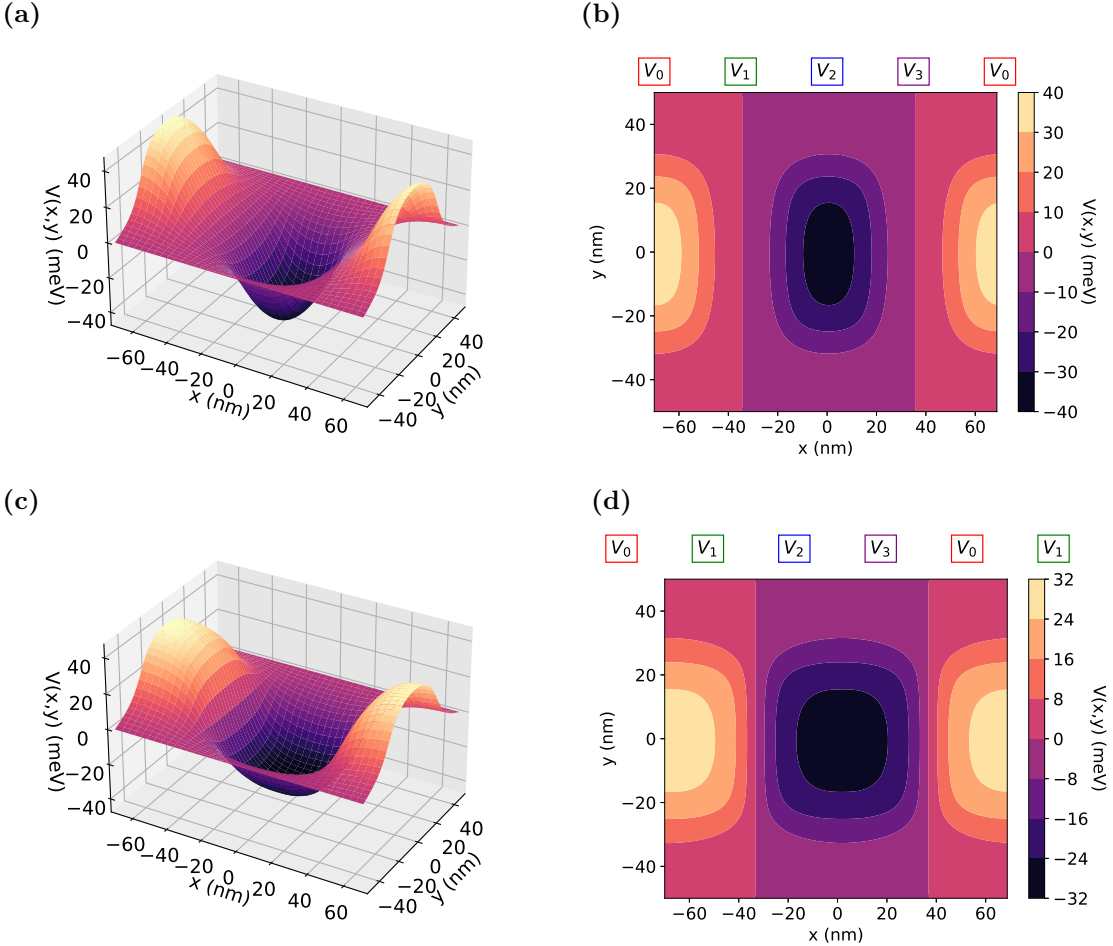


Figure 2.4: 3D and contour plots of the potential energy, $V(x,y)$, generated by the gates for $N = 4$ with $A = 100$ mV. (a) 3D and (b) contour plots of the potential energy for one unit cell centred around the potential minimum when the curvature near the potential minimum, $\kappa(\phi)$, is maximum (corresponding to a potential well directly below an electrode). (c) 3D and (d) contour plots of the potential energy for one unit cell centred around the potential minimum when $\kappa(\phi)$ is a minimum (corresponding to a potential well between two electrodes).

2.3 Voltage profiles for conveyor-belt Shuttling

Conveyor-belt shuttling is achieved by creating a single QD moving in a desired trajectory (along the positive x direction in our case). As explained in Langrock et al.[1], such a potential can be created by applying sinusoidal voltage signals to the gates with a phase difference of $2\pi/N$ between successive gates; N is then the number of independent voltage signals required:

$$V_i(t) = A \cos\left(\phi(t) - \frac{2\pi i}{N}\right), \quad (2.3)$$

where A and $\phi(t)$ are the amplitude and phase of oscillation, respectively. Figure 2.3a illustrates the repeating voltage signals; using an analogy from condensed-matter physics, we define a sequence of N adjacent gates as a *unit cell*. To be specific, the size of the unit cell along the shuttling direction, i.e. the x-direction, changes with the number of gate per unit cell, N . For example, the length of a unit cell is 105 nm for three gates per unit cell, but 175 nm for five electrodes per unit cell. Such a scheme solves the signal fan-out problem because the device only needs N control lines regardless of the number of gates. For example, in the case of 4 gates in the unit cell, the applied pulses will be $\cos(\phi(t))$, $-\sin(\phi(t))$, $-\cos(\phi(t))$, and $\sin(\phi(t))$, where $\phi(t)$ is the phase as a function of time. The resulting evolution of voltage pulses at the clavier gates with time is illustrated in Figure 2.3b. To give a sense of direction, there must be at least three gates per unit cell. Figure 2.3d shows the wave function propagating from left to right using the conveyor-belt shuttling at 4 different times.

These voltage signals will successfully drive shuttling if the process proves to be adiabatic and thus the wave function closely follows the minimum of the potential energy. The instantaneous speed of shuttling is proportional to the first derivative of the phase $\phi(t)$ in the sinusoidal pulses. Hence, the shuttling trajectory depends on how the phase $\phi(t)$ is varied. We examined two possible ways to vary this phase: the first was a simple linear variation, while the second was designed to achieve a uniform propagation speed for the minimum of the quantum dot potential, the phases themselves being determined from a position-phase look-up table. Figure 2.3c shows the shuttling trajectories and voltage pulses (inset) for these two different methods of phase variation. However, a detailed comparison between the linearly increased phase and the phase obtained from the look-up table (in Appendix A.1.2) showed that there is little practical difference between the two methods. Thus, we chose to update the phase linearly because it is easier to generate simple sinusoidal pulses on-chip than to apply more complicated pulses.

2.4 Numerical Simulations

For a given device geometry, specified as in section 2.2, it is necessary to solve the Laplace equation to obtain the QD potential, $\Phi(x, y, z, t)$, and then to solve the time-dependent Schrödinger equation to simulate the dynamics of the shuttling. Periodic boundary condition was chosen along the shuttling direction, i.e. the x-direction, and $V = 0$ was chosen for the bottom surface and sides of the shuttling track. In between the gates, Neumann boundary conditions of $\partial\phi/\partial z = 0$ was imposed. At the Si-SiO₂ interface, the continuity of the displacement field was imposed, and the relevant relative permittivity for Si (11.69) and SiO₂ (3.9) were used. A detailed description of the boundary conditions is outlined in Appendix A.2.1. For the Poisson solver, we defined a uniform rectangular grid in 3D with finite difference approximation for the differential operators. We used successive over-relaxation (SOR)[3, 4] to obtain the time-dependent potential in the unit cell in Figure 2.2. For faster generation of the time-dependent potential, we used the superposition principle, based on the linearity of the Laplace equation, as noted in equation A.1 in Appendix A.2.2. On the other hand, for the Schrödinger solver, we used uniform rectangular grid in 2D on the plane defined by $z = -10$ nm. We used the split operator method[5] with symmetric Strang splitting[6, 7] to solve the time-dependent Schrödinger equation. The convergence of the numerical methods were test in Appendix A.2.4. Finally, the choices of unit systems and hyperparameters of the numerical methods are given in Appendix A.2.3.

If we assume that the z -axis confinement is so strong that the electron only moves in the plane of the Si/SiO₂ interface, modelling in 2D is enough to capture the relevant physics. The perpendicular extent of the wave-function is anyway reduced because the lowest-energy bound states are formed from the $\pm z$ -valleys, so the motion in the z -direction is determined by the longitudinal (heavy) electron mass. Furthermore, SiO₂ has large band gaps that allow strong electric fields to confine electrons in the z -direction without leakage out of the channel[2]. As a result, the typical confinement length of the QD in the z -direction is of order 1 nm[8–10] while the oxide layer thickness is 10 nm. Thus, we sampled our 2D potential at the

interface between Si and SiO_2 . A detailed comparison of the potential sampled at the interface and the potential averaged over the probability density of the ground state in the z -direction is given in Appendix A.1.3.

We may further reduce the dimensionality to 1D if we assume that the voltages at the confinement gates are so high that the electron never undergoes excitation in the y -direction. A detailed comparison of 1D and 2D simulations is given in Appendix A.1.4. 1D and 2D simulations yield different loss probabilities and excitation fractions with an order of magnitude difference for realistic parameters. This highlights the importance of simulating in 2D and that the potential is non-separable. We therefore report results of the more accurate 2D simulations in the remainder of the paper.

Note that the atomic scale interface roughness was neglected in our simulations. Given that interface roughness has a similar nature to the Johnson-Nyquist noise, the results of section 2.7 imply that it only affects the orbital excitation if there is a frequency component in the moving frame of the electron that is comparable to the energy gap in the orbital degree of freedom. For example, if the shuttling speed is 100 m/s and the smallest length scale of roughness is, say, 0.5 nm, the maximum change in frequency is 0.2 THz, which is much smaller than the frequency of characteristic energy gap, i.e. $\Delta E_{gs,2e}/\hbar = 1.46 \text{ THz}$.

We also neglect the effect of valley physics. This is likely to have minimal effect on charge shuttling: valley-orbital anti-crossings are unlikely to occur because the four transverse valley states have much higher energy than the $\pm z$ -valleys. In any device where the tensile strain in Si exceeds 0.1 %, the transverse valley states lie more than 20 meV above the $\pm z$ -valleys [11], comfortably higher than our characteristic orbital energy gap of 6.02 meV ($A = 100 \text{ meV}$ and $N = 4$ electrodes per unit cell). Furthermore, given strong confinement in the z -direction (confinement length $\sim 1 \text{ nm}$), there is an additional contribution to the splitting from the effective mass anisotropy (the longitudinal mass is around 5 times bigger than the transverse mass). On the other hand, the lowest valley excitation occurs within the $\pm z$ -valleys and lies well below the orbital excitations (The energy scale of excited valley states

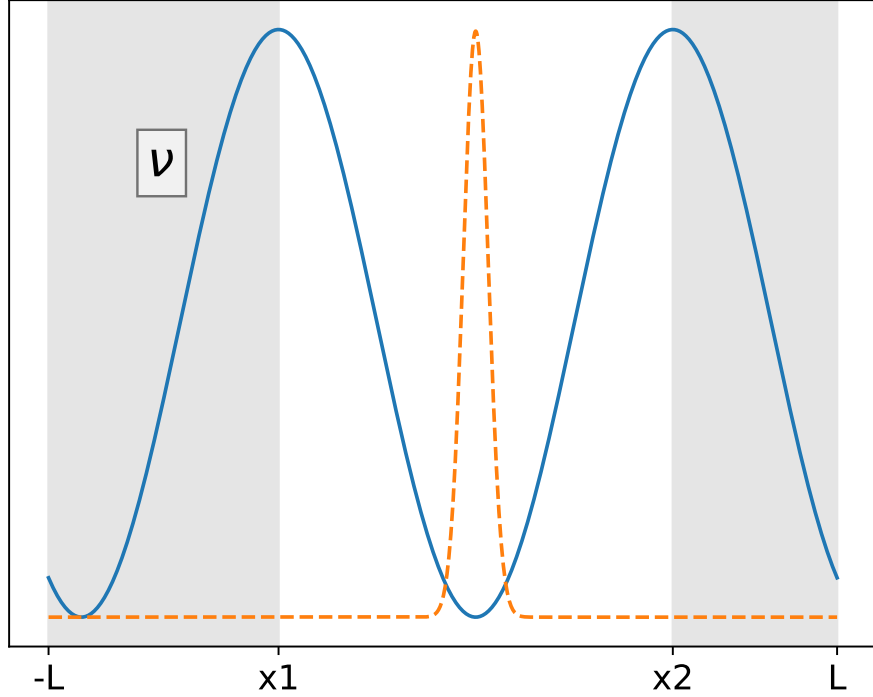


Figure 2.5: Illustration of the definition of the loss probability as the integrated probability density (orange line) over the shaded region ν , defined as the region outside the well in potential energy (blue line) being used to shuttle the electron.

is $\mathcal{O}(10\text{-}100 \mu\text{eV})$ while the energy scale of orbital states is $\mathcal{O}(1 \text{ meV})$; it is not resolved in our calculations but does not significantly affect the location of the shuttled charge. Therefore, valley-orbital anti-crossings are unlikely unless the tensile strain is unusually small.

2.5 Performance metrics

We will characterise the shuttling process by evaluating its capability to move the spin qubit to the target position (1) without losing the qubit and (2) with a good degree of adiabaticity. Specifically, the excitation in the orbital state is important as the g -factor of the electron in silicon depends both on its position and orbital state[1, 12]. Thus, the two most import imperfections to evaluate the shuttling scenarios are (1) the probability P_L of losing the electron from the potential well

and (2) the amount of excitation from the ground state.

The loss probability is defined as the probability that the electron is found outside the single QD where it was initially loaded. Since we have periodic boundary conditions along the x-axis, we need at least two unit cells, i.e. two QDs, to calculate the loss probability. When there are two unit cells, the loss probability is equivalent to the probability of the electron to be in the other ‘wrong’ QD (since we solve the TDSE only within the channel region, the electron cannot leave the channel). Figure 2.5 shows the illustration of calculation of loss probability. The loss probability is the probability in the shaded region, ν :

$$P_L = \int_{\nu} dx dy |\psi(x, y)|^2 \quad (2.4)$$

where $\psi(x, y)$ is a 2-dimensional wave function.

The excitation fraction is a dimensionless measure of the level of excitation of the system due to non-adiabatic effects. It is defined as the ratio $\Delta E / \Delta E_{gs,2e}$ where ΔE is difference between the expectation value of the energy and the (instantaneous) ground state energy and $\Delta E_{gs,2e}$ is a characteristic energy gap; it should be interpreted as the excess energy relative to this characteristic energy gap. Since the excitation primarily occurs in the direction of shuttling, the characteristic energy gap was chosen as the energy gap of the ground to the second excited state, so that $\Delta E / \Delta E_{gs,2e} = (E - E_{gs}) / (E_{2e} - E_{gs})$. Figures A.15a and A.15b show that excitation primarily populates the second excited state, which is the excitation mode in the x-direction as shown in Figure A.6.

Additionally, we calculated the probabilities of excitation to the n th eigenstate of the instantaneous Hamiltonian. This metric was used to compare the performance of the noisy shuttling cases, as the fidelity between the final state and the ground state deviates from 1 by the order of only 10^{-7} for noise-free shuttling.

When we report metrics for the overall performance of the shuttling experiment, these are computed using the state of the system during the static phase after the shuttling procedure. The static phase involved an additional 5000 time steps (≈ 13.5 ps) to evolve the state with the stationary potential at the end of the shuttling.

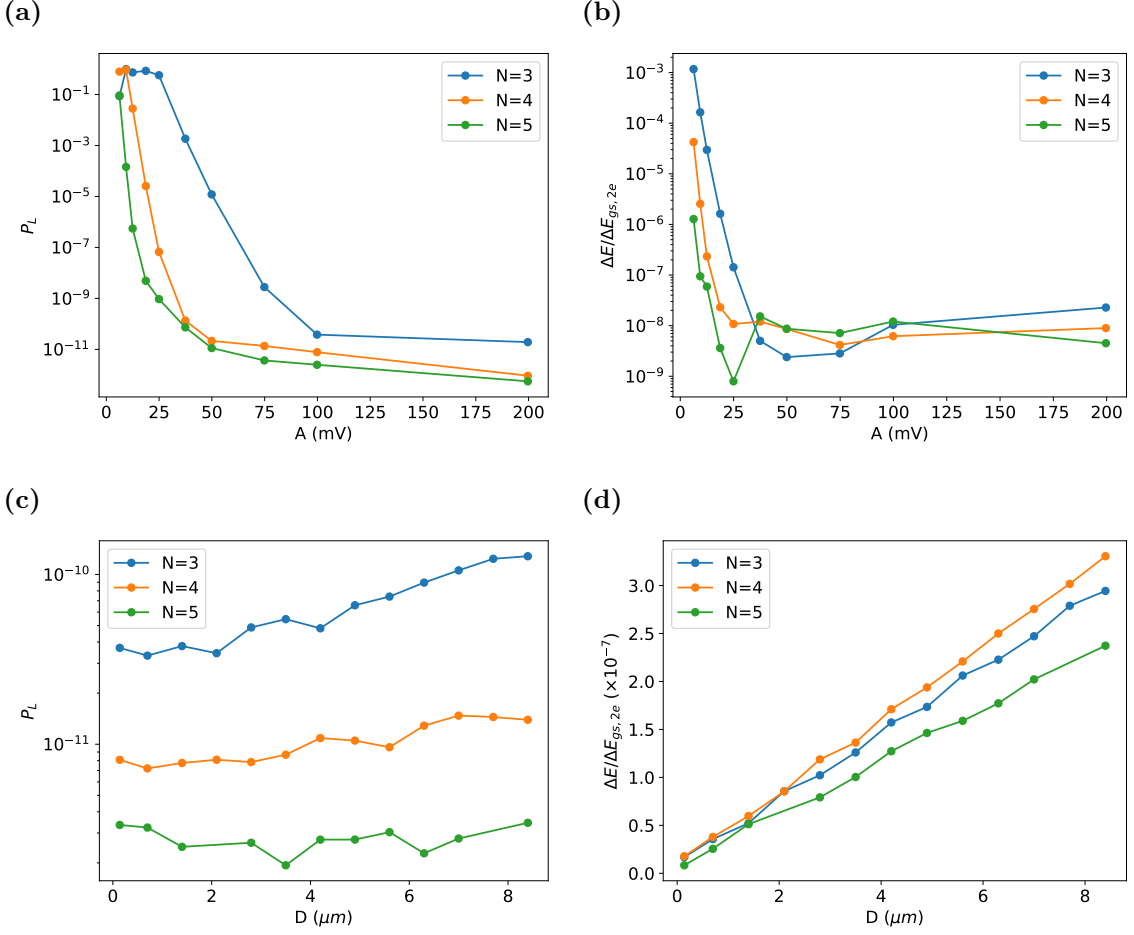


Figure 2.6: The loss probability and excitation fraction for different noiseless shuttling scenarios: (a) loss probability and (b) excitation fraction as a function of voltage signal amplitude, A , for a shuttling distance of $1.4 \mu\text{m}$; (c) loss probability and (d) excitation fraction as a function of target distance, D , for a signal amplitude of 100 mV . Results for different numbers of electrodes per unit cell ($N = 3, 4, 5$) are shown.

While the excitation fraction remains constant up to a numerical precision during this period, the loss probability may vary if the potential barrier is too low, much lower than our default setting of 100 mV . Effectively, we sampled one loss probability value in this case; These scenarios, however, correspond to a failed shuttling, and any small fluctuation in loss probability is not of much interest.

2.6 Noiseless Shuttling

In this section, we present the results from shuttling scenarios where there is no noise and no defect charges are present. While the quality of shuttling depends on

many parameters, we selected three independent variables: (1) the target distance, (2) the amplitude of the voltage signals at the gates, and (3) the number of gates in a unit cell.

Figures 2.6a and 2.6c show the loss probability and excitation fractions for different amplitudes of sinusoidal oscillations at the gates. Larger signal amplitudes make a deeper QD, and thus the loss probability decreases. Our typical value of amplitude, 100 mV, resulted in a loss probability of 3×10^{-11} even for $N = 3$ electrodes. The loss probability reduces even further for larger numbers of electrodes as the depth of the QD and the inter-dot distance both increase. For example, when the amplitude is 50 mV, we see a loss probability of 10^{-5} for $N = 3$ while we see the similar loss probabilities for $N = 4$ and $N = 5$ when the amplitudes are 25 mV and 12.5 mV.

Figures 2.6b and 2.6d show the loss probability and excitation fraction with different target distances. The mean shuttling speed and the amplitude of voltage signals were fixed to 10 m/s and 100 mV, respectively. As the target distance increases, both the loss probability and excitation fraction increase. The worst case occurs when the number of electrodes is three and the target distance is $8.4 \mu\text{m}$, which nevertheless results in near-ideal behaviour: a loss probability of 1.3×10^{-10} and an excitation fraction of 2.7×10^{-7} .

Given these data, we conclude that noiseless shuttling is practically perfect when the default speed and amplitude were used with the target distance up to $8.4 \mu\text{m}$. The quality of shuttling significantly depends on the amplitude of the voltage signal and the number of gates per unit cell. To reduce the loss probability, it is always beneficial to use more gates per unit cell; but for a broad range of cases we find that $N = 3$ is quite sufficient for near-ideal performance.

2.7 Sensitivity to Johnson-Nyquist noise

Since noise-free shuttling is nearly perfect, we further investigated the effect of discontinuities in the voltage signals. The full results are described in Appendix A.3.2 and we summarise here. Two extreme cases were studied: staircase-like potentials

in time, with step-changes in the potential at defined intervals, and potentials formed from piece-wise linear functions connecting the midpoints of the steps of the staircase-like potential (See Figure A.13). From Figure A.12, we concluded that staircase-like discontinuities in the voltage signals result in much more loss and excitation than continuous signals.

Fortunately, these staircase-like voltage profiles constitute an adversarial model that is somewhat unphysical, as in reality there is a finite response time for any change of voltage at the gates. However, rapid changes in the gate voltages on frequencies up to this cutoff can still arise from Johnson-Nyquist noise [13, 14], which is a thermal noise at the resistor caused by random thermal agitation. We therefore proceed to explore the impact of such noise when physically motivated.

Figure A.9 shows a lumped-element model of a voltage source connected to clavier gates via a single bondwire. L is the inductance of the bondwire, R is the resistance of the metal connection from the bondpad to the gate, C_1 is the capacitance of the bondpad, and C_2 is the capacitance of clavier gate. (See appendix A.2.6) The power spectral density of classical Johnson-Nyquist noise can be derived as

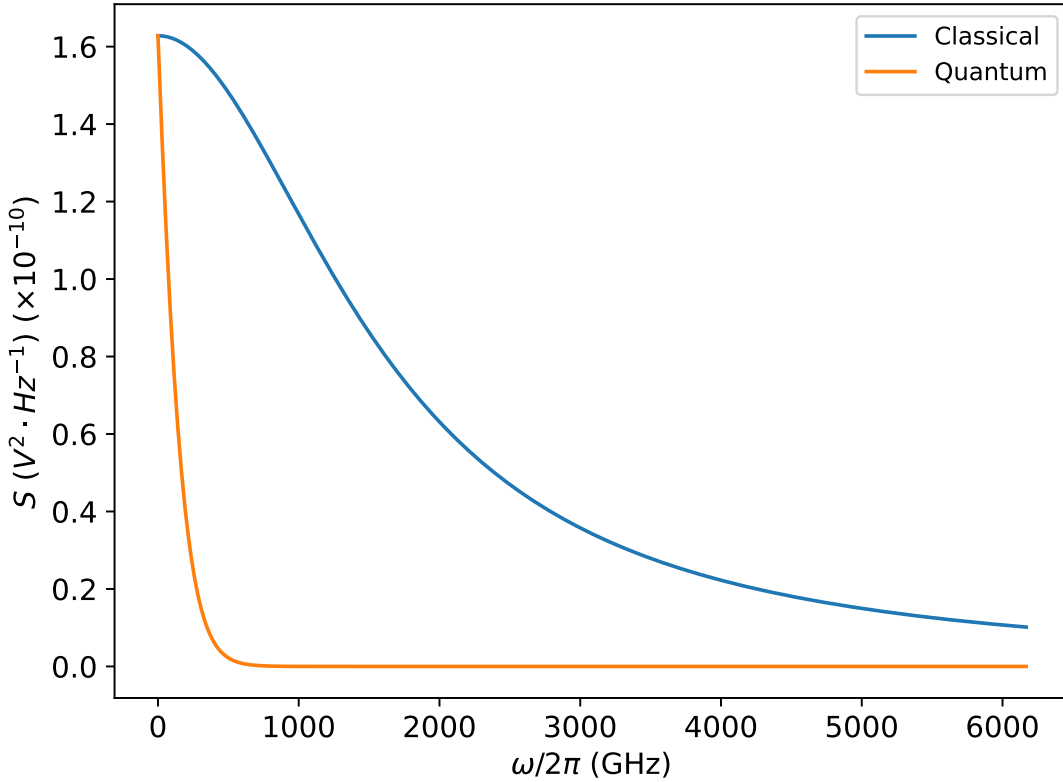
$$S_C(\omega) = 4k_B T \frac{N_G C_2}{C_1^2} \frac{\gamma}{\omega^2 + \gamma^2}, \quad (2.5)$$

where $\gamma = \frac{1}{RC_2}$ is the characteristic inverse time constant of the Lorentzian distribution and N_G is the number of gates and metal connections connected to the same bondpad, as shown in the left side of Figure A.9. The corresponding RMS voltage noise can be obtained as

$$\Delta V_{\text{rms}} = \sqrt{2\pi k_B T \frac{N_G C_2}{C_1^2}}. \quad (2.6)$$

We first looked into the effect of classical Johnson-Nyquist noise. The complete results are described in Appendix A.3.3, and we summarise here. Figure A.14 shows that both loss probability and excitation fraction significantly increase with higher cut-off frequency, γ , and higher temperature, T . We concluded that high frequency noise, especially the one that is comparable to the frequency corresponding to the characteristic energy gap, i.e. $\Delta E_{gs,2e/\hbar}$, is more harmful than low frequency noise.

(a)



(b)

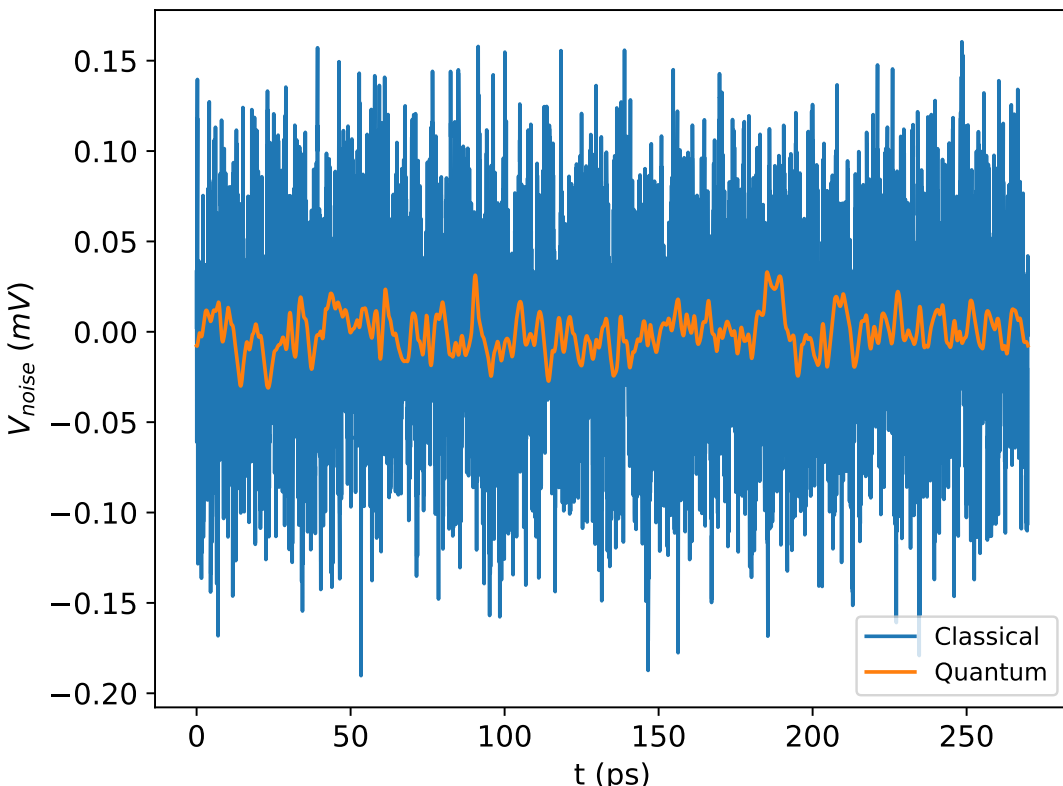


Figure 2.7: (a) the power spectral density S of the classical (blue) and quantum (orange) Johnson-Nyquist noise, and (b) random instances of classical (blue) and quantum (orange) Johnson-Nyquist noise, V_{noise} , at $T = 4$ K, and $\gamma = 10$ THz

For example, for our default setting of 4 gates per unit cell and the amplitude of the voltage signal of 100 mV, i.e. $N = 4$ and $A = 100$ mV, the resulting characteristic energy gap is around 6 meV, which corresponds to the frequency of 1.46 THz, i.e. $\Delta E_{gs,2e}/\hbar = 1.46$ THz.

In reality, quantum effects have to be taken into account once the cut-off frequency reaches $\gamma \gtrsim k_B T/\hbar$. To account for this¹, we multiply the Lorentzian power spectral density in equation 2.5 by a correction factor $\eta(\omega)$ corresponding to the ratio between the thermal mode populations in the classical and quantum cases:

$$\eta(\omega) = \frac{\hbar\omega/k_B T}{e^{\hbar\omega/k_B T} - 1}, \quad (2.7)$$

$$S_Q(\omega) = S_C(\omega)\eta(\omega). \quad (2.8)$$

The correction factor decreases from $\eta(0) = 1$ as the frequency increases, with an asymptotic value of $\eta(\omega) = 0$. Since $\eta(\omega) \leq 1$ for all frequencies, the power spectral density now deviates from the pure Lorentzian distribution with the higher frequency components more strongly suppressed. Figure 2.7a shows the classical and quantum power spectral density at a temperature of 4 K and cut-off frequency 10 THz. For a given cut-off frequency γ , we expect that the quality of shuttling will be improved relative to the corresponding classical case owing to the smaller PSD at higher frequencies. Figure 2.7b shows instances of classical and quantum noise generated with the same circuit elements at $T = 4$ K; the reduction in high-frequency noise in the quantum case is evident, and the total noise power decreases to only 5.5 % of the classical value.

Simulations of the noisy shuttling process were performed by generating random noise profiles from the power spectral density, by the procedure given in

¹There has been a debate about whether to include the zero-point fluctuations in the correction term[15], which is an additive term of $\hbar\omega/2k_B T$ to the correction factor. We found that our situation is close to an example by Kish et al.[15], a resistor connected to an antenna with a photon counter. This is because the amount of fluctuation in the voltage of the gates is *measured* by the electron shuttled underneath the gates, which acts like a photon counter in the example. Furthermore, note that spontaneous absorption doesn't exist while spontaneous emission exists due to the zero-point energy. Since the electron is absorbing energy from the gates, zero-point energy cannot be transferred to the electron, and this implies the absence of the zero-point term in the correction factor. A more detailed discussion about the inclusion of the zero-point term can be found in Kish et al.[15].

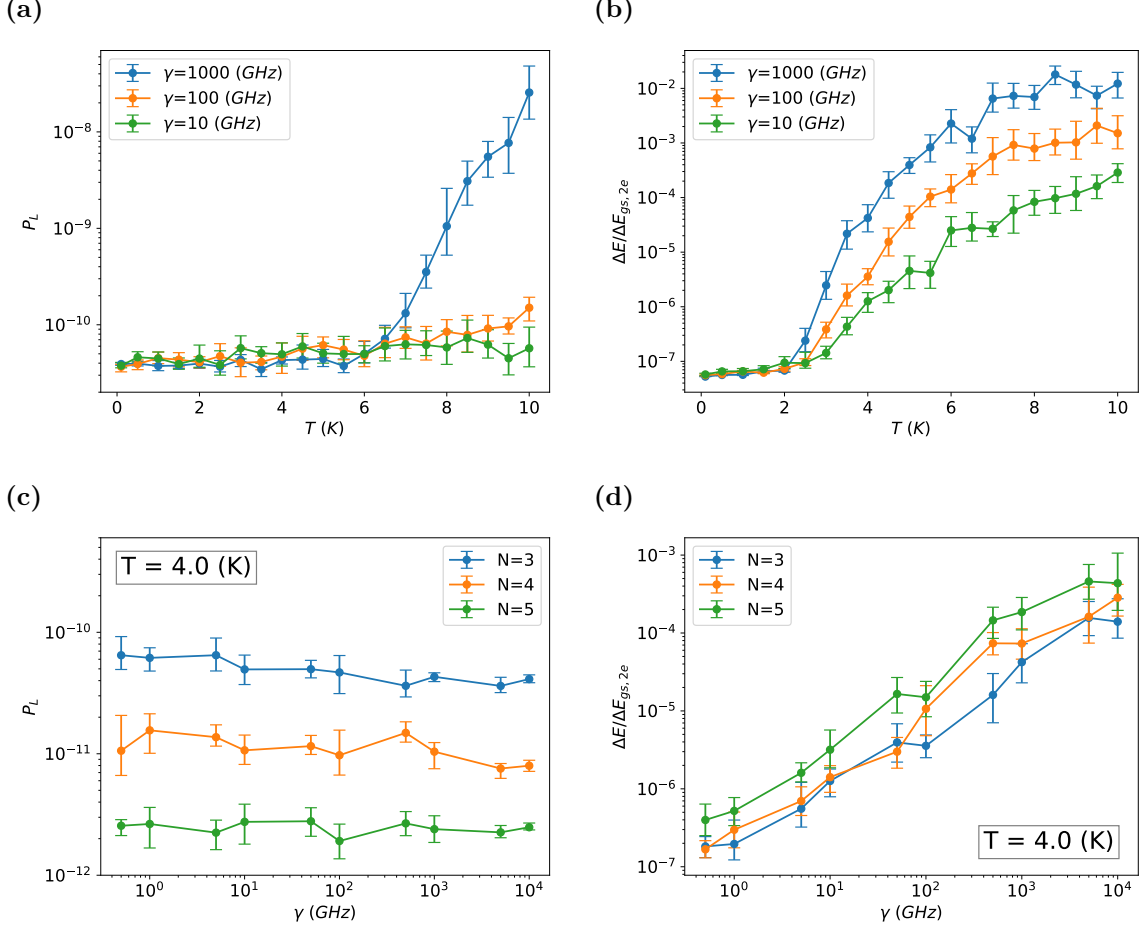


Figure 2.8: Loss probability and excitation fraction: (a, b) as a function of temperature with three different cut-off frequencies, i.e. $\gamma = 10, 100, 1000\text{GHz}$ for three gates per unit cell ($N = 3$) and (c, d) as a function of cut-off frequency γ with varying number of gates per unit cell, N .

Appendix A.2.7. The values of the circuit elements in Figure A.9 are given in appendix A.2.6. The shuttling distance was chosen to be $1.4\ \mu\text{m}$, which corresponds to 10 unit cells; thus, we assumed 10 gates are connected via a single bondpad to a single voltage source with the total capacitance of $N_G \times C_2 = 1\text{ fF}$.

Figures 2.8a and 2.8b show the loss probability and excitation fraction for three gates per unit cell, i.e. $N = 3$, at different temperatures T ranging from 0.1 K to 10 K and with varying cut-off frequencies, $\gamma = 10, 100, 1000\text{ GHz}$. For all cut-off frequencies, the excitation fraction tends to increase with temperature. However, there is highly significant increase only for $\gamma = 1000$, where loss is seen to increase by three orders of magnitude (with an appreciable climb starting at lower

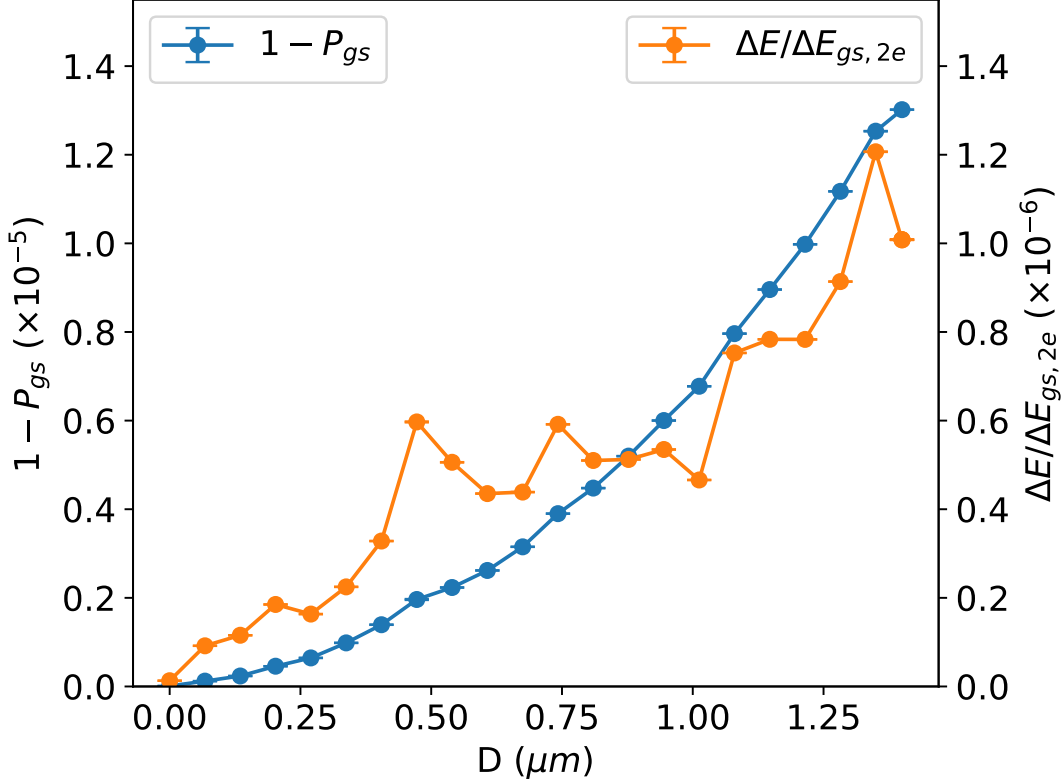


Figure 2.9: Probability of excitation outside of the ground state (blue) and excitation fraction during the shuttling (orange) for a target distance of $1.4\text{ }\mu\text{m}$ at 10 m/s . Other parameters were set as follows: The amplitude of voltage signals was 50 mV , i.e. $A = 50\text{ mV}$, the temperature was 2 K , i.e. $T = 2\text{ K}$, and there were three gates per unit cell, i.e. $N = 3$.

temperatures). The excitation fraction also increases with both temperature and γ .

However, while both loss and excitation are finite and can rise severely with temperature, the primary conclusion is that they remain practically negligible. If we make the assumption that shuttling of qubits will not occur above a 4 K , we can confirm that at this temperature there is near-ideal behaviour. One observes that P_L is always below 10^{-10} and the excitation fraction remains below 10^{-3} for all three architectural variants $N = 3, 4, 5$.

Additionally, to confirm that there is no excitation during the shuttling process, we noted down the probability to remain in the ground state and excitation fraction in the middle of shuttling. Figure 2.9 shows the probability of excitation outside of the ground state throughout the shuttling for a target distance of $1.4\text{ }\mu\text{m}$ at 10 m/s . During the shuttling, the probability of excitation was in the order of 10^{-6}

to 10^{-5} , the excitation fraction was in the order of 10^{-7} to 10^{-6} suggesting that the entire process of shuttling is largely adiabatic.

We conclude that, when high frequency components are suppressed by the correction factor, the effect of Johnson-Nyquist noise is negligible and the loss probability is comparable to the noiseless shuttling in the temperature ranges of practical interest. Furthermore, the entire process of shuttling remains adiabatic.

2.8 Sensitivity to Charge Defects

As Langrock et al.[1] pointed out, trapped charges due to impurities can affect the performance of shuttling if they occur near the interface defining the qubit layer. In this section, we investigate the effect of negative charge defects on the loss probability and excitation fraction. We used three unit cells and five electrodes per unit cell for these simulations, and the electron was shuttled across two unit cells in the presence of charge defects. Note that the trapped charges were placed in the oxide layer, and we used the permittivity of the oxide layer to compute the Coulomb peaks formed by the trapped charges. Since the oxide thickness is 10 nm (see section 2.2.), we chose the mid-point, i.e. 5 nm, as a default distance of defects from the interface. The Coulomb repulsion terms from the negatively charged defects are added to the Hamiltonian in equation 2.2:

$$H = \frac{\hbar^2}{2m^*} \mathbf{p}^2 - e\Phi(V_0(t), V_2(t), \dots, V_{N-1}(t)) + \sum_{i=1}^{N_{defects}} \frac{e^2}{4\pi\epsilon_0\epsilon_{Si}|\mathbf{r} - \mathbf{r}_i|}, \quad (2.9)$$

where $\{r_i\}_{i=1\dots N_{defects}}$ are positions of the charge defects in 3D space. Note that the motion of electron is still confined in a 2D space; The Coulomb repulsion from the static charges is calculated as if they are above (or below) the plane of motion in the 3D space.

Figure 2.10 shows the electron loss probability in the presence of varying number of charge defects. We considered a range of $N_{defects}$, the total number of charge

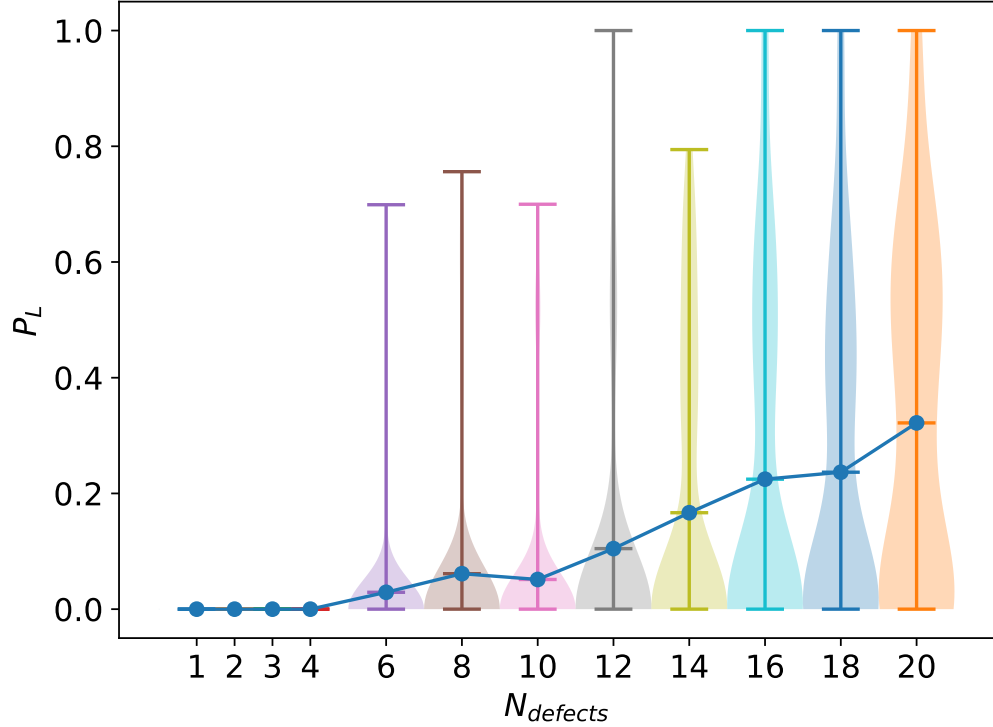


Figure 2.10: The loss probability of electron wave function with varying number of charge defects, N_{defects} , in the channel. Note that, for each number of charge defects, 100 random configurations of charges were simulated. Up to $N_{\text{defects}} = 4$, the loss probability remains nearly zero while we start to see cases with high loss probability with more than 6 defects present. The blue line connects the mean loss probability for each N_{defects} .

defects, and for each case we simulated 100 random configurations. For 4 or fewer charge defects, the loss probability remains near to zero; but this probability climbs for higher defect counts. Notably, for as few as 6 defects, we did observe at least one case where the loss probability exceeds 50% – a catastrophic failure of the shuttling channel where the electron is likely to be ejected from the confinement region.

To investigate further we explored ‘adversarial’ scenarios where we seek the worst-case positioning for a small number of defect charge(s). We initially simulate scenarios with a single trapped negative electronic charge in the centre of the channel located either 2 nm or 5 nm away from the interface, with varying shuttling speeds. We also simulated cases where two and three trapped charges are aligned at a given x-coordinate, and so are liable to form a potential wall to repel the shuttled electron. In particular, two and three charges were positioned symmetrically around

the centre axis of the channel, i.e. $y = 0$, with the distance between two adjacent charges to be 1/3 and 1/4 of the full width of the channel (100 nm), respectively.

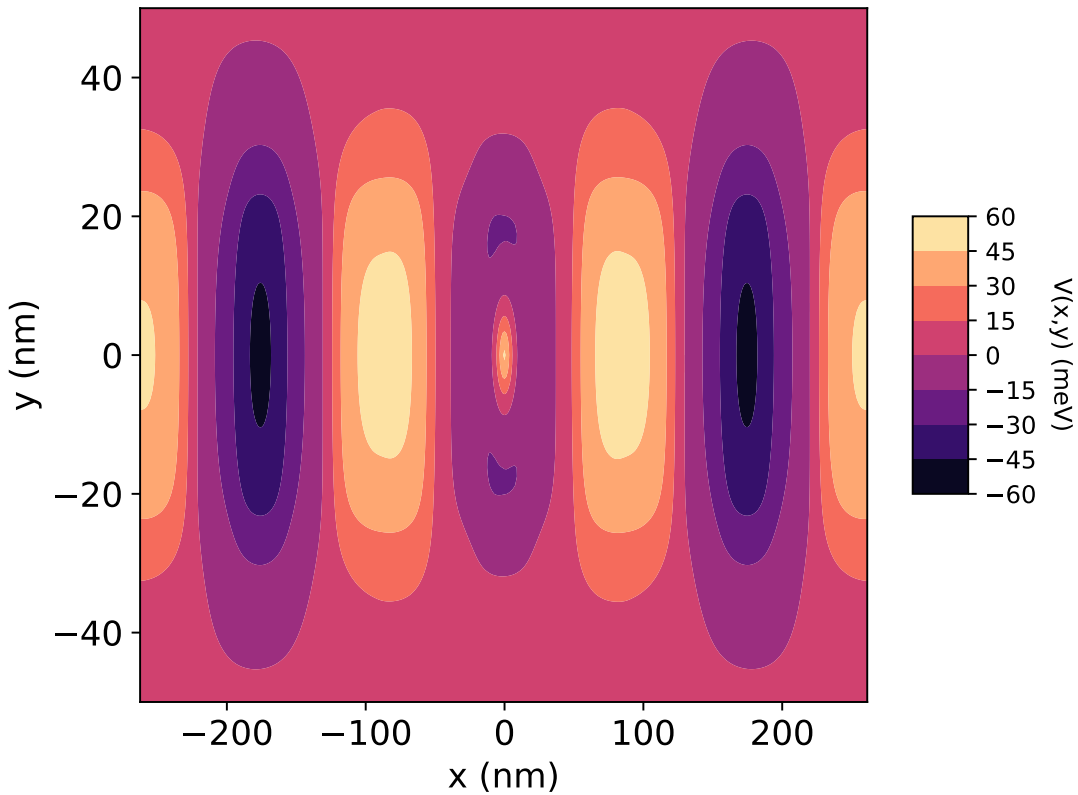
Contour plots of the potential energies with one, two, and three charges placed at 5 nm above the interface are shown in Figure 2.11 at a time where the phases of the gate voltages alone would produce a minimum in the potential energy at the charge location.

Figure 2.12a shows the probability of remaining in the ground state of the potential that would be formed by the gates alone (i.e., excluding the Coulomb potentials of the charge defects) when the shuttling speed is 10 m/s, and the shuttling distance is 350 nm (i.e., the length of two unit cells for 5 electrodes). This means the electron was shuttled from one trough to the next, i.e. from one dark oval to the next in Figure 2.11. Thus, the electron is closest to the charge defects in the middle of the shuttling at around 17.5 ns. While the transfer is still almost adiabatic for one and two charge defects, for three defects the probability to remain in the instantaneous ground state of the gate potential drops to almost zero. When the shuttled electron encounters the potential wall formed by the three charge defects, its wave functions becomes almost completely delocalized; it becomes unbound from its well in the shuttling potential. This is therefore a catastrophic failure of the shuttling process, and the device could not be used as a shuttling channel until/less the defect charges are moved.

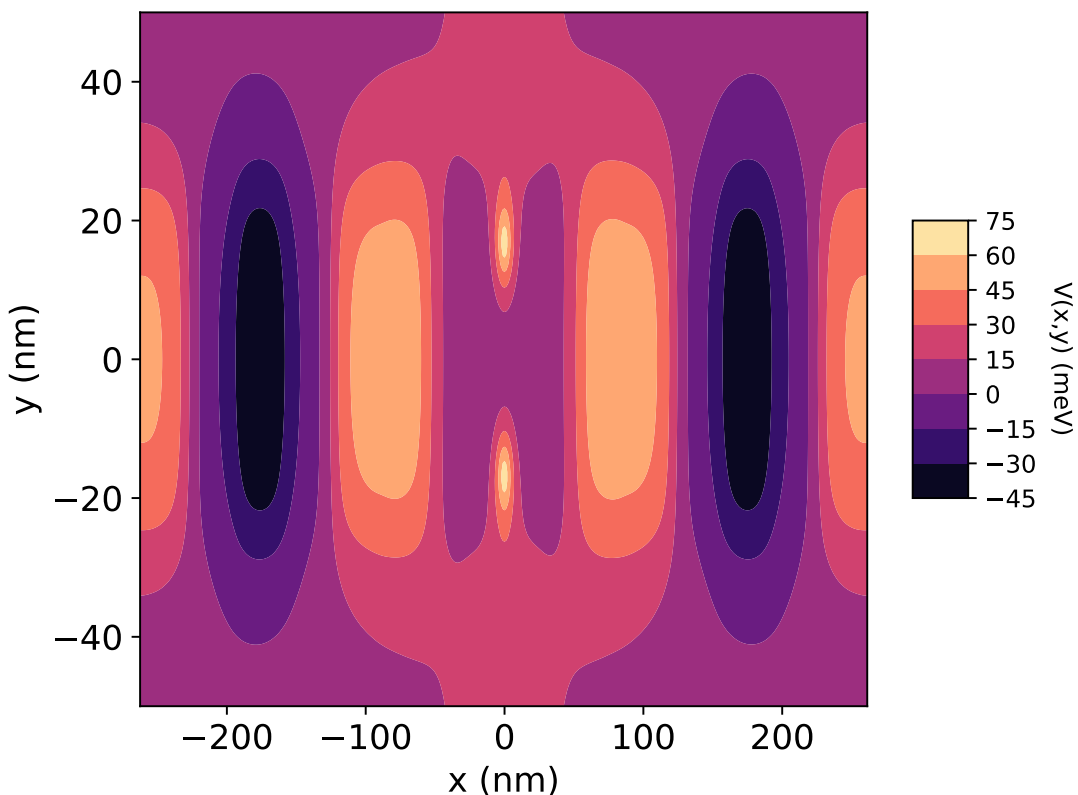
It is unsurprising (indeed inevitable) that a sufficiently adversarial scenario involving multiple trapped charges will prevent shuttling. What is more remarkable is the protocol's robustness to the cases that might, intuitively, seem very problematic – i.e. that it takes three trapped charges to ‘block’ the channel with high probability. Figure 2.12a shows that a single trapped charge or a pair of charges will imply a radical change to the instantaneous ground state, but the process can remain near-ideal. The contrast to the case of the three-charge ‘wall’ is dramatic.

We explored the worst case for the two-defect scenario. Figure 2.12b shows the loss probability and excitation of the electron for varying defect separation, i.e. Δy . Both loss measures are at their most severe at about $\Delta y = 25$ nm. However,

(a)



(b)



(c)

DRAFT Printed on December 3, 2025

even at this point the loss is only $\approx 4\%$; for separations outside a narrow 22 to 27nm range, the loss is again negligible. Figure 2.13 shows the cross-section of the potential on the $x = 0$ nm plane of figure 2.11b with varying defect separations. When the separation is small, e.g. $\Delta y = 2$ nm, the potential energy near the channel sides, e.g. $y \approx \pm 20$ nm is low enough for the electron to move around the central barrier as in Figure A.17a in appendix A.3.5. When the separation is large, e.g. $\Delta y = 30$ nm, the potential energy in the middle is low enough for the electron to pass between the repulsive peaks as in Figure A.17d in appendix A.3.5. However, at $\Delta y = 25$ nm, neither of these actions is easy: the local minima of potential energy($y = 0, \pm 25$ nm) have roughly the same values as the potential energy at the channel edges ($y = \pm 50$ nm), and the electron requires higher energy to tunnel the barrier. Thus, Figure A.17c in appendix A.3.5 shows the high energy state of the electron tunneling through the barrier.

Our simulations also confirm that charge defects closer to the shuttling channel are more harmful to shuttling at varying shuttling speeds (see Figure 2.14).

2.9 Advanced non-adiabatic ultra-fast shuttling

Our analysis has confirmed the robustness of the conveyor-belt mode of shuttling: Over the range shuttling speeds that are likely to be targeted by near- or mid-term technologies, the method evidently excels.

However, as quantum technologies mature it is possible that far greater shuttling speeds may be desirable. Therefore, in this final section we briefly explore the feasibility of an intentionally non-adiabatic shuttling method which could achieve extremely high shuttling rates, albeit with demands on voltage switching that are not practical at this time.

In Appendix A.3.2, we found that instantaneous changes in potential degrade the quality of shuttling. However, if we make such instantaneous changes at the right time, we can in principle perform shuttling with low loss and low probability of final excitation. The approach, which we informally call the ‘snap method’, consists of four steps (see Figure 2.15).

1. Make an instantaneous change (or ‘snap’) to the potential such that the minimum of potential energy is displaced to the right of the maximum of probability density by $\Delta x > 0$ (assuming that the shuttling direction is the $+x$ direction).
2. Wait for the state to propagate across the potential well, climbing up the far side so that it effectively mirrors its initial position. The total distance travelled by the wave function is $2\Delta x$. The time taken can be approximated by $\Delta t = \pi\sqrt{m/2\kappa}$, where κ is the instantaneous local curvature at the bottom of the well (assumed approximately harmonic).
3. Repeat 1 and 2 until the electron approaches the target position.
4. Once the state approaches the target position, displace the potential such that the electron will have zero momentum at the target location; finally, displace the potential such that the minimum of the potential energy is at the target position. The shuttling is complete.

Using the same numerical model, we simulated various scenarios of the snap method at different depths of the Si layer. At the depth of 30 nm below the bottom of the clavier gates, we found the loss probability as low as 10^{-6} at the shuttling speed of 500 m/s with the excitation fraction of 2×10^{-3} . While the results suggest possibility of achieving full non-adiabatic transport with low loss and excitation, the method faces various challenges. For example, making instantaneous changes of potential is bounded by the maximum rate of change of voltage at the gates, which is around 14 mV/ps in current technology. Furthermore, the presence of charge defects will change the optimal timings of the instantaneous changes of the potential. Thus, we leave this fully non-adiabatic method as a future investigation: The results and detailed analysis of the snap method can be found in Appendix A.4.

2.10 Implications for coherent qubit transport

Our numerical studies have allowed us to analyse the orbital state of the electron in various shuttling scenarios. The loss probability measures how likely it is that the scheme will transport the electron to a target position, while the excitation fraction measures the adiabaticity of the overall shuttling process. In this section we consider the implications for the spin, i.e. the degree of freedom representing the qubit.

The arguments and analysis in the study by Langrock et al.[1] are very relevant to the present section. There, the author's discusses various spin dephasing mechanisms. Spin dephasing still occurs when the shuttling is completely adiabatic in the spatial sector, because of variations in the local Zeeman splitting due to nuclear Overhauser fields and $1/f$ charge noise (which causes fluctuations in the local g-factor through spin-orbit interaction). While this effect can be mitigated by moving the electrons more quickly, averaging the local variations and leading to motional narrowing of the Zeeman splitting, fast movement makes shuttling non-adiabatic.

There are also potential sources of non-adiabaticity in shuttling: orbital excitation, both from the motion of electron and from electrostatic disorder in the QD potential. Such disorder can arise, for example, due to Ohmic heating or charge defects at the Si–SiO₂ interface. Furthermore, atomic-scale interface roughness makes the valley splitting in silicon, and the constitution of valley states, position-dependent. Shuttling the electron, so that it experiences different interface structure, therefore causes excitation in the valley degree of freedom. Such excitation into excited orbital and valley states gives rise to random phonon relaxations leading to a distribution of time spent in the excited orbital and valley states. Because of spin-orbit coupling, the g-factor depends on the orbital and valley states, and the randomness of relaxation therefore becomes a source of spin dephasing.

The excitation fraction used in our paper directly measures the amount of orbital excitation arising from the motion of the electron. For realistic parameters of $A = 50$ mV and $T = 2$ K, Figure 2.8b suggests that the excitation in the orbital degree of freedom is minimal, $\Delta E / \Delta E_{gs,2e} \sim 10^{-7}$. (Were it necessary, the Johnson-Nyquist noise can be further suppressed by using bondpads with higher capacitance

and/or bondwires with higher resistance, at the cost of slowing down the control of the qubits). Thus, in the scenarios we have explored it is likely that the spin dephasing directly due to orbital excitation is minimal. Moreover, Figure 2.9 shows the probability of excitation outside of the ground state throughout the shuttling for a target distance of $1.4\text{ }\mu\text{m}$ at 10 m/s . During the shuttling, the probability of excitation was in the order of 10^{-6} to 10^{-5} , the excitation fraction was in the order of 10^{-7} to 10^{-6} suggesting that the entire process of shuttling is largely adiabatic. This supports the claim that phonon relaxation from spatial excitation is unlikely to occur.

Spin dephasing can also occur via spin relaxation due to the motion of a QD[16], whose rate is inversely proportional to the fourth power of the characteristic energy gap[1], which is about 6 meV in our case for $N = 4$ and $A = 100\text{ meV}$. Note that the spin relaxation rate is also proportional to the square of contribution of the potential from electrostatic disorder, δV , and inversely proportional to the third power of the correlation length $l_c^{\delta V}$ [1]. Since the charge defects are closer to the shuttled electron in SiMOS than in Si/SiGe devices, the electrostatic disorder, δV , becomes bigger. Thus, there is a competition between the larger orbital splitting and stronger electrostatic disorder. Following the arguments of Langrock et al.[1], we estimate the probability of a spin flip to be around 10^{-5} with the following parameters: energy gap 6 meV , $\delta V = 73.85\text{ meV}$ (the Coulomb potential of a charged defect at a distance of 5 nm), correlation length $l_c^{\delta V} = 100\text{ nm}$, shuttling speed 10 m/s and shuttling distance $1.4\text{ }\mu\text{m}$. The probability of a spin flip is therefore negligible. However, our assumed correlation length, (100 nm , following Langrock et al.[1]) may be an overestimate as the charge defects are closer to the interface in SiMOS than in Si/SiGe, and the spin relaxation may therefore be underestimated. Further calculations are needed to make a better estimate of spin relaxation in SiMOS; we leave this to future work, as we focus on the modelling of charge shuttling in Si/SiO₂.

Our results agree with the one of the conclusions made by Langrock et al.[1]: spin dephasing is not significantly affected by the non-adiabatic effects in orbital degree of freedom. By approximating the channel as 1D, Langrock et al. calculated the excitation rate to the first excited state in the presence of electrostatic disorder

and showed that the rate is suppressed by a Gaussian factor at low speeds, i.e. $v \ll 10^{-4} \text{ m/s}$. This is in line with our results for the excitation fraction, which is no more than 3×10^{-2} in the worst case of Johnson-Nyquist noise. Furthermore, Langrock et al. showed that the phonon relaxation is fast enough for the orbital state to relax without significant spin dephasing. Using realistic parameters, Langrock et al. estimated the amount of phase error due to random phonon relaxations during the entire shuttling, which is orders of magnitude smaller than the threshold error of 10^{-3} .

We do observe more strongly non-adiabatic behaviours at higher shuttling speeds; for example peaks in loss probability and excitation fraction up to around 10^{-3} are observed at distances around $0.45 \mu\text{m}$ for shuttling speeds of 300 ms^{-1} (see Figure A.16 in Appendix A.3.4.).

2.11 Conclusions

We investigated the feasibility of conveyor-belt shuttling of an electron’s orbital state through numerical simulations. We have captured the essential physics of a SiMOS shuttling device with a 3D solution of the Poisson equation but a 2D simulation of the electron wave-packet propagation near the Si/SiO₂ interface. We use periodic boundary conditions for both potential and wave-function along the row of ‘clavier gates’ implementing the shuttling protocol, but force the electron wave function to vanish at a point within the confinement gates forming the sides of the channel. We introduced two important metrics in section 2.5 to evaluate the shuttling scenarios: the loss probability (effectively quantifying the failure of the electron to arrive at the desired location) and the excitation fraction (quantifying the non-adiabaticity of the shuttling).

Shuttling in the absence of noise was described in section 2.6. For target distance varying from 140 nm to $8.4 \mu\text{m}$, we observed loss probabilities of the order of 10^{-10} or below and excitation fraction in the order of 10^{-7} . Using three gates per unit cell rather than four, as previously proposed, would be enough to achieve this (albeit using 4 or more gates does lead to even more nearly-perfect operation).

We also simulated shuttling scenarios in the presence of Johnson-Nyquist noise. While the power spectral density of the classical Johnson-Nyquist is only valid when the energy corresponding to cut-off frequency, $\hbar\gamma$, is smaller than the energy of thermal excitation, $k_B T$, we tried both cases to clarify how much the quantum effect at low temperature and high frequency benefits the shuttling.

The results of classical Johnson-Nyquist noise are given in Appendix A.3.3. The system becomes more resilient to the noise as the number of gates per unit cell increases. We found that high frequency noise, especially the one that is comparable to the frequency corresponding to the characteristic energy gap, i.e. $\Delta E_{gs,2e/\hbar}$, is more harmful than low frequency noise. The same behaviour is observed for the excitation fraction in Figure A.14d.

In section 2.7, the results of Johnson-Nyquist noise with the quantum correction factor are given. We found the loss probability and excitation fraction are greatly suppressed by quantum effects that reduce the high-frequency noise at low temperature as shown in Figure 2.7a. We find that the most important part of the noise is that occurring at the orbital excitation frequency in the direction of the shuttling; once this frequency is above the thermal frequency, changes in temperature have a limited effect. We conclude that the Johnson-Nyquist noise can be greatly suppressed by operating at low temperatures or with a low cut-off frequency, which is achieved by having bondwires with a large resistance, R (given a fixed gate capacitance, C_2) or bondpads with high capacitance, C_1 . However, this will also limit the ability to produce fast voltage variations.

The effect of negative trapped charges near the interface on the shuttling was investigated, and the results are given in section 2.8. We first looked into varying number of charge defects and found that loss probability was near zero up to four charge defects at random positions. To gain more insight, we looked into ‘adversarial’ scenarios with a single trapped charge, two charges, or three charges positioned symmetrically around the centre of the channel. In the case of two and three charges, the Coulomb peaks can form a potential wall that repels the electron. We showed that the electron wave function was easily completely delocalized in

the presence of three such trapped charges while the shuttling was remarkably successful in the presence of one and two trapped charges (with a small risk of loss in the two-defect case) . Furthermore, we confirmed that a shorter distance from the trapped charges from the interface and higher shuttling speeds harmed the shuttling more, as expected from the adiabatic theorem.

In section 2.9, we proposed a new non-adiabatic shuttling method, which allows fast shuttling with low loss probability. Despite our observation (see Appendix A.3.2) that instantaneous changes of the potential are detrimental to conventional adiabatic shuttling, we leverage the idea that *properly timed* instantaneous changes can drive a coherent shuttling process. At the appropriate instant, the electron’s wavefunction is a well-behaved coherent state in both the ‘before’ and ‘after’ potentials. The interval between the sudden changes, hence the shuttling speed, depends potential curvature near the minimum and the number of instantaneous updates per unit cell as shown in Figure A.18. We found that there is a trade-off with this method as a function of depth below the electrodes: for deeper shuttling, the quantum dot becomes shallower, but also more nearly harmonic. For our reference voltage pulse amplitude (100 mV) we find the optimum depth is around 30 nm.

In section 2.10, we assess the impact of our results on the fidelity of spin transport. We find that the effect of random phonon-relaxation due to excitation of the orbital state would be minimal for the conveyor-belt shuttling.

Overall, we conclude that the Conveyor-belt shuttling is so adiabatic that the excitation fraction is smaller than 10^{-3} and loss probability is smaller than roughly 5×10^{-9} even if we have only three gates per unit cell, in a reasonable temperature range $T \lesssim 4$ K, at shuttling speeds up to 500 m/s, and in the amplitude range of 50 mV to 100 mV, in the presence of quantum Johnson-Nyquist noise. However, charge defects due to impurities can damage the shuttling if such defects form a repulsive potential wall in the middle of channel and delocalize the electron wave function.

Our approach is complementary to that of Langrock et al.[1] who solved Poisson-Schrödinger equations to see the formation of quantum dots in the presence of

charge defects, whereas we modelled the effect of charge defects by doing explicit time-dependent simulations of electron wave function on these potentials. While the Si/SiGe structure considered by Langrock et al. has the charge defect plane far apart from the shuttling channel (around 45 nm), the Si/SiO₂ structure considered in this paper is affected by charge defects more severely as the charge defect plane is closer to the channel (5 nm in our typical simulations). As a topic for further study, we expect that 3D simulations may result in improved loss probability and excitation fraction compared to the 2D simulations performed in this paper as wave function has one more spatial direction to circumvent the potential barrier.

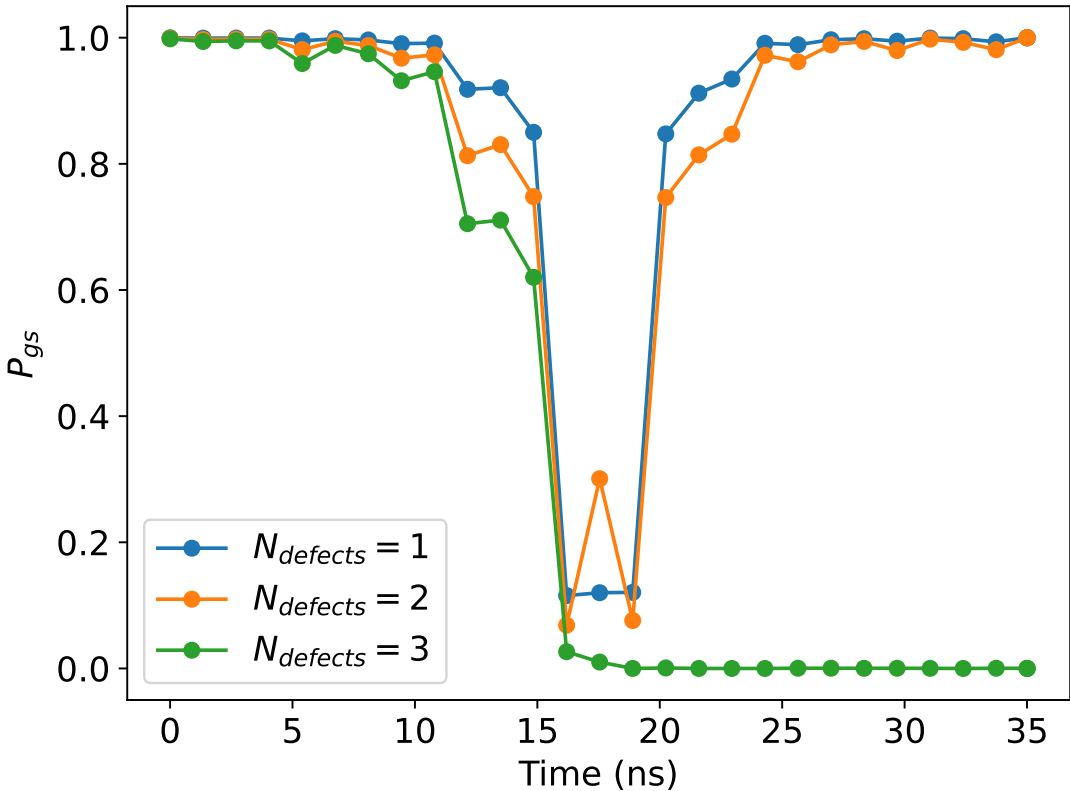
Similar charge modelling of bucket-brigade shuttling was performed by Buonacorsi et al.[17] and Krzywda et al.[18]. Buonacorsi et al.[17] reported the infidelity between the final state of shuttling and orbital ground state as low as 10⁻⁵ for a dot-to-dot transfer, and Krzydwa reported the charge transfer error as below as 10⁻⁷ for a dot-to-dot transfer. While the charge shuttling with bucket-brigade was shown to be still reliable for short distances of a few interdot distances, roughly a few 100 nm, shuttling of longer distances, e.g. a few micrometres, has not been simulated: Furthermore, bucket-brigade suffers from reversal of the shuttling direction once the dot-to-dot transfer fails. In contrast, we simulated conveyor-belt shuttling in the presence of Johnson-Nyquist noise for a distance of 1.4 μm and found nearly perfect loss probability below 5×10^{-9} and excitation fraction below 10⁻³. However, we do acknowledge that charge defects can hinder the reliable conveyor-belt shuttling of electron in some adversarial cases.

Further investigation for the charge modelling could be made to find the effect of trapped charges randomly placed near the interface due to impurities. Even though we looked into the worst case of three charges forming a repulsive potential wall, we have not yet determined the statistical probability that a given charge *density* will disable a shuttling channel of a given length. It may also be interesting to ask whether any modification of the shuttling protocol can improve the robustness versus the charge defect environment. Finally, it would be helpful to investigate

the effect of positive charge defects near the interface. Positive charge defects may trap the shuttled electron and form a bound state.

In this paper we have explored the dynamics of charge shuttling directly through numerically-intensive granular grid-based modelling of the 2D wavefunction, and then argued how the observed behaviour can be expected to affect qubit integrity. The natural next stage for a further study is to equip the model with spin and valley degrees of freedom so as to observe the qubit's evolution directly. For this to be meaningful, numerical models of state/position-dependent g-factor and atomic scale interface roughness are necessary and this is an exciting challenge.

(a)



(b)

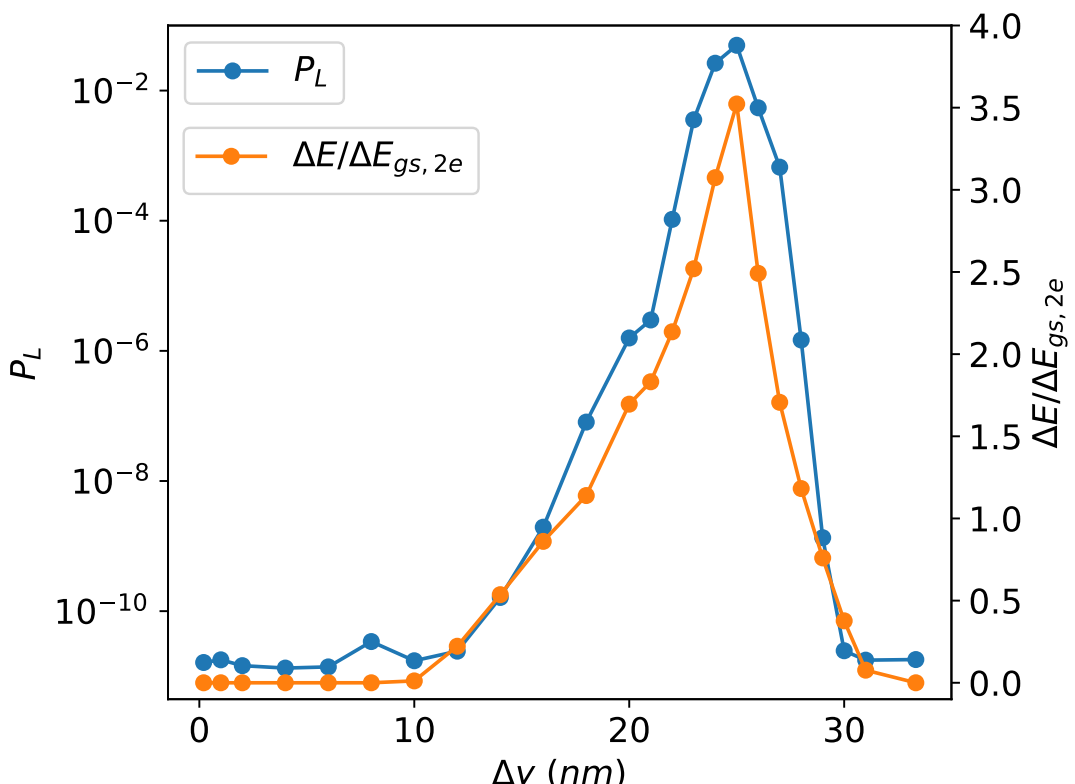


Figure 2.12: (a) The probability to remain in the instantaneous ground state of the potential formed by the gates alone for a shuttling speed of 10 m/s and varying numbers of charge defects, $N_{defects}$: one (blue), two (orange), and three (green). The electron is closest to the defects in the middle of the shuttling. Note that, for one and two

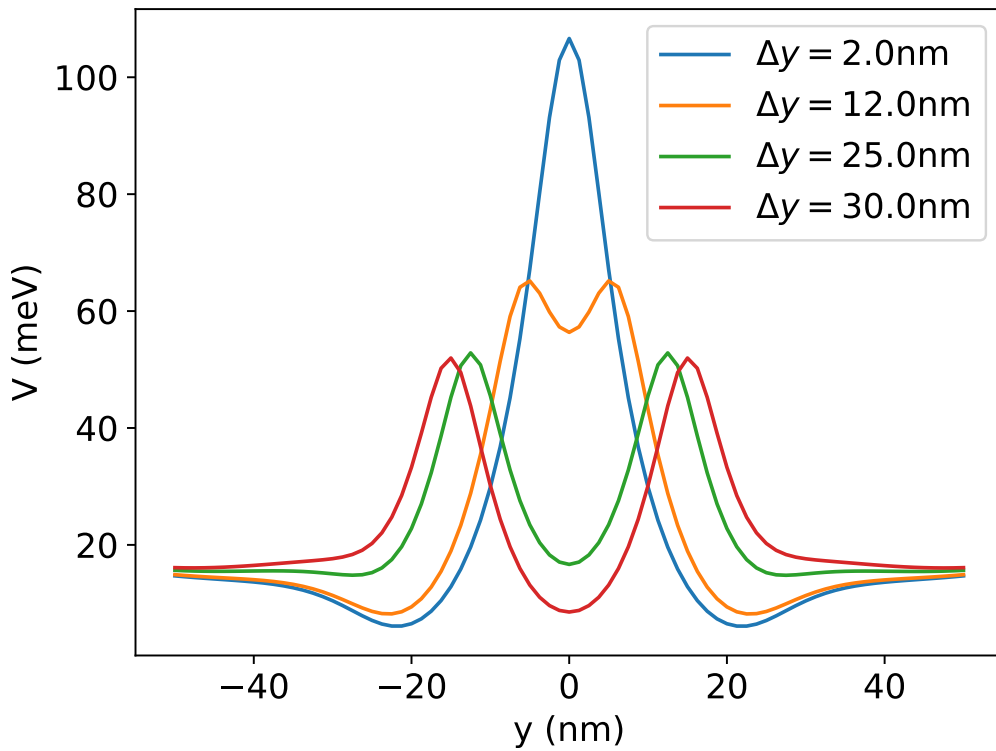


Figure 2.13: The cross-section of the potential in the xz plane (at $x = 0$ nm in Figure 2.11b) in the presence of two charge defects of varying separations $\Delta y = 2, 12, 25, 30$ nm. Each defect has charge of $-e$.

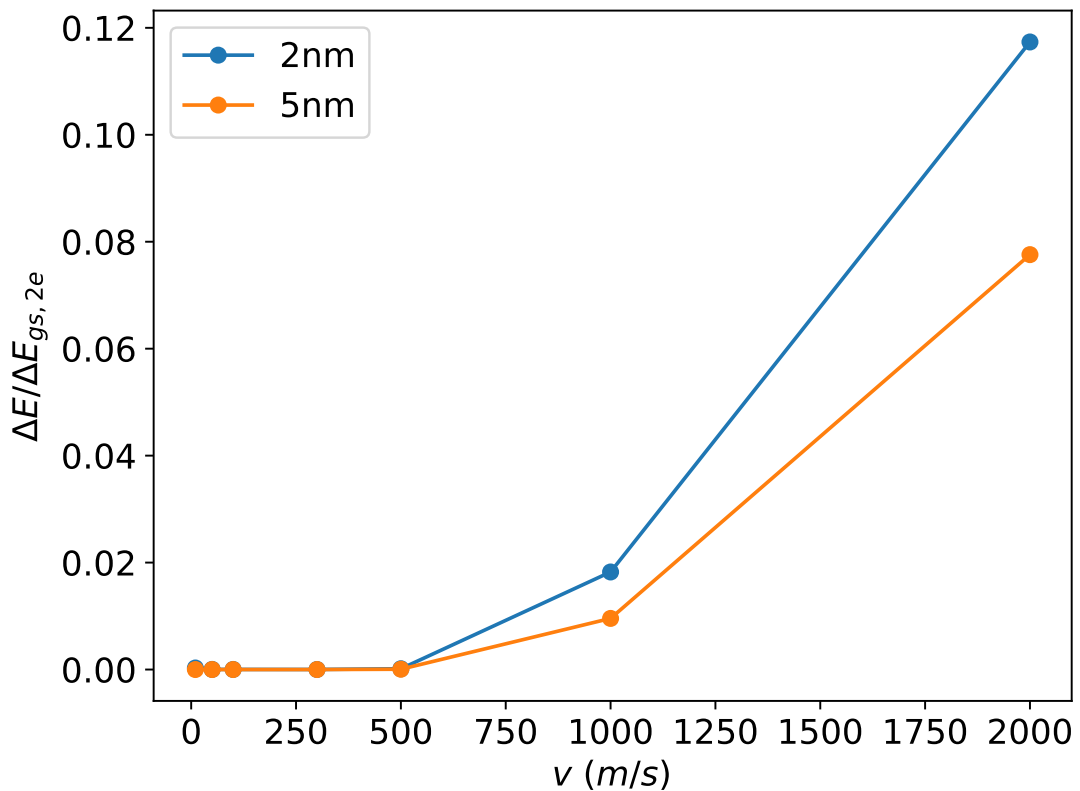


Figure 2.14: The excitation fraction with various shuttling speeds when one charge defect is present. The blue and orange lines correspond to excitation fraction when the charge defect is 2 nm and 5 nm away from the interface.

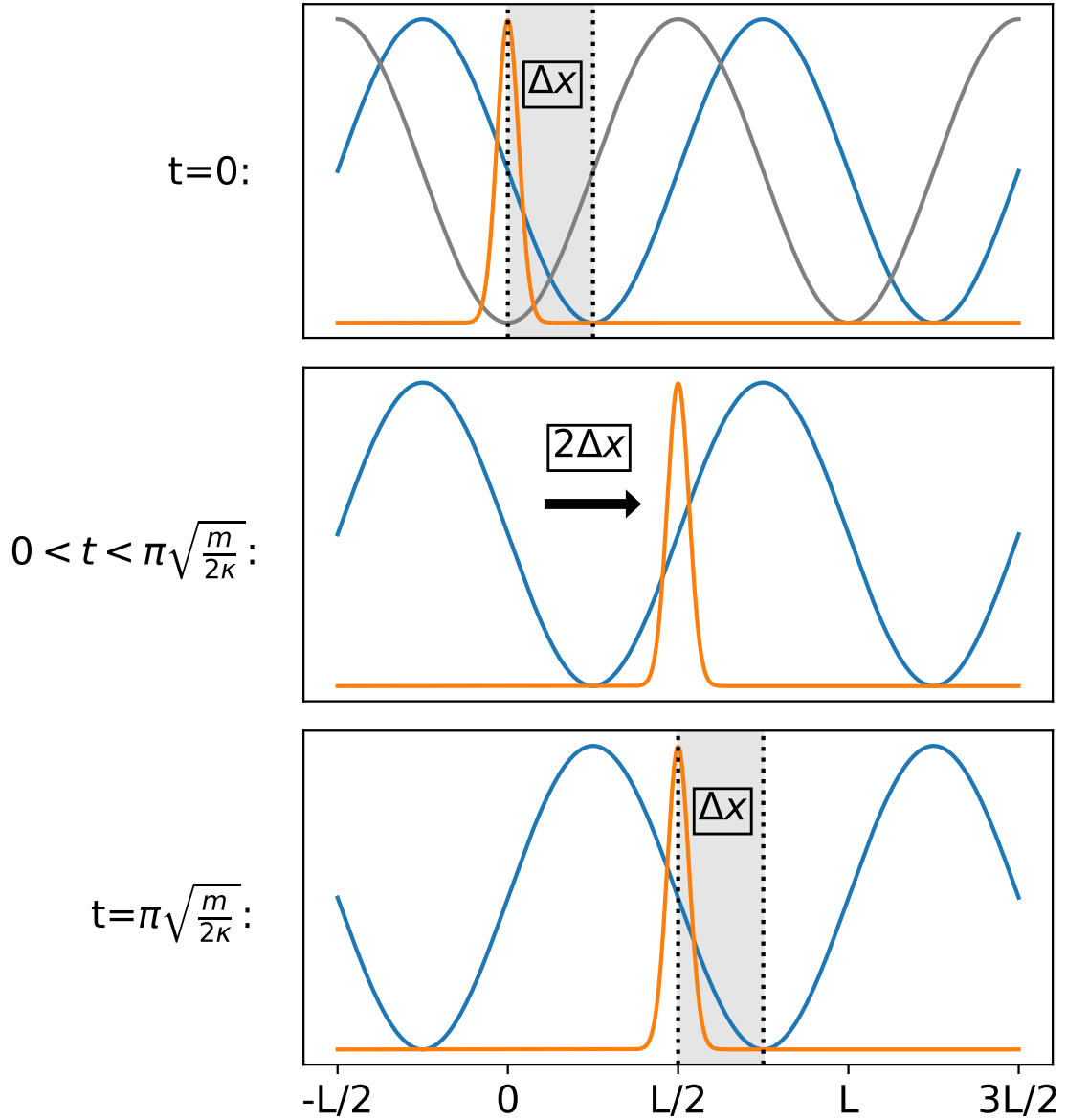


Figure 2.15: The illustration of snap method, where the blue line corresponds to the potential energy, the orange line corresponds to the probability density. Shaded regions were applied when instantaneous changes of the potential energy with displacement Δx were made. The grey line at the $t = 0$ panel represents the potential energy at $t < 0$. In the first panel, the potential is instantaneously shifted to the right by Δx . In the second panel, the potential is static until the wave function has evolved to the other side of the well and comes to a halt. In the last panel, the potential is shifted again to the right by the same amount, Δx . This process continues until the target distance of shuttling is achieved. The time it takes for the electron wavefunction to curl up the other side of the well depends on the local curvature, κ , at the bottom of the well.

*Alles Gescheite ist schon gedacht worden.
Man muss nur versuchen, es noch einmal zu denken.*

*All intelligent thoughts have already been thought;
what is necessary is only to try to think them again.*

— Johann Wolfgang von Goethe
[von_goethe_wilhelm_1829]

3

Noise-aware Time-optimal Quantum Control

Contents

3.1	Introduction	41
3.2	Time Optimisation in Quantum Optimal Control	43
3.2.1	Chopped Random Basis (CRAB)	43
3.2.2	Noisy Simulation of CRAB	45
3.2.3	Implementation of Time-optimised CRAB	48
3.3	Numerical Simulations	49
3.3.1	State-to-State Transfer	49
3.3.2	Gate Compilation	52
3.4	Discussion	55
3.5	Conclusion	57

3.1 Introduction

Quantum optimal control, which is the process of designing control pulses or sequences that achieve desired quantum dynamics, is central to the practical implementation of many quantum technologies [19], such as quantum communication [20, 21], quantum sensing [22, 23], state preparation [24–29] and gate compilations [30–33]. Many different quantum optimal control techniques have been developed, ranging from techniques that iteratively refine control pulses based on

gradients of the cost function like gradient ascent pulse engineering (GRAPE) [34] and Krotov method [35], to techniques that try to reduce the parameter search space using chopped random basis (CRAB)[36]. Due to the advent of artificial intelligence, there are also many works trying to integrate machine learning into the pipeline [37–50]. In addition, there were also proposals using quantum-classical methods [51, 52], and such techniques have been applied to both open and close quantum systems [38, 53–56].

Pulse duration (evolution time) is one of the most important aspects in control pulse optimisation, which brings about a series of theoretical frameworks for time-optimal quantum control, for example, using Pontryagin’s Maximum Principle (PMP) [57–64], Quantum Brachistochrone (QB) [65–70], geometric approach [71–74], information-theoretic approach [75–77], and Lie algebraic approach [71, 78]. These analyses usually assume noiseless quantum systems and are interested in the theoretically achievable control pulse rather than what can be found via optimisation in practice. Under such context, they are interested in finding the minimum time required to reach a target state or perform a target gate with 100% fidelity. Such a lower bound on the time required is also called the quantum speed limit, which has been studied in several notable numerical simulations [24, 32, 79] and experiments [80–82].

However in practice, when trying to implement the control pulses in actual quantum devices for the purpose of e.g. state preparation or gate optimisation, there will inevitably be noise in our quantum system, which is not taken into account in the aforementioned studies. Furthermore in practice, pulse optimisation can be stuck in different local traps given different pulse durations. Both of these factors mean that 100% fidelity is not achievable in practice and the minimal time derived in theory to reach this perfect fidelity is not necessarily the actual optimal time. There has been a range of impactful works that looked into potential ways to incorporate noise into quantum optimal control [53, 54, 56, 83]. However in these protocols, the noisy quantum system simulation required is much more expensive than its noiseless counterpart, and explicit optimisation for the pulse

duration is also not included. In this article, we show that under certain noise conditions (including practical examples under depolarising noise, dephasing noise and dipole dipole noise), we have a way to efficiently perform one of the most practical quantum optimal control protocols, CRAB, at a similar cost as noiseless simulation, thus allowing us to perform optimisation on a system that has two times more qubits compared to before. Such efficient inclusion of noise in our simulation also allows us to perform direct optimisation for the pulse duration to maximise the fidelity reachable in practice, rather than simply searching for the theoretically possible shortest time as before.

This article is organised as follows. In Sec. 3.2, we present a way to efficiently perform noisy CRAB under certain noise conditions and then outline our methods for performing optimisation on the pulse duration. In Sec. 3.3, we perform numerical simulations of state-to-state transfer and gate compilation for different physical systems using our time-optimised CRAB method, which is followed by discussions on the importance of such time optimisation in Sec. 3.4. At the end in Sec. 3.5, we summarise our results and list out the many interesting directions for further investigation.

3.2 Time Optimisation in Quantum Optimal Control

3.2.1 Chopped Random Basis (CRAB)

In the state-to-state transfer problem, our goal is to arrive at the target state $|\psi_g\rangle$ from the initial state $|\psi_0\rangle$, using a time-independent Hamiltonian generated by the set of basis $\{H_i\}_0^{N_H}$:

$$H(t) = H_0 + \sum_{i=1}^{N_H} f_i(t) H_i. \quad (3.1)$$

This Hamiltonian is completely determined by the set of pulses, $\{f_i(t)\}_{i=1}^{N_H}$. The quantum state will evolve from the initial state following the time-dependent Schrödinger equation with the Hamiltonian $H(t)$, giving rise to the final state, $|\psi_f\rangle$.

In Eq. (3.1), the time-independent term, H_0 , is called the *drift Hamiltonian* while the other part is called the *control Hamiltonians*.

Our goal is to find the set of pulses, $\{f_i(t)\}$, that maximises fidelity between the final state and the target state,

$$F = |\langle \psi_f | \psi_g \rangle|^2. \quad (3.2)$$

Caneva et al.[84] developed a quantum optimal control method called the Chopped Random Basis(CRAB), where the control pulses, $\{f_i\}_{i=1}^{N_H}$, are expressed in terms of truncated Fourier basis:

$$f(t; \vec{\alpha}, \vec{\omega}) = \alpha_0 + \sum_{m=1}^M \alpha_{-m} \cos(\omega_m t) + \alpha_m \sin(\omega_m t), \quad (3.3)$$

where $\vec{\omega}$ is a vector of frequencies randomly drawn around the principal harmonics [84]. The k th frequency is defined as $\omega_k = 2\pi k(1 + r_k)/T$, where r_k is drawn from a uniform distribution in the range of $-0.5 \leq r_k \leq 0.5$ and $k = 1, \dots, M$.

Given some control pulses, $\{f_i\}_{i=1}^{N_H}$ and time duration T , the control unitary becomes

$$U(T, \vec{\alpha}) = \mathcal{T} \exp \left\{ -i \int_0^T dt (H_0 + \sum_{i=1}^{N_H} f_i(t; \vec{\alpha}_i, \vec{\omega}_i) H_i) \right\}. \quad (3.4)$$

In some of the experiments in Ref. [84], the evolution time T was chosen to be inversely proportional to the energy scale, with an arbitrarily selected constant. In some other experiments in Ref. [84], T is fixed to be twice the minimum time set by the quantum speed limit. This leaves only $\vec{\alpha}$ as free parameters for optimisation, i.e. $U(T, \vec{\alpha}) \rightarrow U(\vec{\alpha})$.

In the absence of noise, the final output state is $|\psi_f\rangle = U(\vec{\alpha}) |\psi_0\rangle$ and its state fidelity with respect to the target state is

$$F_U(\vec{\alpha}) = |\langle \psi_g | U(\vec{\alpha}) | \psi_0 \rangle|^2 = |\langle \psi_g | \psi_f \rangle|^2. \quad (3.5)$$

CRAB uses the fidelity $1 - F_U(\vec{\alpha})$ as a cost function to optimise the free parameters, $\vec{\alpha}$, often with additional constraints on the parameter depending on the problem.

3.2.2 Noisy Simulation of CRAB

So far we have not considered noise in the quantum system, but noise is unavoidable in practice. Directly trying to incorporate noise into the CRAB optimisation will simply make the simulation exponentially more expensive with respect to the number of qubits, since a N -qubit noisy mixed state simulation is equivalent to an $2N$ -qubit pure state simulation. In the presence of Markovian noise, instead of following the time-dependent Schrödinger equation, the evolution of the state will follow the Lindblad master equation

$$\frac{d}{dt}\rho = \underbrace{-i[H, \rho]}_{\text{unitary part}} + \underbrace{\sum_{k=1}^{4^N-1} \gamma_k \left(L_k \rho L_k^\dagger - \frac{1}{2} \{ L_k^\dagger L_k, \rho \} \right)}_{\text{dissipative part}} \quad (3.6)$$

where $\{L_k\}$ are the jump operators that describe the noise process. As explicitly shown in Sec. B.1, we can vectorise the density operator to write the Lindblad master equation in the Liouville superoperator form [85]:

$$\frac{d}{dt}|\rho\rangle\langle\rho| = \mathcal{L}|\rho\rangle\langle\rho| = (\mathcal{L}_H + \mathcal{L}_D)|\rho\rangle\langle\rho| \quad (3.7)$$

where \mathcal{L}_H represent the Liouville operator of the unitary part and \mathcal{L}_D represent the Liouville operator of the dissipative part. For simplicity, we will consider the case in which both \mathcal{L}_H and \mathcal{L}_D are time-independent. In this case, with an incoming state $\rho_0 = |\psi_0\rangle\langle\psi_0|$, the resultant noisy state at time T is simply given by:

$$|\rho_{f,\text{noi}}\rangle\langle\rho_{f,\text{noi}}| = e^{(\mathcal{L}_H + \mathcal{L}_D)T}|\rho_0\rangle\langle\rho_0|$$

and its fidelity against the target *pure* state $|\rho_g\rangle\langle\rho_g| = |\psi_g\rangle\langle\psi_g|$ is given as

$$\text{Tr}(\rho_g \rho_{f,\text{noi}}) = \langle\langle \rho_g | \rho_{f,\text{noi}} \rangle\rangle = \langle\langle \rho_g | e^{(\mathcal{L}_H + \mathcal{L}_D)T} | \rho_0 \rangle\rangle.$$

Evaluating this fidelity requires full simulation of mixed state vectors of dimension 4^N over many time steps, which as mentioned, is exponentially more expensive than the pure state simulation of dimension 2^N required for the noiseless case in Eq. (3.5).

In order to reduce the computational cost, we will consider the case in which the unitary part and the dissipative part commute. As shown in Sec. B.1, a sufficient condition is

$$[H, L_k] = a_k L_k \quad \forall k \quad \Rightarrow \quad [\mathcal{L}_H, \mathcal{L}_D] = 0 \quad (3.8)$$

for some set of real number $\{a_k\}$. Physically, this means that the jump operator L_k will map one eigenvector of H to another eigenvector. While preserving the eigenbasis of H , the jump operators do not preserve the norm of the eigenstates, causing the decay of the states towards the origin of the Bloch sphere.

Do note that Eq. (3.8) is just a sufficient condition and thus is not the only way to ensure the unitary part and the dissipative part commute. When the jump operators are Pauli operators, they will generate Pauli noise channels that are diagonal in the Pauli transfer matrix formalism [86]. For such Pauli noise, another (not mutually exclusive) way for the unitary and dissipative part to commute is to have \mathcal{L}_H block diagonal in the same way as the degenerate subspaces of \mathcal{L}_D as shown in Eq. (B.8).

When \mathcal{L}_H and \mathcal{L}_D commutes, the output fidelity can be written as

$$\langle\langle \rho_g | \rho_{f,\text{noi}} \rangle\rangle = \langle\langle \rho_g | e^{\mathcal{L}_D T} e^{\mathcal{L}_H T} | \rho_0 \rangle\rangle = \langle\langle \rho_{g,\text{noi}} | \rho_f \rangle\rangle \quad (3.9)$$

with

$$|\rho_f\rangle\rangle = e^{\mathcal{L}_H T} |\rho_0\rangle\rangle \quad (3.10)$$

$$|\rho_{g,\text{noi}}\rangle\rangle = (e^{\mathcal{L}_D T})^\dagger |\rho_g\rangle\rangle. \quad (3.11)$$

Here $\rho_f = |\psi_f\rangle\langle\psi_f|$ is the noiseless final state we have before. Note that we have assumed that \mathcal{L}_H is time-independent so far, but the same expression $\langle\langle \rho_g | \rho_{f,\text{noi}} \rangle\rangle = \langle\langle \rho_{g,\text{noi}} | \rho_f \rangle\rangle$ is obtained even if \mathcal{L}_H is time-dependent, with the only change that $|\rho_f\rangle\rangle$ is now a state dependent on the pulse parameters $\vec{\alpha}$ as described in Sec. 3.2.1. The condition in Eq. (3.8) needs to hold for all t , but in practice, we simply check in against all of the subterms in the Hamiltonian in Eq. (3.1). If the jump operators are Hermitian or anti-Hermitian, then $e^{\mathcal{L}_D T}$ will be self-adjoint

and thus we have $|\rho_{g,\text{noi}}\rangle\rangle = e^{\mathcal{L}_D T} |\rho_g\rangle\rangle$ being simply the noisy target state that undergoes the same noise channel.

Hence, we can obtain an estimate of the noisy fidelity by simply performing 2^N -dimensional pure state simulation in the same way as in Sec. 3.2.1 to obtain the noiseless output state $\rho_f = |\psi_f\rangle\langle\psi_f|$, then we can obtain the noisy fidelity by measuring the modified observable $\rho_{g,\text{noi}}$ on the noiseless state. The form of the observable $\rho_{g,\text{noi}}$ is independent of the control pulses and thus can be calculated beforehand before all of the pulse optimisations. As shown in Sec. B.2, under Pauli noise, we can write out the exact T -dependence for observable $\langle\langle\rho_{g,\text{noi}}(T)|$

$$\langle\langle\rho_{g,\text{noi}}(T)| = 2^{-N} \sum_j e^{-\lambda_j T} \langle\langle\rho_g|G_j\rangle\rangle \langle\langle G_j|,$$

which allows for a simpler calculation of $\rho_{g,\text{noi}}(T)$ at different T . Here $\{G_j\}$ is the Pauli basis, and λ_j is a real number determined by the set of jump operators that anti-commute with G_j . We can further simplify the sum above by truncating it to include only terms with significant value of $e^{-\lambda_j T} \langle\langle\rho_g|G_j\rangle\rangle$. Performing simulation in the way outlined above is significantly cheaper than performing 4^N -dimension noisy simulation using the Lindblad master equation through all the time steps to obtain $\rho_{f,\text{noi}}$ for every iteration of pulse optimisation.

Using the expression of $\langle\langle\rho_{g,\text{noi}}(T)|$ for Pauli noise above, we see that the output fidelity will decay in a multi-exponential manner

$$\begin{aligned} F(T, \vec{\alpha}) &= \langle\langle\rho_g|\rho_{f,\text{noi}}(T, \vec{\alpha})\rangle\rangle = \langle\langle\rho_{g,\text{noi}}(T)|\rho_f(T, \vec{\alpha})\rangle\rangle \\ &= 2^{-N} \sum_j e^{-\lambda_j T} \langle\langle\rho_g|G_j\rangle\rangle \langle\langle G_j|\rho_f(T, \vec{\alpha})\rangle\rangle \end{aligned}$$

where we have written out explicitly the T and $\vec{\alpha}$ dependence of the different components. In practice, many of these λ_j can share very similar values, enabling us to group many of these decay terms. In particular, we have shown in Sec. B.2 that for a particular type of Pauli channel we call group channel [87], the fidelity will decay with a single exponential curve. One example of such a group channel

is the global depolarising channel, whose fidelity decay follows

$$\begin{aligned} F(T, \vec{\alpha}) &= \langle\langle \rho_g | \rho_{f,\text{noi}}(T, \vec{\alpha}) \rangle\rangle \\ &= e^{-\lambda T} F_U(T, \vec{\alpha}) + 2^{-N}(1 - e^{-\lambda T}). \end{aligned} \quad (3.12)$$

with $F_U(T, \vec{\alpha})$ being the noiseless fidelity given in Eq. (3.5).

3.2.3 Implementation of Time-optimised CRAB

After being able to more efficiently implement CRAB in the presence of noise, the natural competition between the noise, which favours shorter evolution time, and the quantum speed limit, which favours longer evolution time, will call for the need to optimise along the time direction. This brings us to time-optimised CRAB (TCRAB) in which we try to maximise $F(T, \vec{\alpha})$ over both T and $\vec{\alpha}$. The first possibility is to optimise T and $\vec{\alpha}$ in separate and alternating rounds. However, as shown in Sec. B.4.1, the T optimisation performed after full $\vec{\alpha}$ optimisation tends to get stuck in local minima. Hence, we instead turn to a global optimiser called basin-hopping, for simultaneous optimisation of T and all parameters in $\vec{\alpha}$. Basin-hopping is a two-step optimisation method combining global search and local optimisation, ideal for rugged, funnel-shaped energy landscapes [88]. L-BFGS-B [89], a variant of limited-memory BFGS [90], was used as the local optimiser in our case.

It is also possible to perform TCRAB using root-finding methods. With a fixed evolution time T , we can obtain the optimised parameters $\vec{\alpha}_T$ that achieve the highest possible fidelity using CRAB for the given T

$$F_{\text{opt}}(T) = F(T, \vec{\alpha}_T) \quad (3.13)$$

Hence, finding the optimal evolution time is simply identifying the maxima in $F_{\text{opt}}(T)$, which can also be solved by performing root-finding methods on its derivative $\dot{F}_{\text{opt}}(T)$. The derivative here can be estimated using finite difference. In this article, the *bisection method* is used as an example of root-finding methods to find the optimal evolution time. Using root-finding methods will return a maximum of $F_{\text{opt}}(T)$, but it is not necessarily the global maximum. However, as we will see in

our examples later, some $F_{\text{opt}}(T)$ are actually concave, allowing us to obtain the global maximum using the bisection method, while in many other cases, we can reach a local minimum that still has very high fidelity F_{opt} close to the global maximum. The detailed implementations and hyper-parameters used in our simulations are all outlined in Sec. B.4. Note that by global maximum here, we mean the global maximum for $F_{\text{opt}}(T)$ along the T direction. It is not guaranteed to be the global maximum for the whole parameter space since it is subject to the efficiency of the optimisation in CRAB. All of our mentions of the global optimal time in this article are subject to the same constraints.

3.3 Numerical Simulations

3.3.1 State-to-State Transfer

Entanglement Generation

We will present our simulation results to benchmark CRAB and TCRAB for a series of state-to-state transfer and gate compilation tasks. The first example is an entanglement generation for the two capacitively coupled Josephson charge qubits in a depolarising channel. The two qubits are initialised as $|00\rangle$, and the target state is set to be a bell pair, $|\Psi^+\rangle = (|00\rangle + |11\rangle)/2$.

As noted in Caneva et al.[84], the Hamiltonian of two capacitively coupled Josephson charge qubits is

$$H(t) = \sum_{i=1,2} (E_C \sigma_i^z + E_J \sigma_i^x) + E_{cc}(t) \sigma_1^z \sigma_2^z. \quad (3.14)$$

We set $E_J = -E_C = 1$ such that the energy is expressed in the units of E_J . The control Hamiltonian is $\sigma_1^z \sigma_2^z$, and the corresponding control pulse is $E_{cc}(t)$, which is expressed as a truncated Fourier series (Eq. (3.3)) parametrised by the set of parameters $\vec{\alpha}$ in CRAB and TCRAB.

We perform CRAB and TCRAB for the state-to-state transfer problem with the hyper-parameters specified in Sec. B.4.2 with 8 frequencies for the basis functions,

i.e. $M = 8$. We will assume depolarising noise here with a decay rate $\lambda = 0.01$, which means the fidelity calculation will follow Eq. (3.12).

In Fig. 3.1a, we have plotted $1 - F_{\text{opt}}(T)$ (see Eq. (3.13)), which is the optimal infidelity achieved by CRAB for different evolution time. Indeed, as expected, $1 - F_{\text{opt}}(T)$ decreases rapidly at the beginning due to the quantum speed limit, reaches an optimal point and then rises again due to noise in the evolution. Because of the discretisation of the time step, we are not able to read off the exact optimal time from this curve. We then perform TCRAB using the basin-hopping algorithm using 100 different initial guesses of the evolution time, evenly distributed across the whole time range. The lowest infidelity achieved is 0.0102 at the evolution time $T_{\text{opt}} = 1.35$. In 72 out of the 100 runs, our algorithm can converge around this optimal point, outputting $T_{\text{opt}} \in [1.349, 1.359]$. We have only shown the optimal points in the plot, but more results for the rest of the runs can be found in Sec. B.5.

We also perform the bisection method to search for the optimal time, with the gradient of F_{opt} estimated using finite difference. We are able to also obtain the same optimal evolution time $T_{\text{opt}} = 1.35$ using 48 evaluations of F_{opt} at different T during the algorithm.

Lipkin-Meshkov-Glick Model

The second example that we will look at is the Lipkin-Meshkov-Glick (LMG) model, which describes the uniform spin-spin interaction in the presence of a transverse magnetic field in z-direction:

$$H = -\frac{J}{N} \sum_{i < j} \sigma_i^x \sigma_j^x + \gamma \sigma_i^y \sigma_j^y - \Gamma(t) \sum_{i=1}^N \sigma_i^z. \quad (3.15)$$

Here J is the coupling strength of the spin-spin interactions, N is the number of spins, and γ governs the anisotropy of the spin-spin interaction. We are assuming that we can control the strength of the magnetic field, i.e. $\Gamma(t)$ is our control pulse. In the thermodynamic limit, $N \rightarrow \infty$, a second-order phase transition occurs at $\Gamma_c = 1$ from a ferromagnet($\Gamma < 1$) to a paramagnet($\Gamma > 1$). Here, looking at $N = 3$, we will perform a state-to-state transfer from the ground state

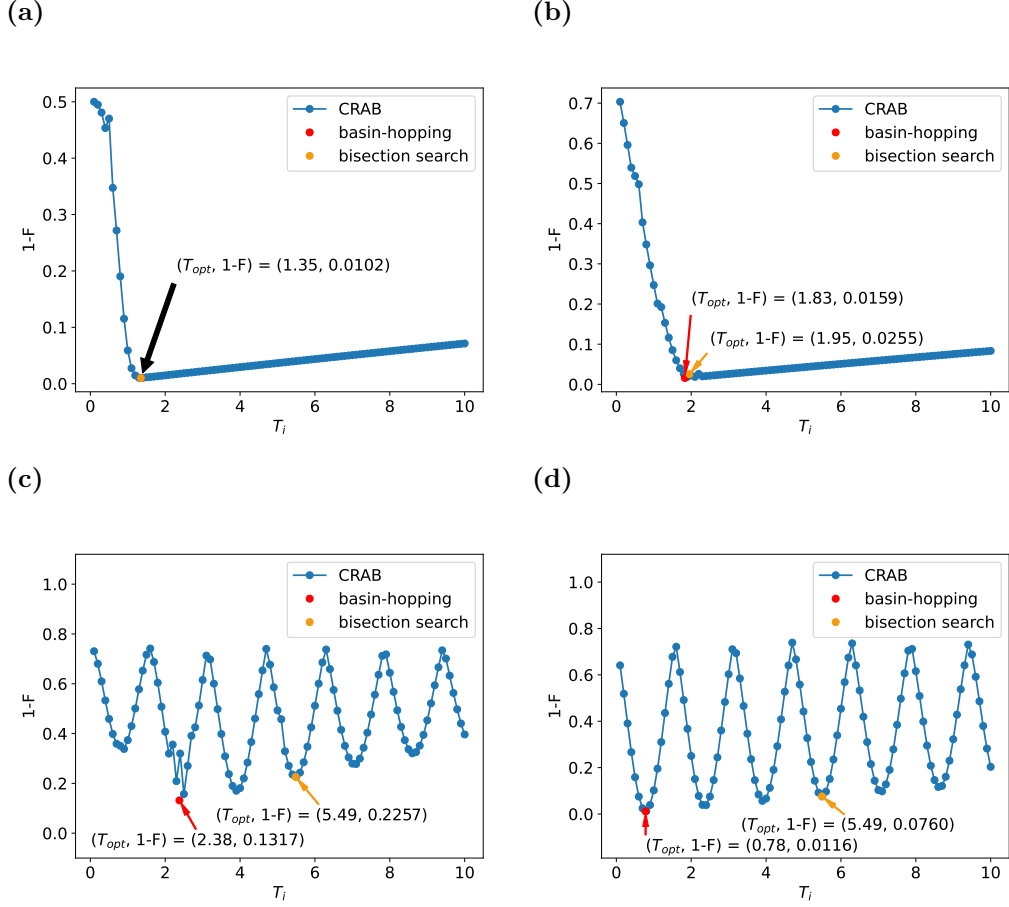


Figure 3.1: The optimised infidelity reached using CRAB (blue) and TCRAB with two optimisation methods, i.e. basin-hopping (red) and bisection search (orange) for (a) entanglement generation of two capacitively coupled Josephson charge qubits; (b) state-to-state transfer from the ground state of paramagnetic phase to a ground state of ferromagnetic phase; (c) CZ gate compilation for spin qubits with SWAP control fields; (d) CZ gate compilation for spin qubits with dipole-dipole control fields. The optimal time, T_{opt} , and optimised infidelity are annotated. In (a), we have basin-hopping and the bisection method both successfully converged to the same global minimum since the cost function is convex. In (b), (c) and (d), due to the presence of oscillations, the bisection search converged to a local minimum instead. Note that there is a small oscillation in the cost function near $T_i = 2$ for (b).

of the paramagnet ($\Gamma \gg 1$) to the ground state of the ferromagnet ($\Gamma = 0$). While there is only one ground state at the paramagnetic phase, i.e. all spins pointing in the $-z$ -direction, the system has degenerate ground states at the ferromagnetic phase. Given the form of the Hamiltonian and control fields, we chose $\frac{1}{2}(|000\rangle + |011\rangle + |101\rangle + |110\rangle)$ as the target state.

We perform the benchmark of CRAB and TCRAB with the hyper-parameters specified in Sec. B.4.2 with 10 frequencies for the control pulse basis functions, i.e. $M = 10$. We will again assume the noise here is depolarising noise with a decay rate $\lambda = 0.01$, which means the fidelity calculation follows Eq. (3.12).

The results are shown in Fig. 3.1b. Similar to the last example of entanglement generation, the optimised infidelity of CRAB decreases sharply until the minimum point, and then increases again due to decoherence. Similar to before, we perform TCRAB with basin-hopping using 100 different initial guesses of the evolution time. The lowest infidelity achieved is $1 - F_{opt} = 0.0160$ with the corresponding evolution time being $T_{opt} = 1.83$. In 72 out of the 100 runs, our algorithm can converge around this optimal point, outputting $T_{opt} \in [1.819, 1.859]$ (see Sec. B.5).

Using the bisection method instead, we obtain the optimal evolution time $T_{opt} = 1.95$ with the infidelity 0.0255 using 34 evaluations of F_{opt} . We are not able to reach the exact minimum in this case due to the small oscillation of $1 - F_{opt}(T)$ around the optimal evolution time as can be seen in Fig. 3.1b.

3.3.2 Gate Compilation

In this section, we will perform gate compilation for CZ gates between two spin qubits in quantum dots. In the lab frame, the general expression of Hamiltonian for two spin-1/2 particles in a uniform magnetic field is:

$$H = \frac{1}{2}(E_1 Z_1 + E_2 Z_2) + \frac{J}{2}\text{SWAP}, \quad (3.16)$$

where E_1 and E_2 are Zeeman splitting of the two spin qubits, respectively. It can be rearranged into

$$H = \frac{E_Z}{2}(Z_1 + Z_2) + \frac{\Omega}{2}(Z_1 - Z_2) + \frac{J}{2}\text{SWAP}, \quad (3.17)$$

where E_Z is the average Zeeman splitting $E_Z = (E_1 + E_2)/2$, and Ω is half of the difference between the Zeeman splitting of the two dots, i.e. $\Omega = (E_1 - E_2)/2$. Since the exchange interaction between two qubits can be controlled electrically by changing the plunger gate voltage, $J(t)$ will be tuneable and the related terms become our control Hamiltonian.

The main noise source in spin qubits in quantum dots is the charge noise in the various control lines [91], which can lead to fluctuation in $J(t)$ and/or $E_{1/2}$. These will be the sources of noise that we will consider later.

To perform the gate-compilation optimisation, we will map it into a state-to-state transfer problem using the Choi-Jamiołkowski isomorphism as further outlined in Sec. B.3. In this way, we could utilise tools we developed for the state-to-state problem in Sec. 3.2 to perform gate compilations in the presence of noise.

Depending on the natural set-up of the quantum dots, which can bring about different Ω , we will be interested in two different parameter regimes: $\Omega \ll J$ and $\Omega \gg J$ as will be discussed in the following sections.

CZ compilation at $\Omega \ll J$

In the regime of $\Omega \ll J$, i.e. the Zeeman splitting gradient is much smaller than the exchange interaction, the effective Hamiltonian in the rotating frame of reference is reduced to [92]:

$$H = \frac{1}{2}(\Delta E_1 Z_1 + \Delta E_2 Z_2) + \frac{J(t)}{2}\text{SWAP}. \quad (3.18)$$

Here ΔE_1 and ΔE_2 are additional Zeeman splitting on top of E_1 and E_2 , for example, due to micromagnets or local Stark shifts. We will assume these additional splittings to be fixed in our gate compilation. Hence, the drift Hamiltonian will lead to local Z rotations, and the control Hamiltonian is the SWAP operation.

Fluctuation in the gate voltages on the quantum dot can lead to fluctuation of ΔE_1 and ΔE_2 , which effectively becomes local dephasing channels on each qubit. Such noise channel commutes with the Hamiltonian in Eq. (3.18), thus the final fidelity between the final and the target state can be derived using the simulation method in Sec. 3.2.2 (See Sec. B.2.3 for more details).

We will perform the gate compilation of the CZ gate using CRAB and TCRAB. The Zeeman splittings in the drift Hamiltonian were set asymmetrically: $\Delta E_1 = 1.5$, $\Delta E_2 = 0.5$. The number of basis functions was set to $M = 8$, and other hyperparameters were chosen as stated in Sec. B.4.2. The local dephasing rate is set to be 0.05 (this is the strength of the related jump operator with its definition given in Sec. B.2.3).

The result is shown in Fig. 3.1c, we see that a key difference from our previous examples is the oscillation in the infidelity. This is because the drift Hamiltonian and control Hamiltonian commute in this case. Thus, the evolution operator of the drift field, i.e. e^{-iH_0T} leads to rotation on the multi-qubit Bloch sphere, causing oscillation in the fidelity. We will discuss such oscillations in further detail in Sec. 3.4.

On top of oscillation, the effects due to the quantum speed limit and decoherence from the noise channel lead to an envelope resembling what we have before. In order to determine the exact optimal time, we perform TCRAB using basin-hopping and found $T_{opt} = 2.38$ to be the optimal time of evolution, which results in the lowest infidelity of 0.1317. As further detailed in Sec. B.5, for the 100 rounds of basin-hopping optimisation we perform, 13 of them end in the right basin and give us the optimal time. Within these 13 runs, 10 of them start far away from the optimal time, showing that our algorithm is not susceptible to local traps. For the rest of the runs, the majority of them end in the second and third most optimal time.

Using the bisection method instead, we can obtain the optimal evolution time $T_{opt} = 5.49$ with the infidelity 0.2257 using 34 evaluations of F_{opt} . We have reached the third lowest basin with still very low infidelity.

CZ compilation at $\Omega \gg J$

In the regime of $\Omega \gg J$, i.e. the Zeeman splitting gradient is much larger than the exchange interaction, the effective Hamiltonian in the rotating frame of reference is reduced to:

$$H = \frac{1}{2}(\Delta E_1 Z_1 + \Delta E_2 Z_2) + \frac{J(t)}{2} Z_1 \otimes Z_2. \quad (3.19)$$

In this regime, the control Hamiltonian becomes the dipole-dipole interaction, i.e. the $Z \otimes Z$ term, while the drift Hamiltonian is the sum of two single Z gates, i.e. $H_0 = \frac{1}{2}(\Delta E_1 Z_1 + \Delta E_2 Z_2)$, as in Eq. (3.19).

Here let us investigate another possible noise source coming from the oscillation of $J(t)$, which will lead to the dipole-dipole noise channels (See Sec. B.2.6 for more details.). Again such noise channel commutes with the Hamiltonian in Eq. (3.19), thus the final fidelity between the final and the target state can be derived using the simulation method in Sec. 3.2.2.

Fig. B.6 shows the results of the gate compilation of the CZ gate using CRAB and TCRAB. We chose to use 8 frequencies, i.e. $M = 8$, to define the control pulse. The Zeeman splittings for the two quantum dots were set symmetrically: $\Delta E_1 = 1.0$, $\Delta E_2 = 1.0$. The decay rate of the dipole-dipole noise channel was set as 0.03 (See Sec. B.2.6).

Again, we see oscillation in the optimised infidelity for the same reason and there is again an envelope due to fidelity decay caused by noise. After 100 runs of TCRAB using basin-hopping, we identified $T_{opt} = 0.78$ to be the optimal time of evolution, which resulted in the lowest infidelity of 0.0116. Out of the 100 TCRAB runs, 86 converges to around the global optimal time. For the rest of the runs, 13 of them converge to the second lowest basin and one run converges to the third lowest basin. Using the bisection method instead, we can obtain the optimal evolution time $T_{opt} = 5.49$ with the infidelity 0.0760 using 34 evaluations of F_{opt} , which in the fourth lowest basin with still very low infidelity.

3.4 Discussion

After seeing how time optimisation works in our examples. Let us recap how the optimised fidelity $F_{opt}(T)$ varies with the evolution time T and further discuss three reasons why the time optimisation is essential: 1) the presence of noise; 2) the oscillation of infidelity due to the drift Hamiltonian and 3) the ability to escape local traps in the other optimisation direction.

1. At T smaller than the minimal required time set by the quantum speed limit, we will expect the optimised fidelity $F_{\text{opt}}(T)$ to increase as we increase T since we have not yet had sufficient time to evolve to the target state at this point, due to the energy scale and constraints we place on our control Hamiltonian. At large T , the length of the evolution time is no longer the rate-limiting factor, and decay in $F_{\text{opt}}(T)$ due to noise will dominate. Both of these effects can be seen in our experiments in Figs. 3.1a and 3.1b, and time optimisation is essential for identifying the optimal trade-off point between them.

2. If the control field cannot compensate for the effect of the drift field by some appropriate control pulses, then the control field will have limited influence on the trajectory in the state space that purely due to the drift field, which is some rotation along a hyper-surface. Such a rotation will periodically approach the target state, then move away and repeat, leading to oscillations in the optimised fidelity $F_{\text{opt}}(T)$. Whether such oscillatory behaviour exists or not is not affected by the presence of noise, thus one can check whether $F_{\text{opt}}(T)$ is oscillatory or not by simply performing the noiseless optimisation. We also can see that such an oscillation indeed comes from the fact that the control field cannot compensate for the effect of the drift field through the numerical experiment in Sec. B.7, in which we test whether the effective identity channel is achievable at different evolution times. In the presence of such oscillation, the optimised fidelity varies so significantly with time that time optimisation becomes essential. In some specific cases, we might be able to guess the position of the fidelity peak, but this cannot be done in general, especially in the presence of decoherence. We have discussed a more explicit derivation of this oscillation behaviour in Sec. B.6. This is for the case when the drift Hamiltonian commutes with the control Hamiltonian and the basis for the drift Hamiltonian is not part of the basis for the control Hamiltonian, which is what happens in Figs. 3.1c and 3.1d.

3. Variation in time can also help with escaping local traps in the pulse optimisation. When performing standard CRAB without T optimisation, we are susceptible to local traps in the pulse optimisation in two main ways. When the

number of basis functions M is small, such local traps are due to the limited expressivity of the control pulse. When the number of basis function M is big, such local traps are due to the difficulties in optimising $\vec{\alpha}$ due to the increased dimensionality. Both of these effects are shown in Fig. 3.2. There we see that we often can move away from local traps and reach lower infidelity by moving to another nearby T . Hence, by adding the evolution time as an additional parameter in the search space, the optimisation is more likely to navigate out of these false traps by moving along the new time direction. This is also seen in Fig. 3.1c. There, the cost function landscape obtained by CRAB is ragged near the second trough due to its inability to escape local traps. In contrast, basin-hopping is able to escape these local traps, reaching a lower infidelity than CRAB even at the same evolution time and giving us the true global optimum.

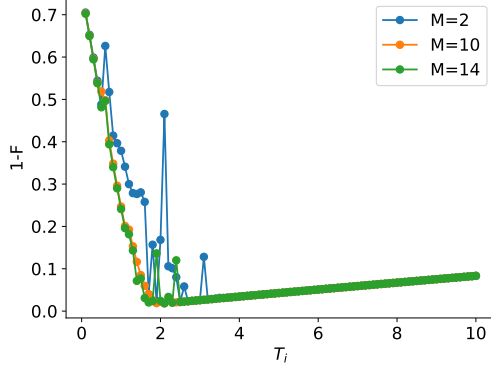


Figure 3.2: Optimised infidelity using basin-hopping for the state-to-state transfer problem of the LMG model (Sec. 3.3.1). M is the number of basis functions in the pulse. Local traps in optimisation have led to fluctuations in the optimised infidelity. Such fluctuation is more prominent when M is either too small (e.g. $M = 2$) or too large (e.g. $M = 14$).

3.5 Conclusion

In this paper, we analyse the condition required for the noise to commute with the gate Hamiltonian in the context of quantum optimal control, which allow us to study the effect of such noise and obtain an analytic expression of the resultant fidelity. Under such noise, for a given evolution time, we can now perform the

pulse optimisation using the CRAB protocol of the noisy system at a similar computation cost as the noiseless system, which is an exponential reduction in the computation cost in terms of the number of qubits. Leveraging this approach, we are able to perform optimisation of the evolution time on top of optimising the pulse parameters. We have performed numerical simulations on state-to-state transfer problems for Josephson charge qubits and LMG models and gate compilation problems for silicon spin qubits, under noise models such as global depolarising noise, local dephasing noise and dipole-dipole noise. In these examples, we indeed see a strong dependence of the optimised infidelity on the evolution time, caused by noise, drift field oscillations and local traps encountered in pulse optimisations. Our results indicate that an inappropriate choice of evolution time can significantly increase infidelity, highlighting the necessity to optimise the evolution time. Using the basin-hopping algorithm for optimisation, we are able to consistently identify globally optimal evolution times across all considered examples. In addition, we have explored the use of root-finding methods like bisection search, which can output a local optimum rather than a global one. However, these local optimum are nonetheless much better than an arbitrary choice of evolution time and is comparable to the global optimum in terms of infidelity in our examples.

Our paper just marks the start of the numerous possibilities for incorporating time optimisation into quantum optimal control. A natural extension is to expand time optimisation to dCRAB [93], and more generally other quantum optimal control algorithms like GRAPE and Krotov method, to see if similar efficient implementation can be found. It is also interesting to explore the effect of more general noise models, for example going beyond Pauli noise or considering noise that only approximately commutes with the gate Hamiltonian. We can even consider pulse optimisation that incorporates Pauli-twirling-like behaviour that can enhance the commutation between the noise and the gate Hamiltonian.

Another possible area to explore is the optimisation algorithm used. We have considered basin-hopping and the bisection method in this article, and one might wonder whether there are other optimisation algorithms that are more efficient

and/or more accurate. Methods like simulated annealing [94] and evolutionary methods [95] have found previous success in quantum optimal control [55, 96–101], and thus will be interesting to investigate their performance with time optimisation. This can be new optimisers that more explicitly consider the difference between the cost function landscapes along the T direction and the $\vec{\alpha}$ direction, or optimisers that can take advantage of the analytical expression of the fidelity expression that we derived.

Appendices

Cor animalium, fundamentum est vitæ, princeps omnium, Microcosmi Sol, a quo omnis vegetatio dependet, vigor omnis & robur emanat.

The heart of animals is the foundation of their life, the sovereign of everything within them, the sun of their microcosm, that upon which all growth depends, from which all power proceeds.

— William Harvey [harvey_exercitatio_1628]



Appendix of Robustness of electron charge shuttling: Architectures, pulses, charge defects and noise thresholds

Contents

A.1 Details of Conveyor-Belt Shuttling	64
A.1.1 Energy Evolution	64
A.1.2 Two Possible Phase Variations	64
A.1.3 The Effect of Finite Extent of the QD in the perpendicular direction	68
A.1.4 The Comparison of 1D and 2D Simulations for the Shuttling	70
A.2 Details of Numerical Simulations	70
A.2.1 Boundary Conditions	70
A.2.2 Numerical Methods	73
A.2.3 Definition of Model	74
A.2.4 Convergence Studies of the model	78
A.2.5 Numerical Precision	79
A.2.6 Lumped Element Model of a Voltage Source connected to Clavier Gates	80
A.2.7 Generation of Johnson-Nyquist Noise	81
A.3 Additional Results of the Conveyor-Belt Mode Shuttling	81
A.3.1 Noise-free Shuttling: Target Speed	81
A.3.2 Sensitivity to step-changes in voltage control	81
A.3.3 Sensitivity to Classical Johnson Nyquist Noise	86
A.3.4 Speed Vs. Adiabaticity	87
A.3.5 Sensitivity to Charge Defects: Two Defects of Varying Separations.	91
A.4 Results of Advanced Non-Adiabatic Ultra-fast shuttling	91

Appendices are just like chapters. Their sections and subsections get numbered and included in the table of contents; figures and equations and tables added up, etc. Lorem ipsum dolor sit amet, consectetur adipiscing elit. Sed et dui sem. Aliquam dictum et ante ut semper. Donec sollicitudin sed quam at aliquet. Sed maximus diam elementum justo auctor, eget volutpat elit eleifend. Curabitur hendrerit ligula in erat feugiat, at rutrum risus suscipit. Pellentesque habitant morbi tristique senectus et netus et malesuada fames ac turpis egestas. Integer risus nulla, facilisis eget lacinia a, pretium mattis metus. Vestibulum aliquam varius ligula nec consectetur. Maecenas ac ipsum odio. Cras ac elit consequat, eleifend ipsum sodales, euismod nunc. Nam vitae tempor enim, sit amet eleifend nisi. Etiam at erat vel neque consequat.

A.1 Details of Conveyor-Belt Shuttling

A.1.1 Energy Evolution

Figure A.1 shows the evolution of kinetic, potential, and total energy when the electron is shuttled over one unit cell length for 3 electrodes per unit cell. The energy curves are periodic with the period $L/(Nv)$, where L is the length of the unit cell, v is the shuttling speed, and N is the number of gates per cell: this is the time taken for the electron to travel from one gate to the next.

The change of local potential energy results from the change of local curvature as shown in Figure 2.3e. The curvature a maximum when the electron is directly underneath one of the gates and a minimum when the electron is beneath the gap between two gates.

A.1.2 Two Possible Phase Variations

As mentioned in 2.3, the trajectory and speed of shuttling depend on how we vary the phase $\phi(t)$ of the sinusoidal pulses in equation 2.3.

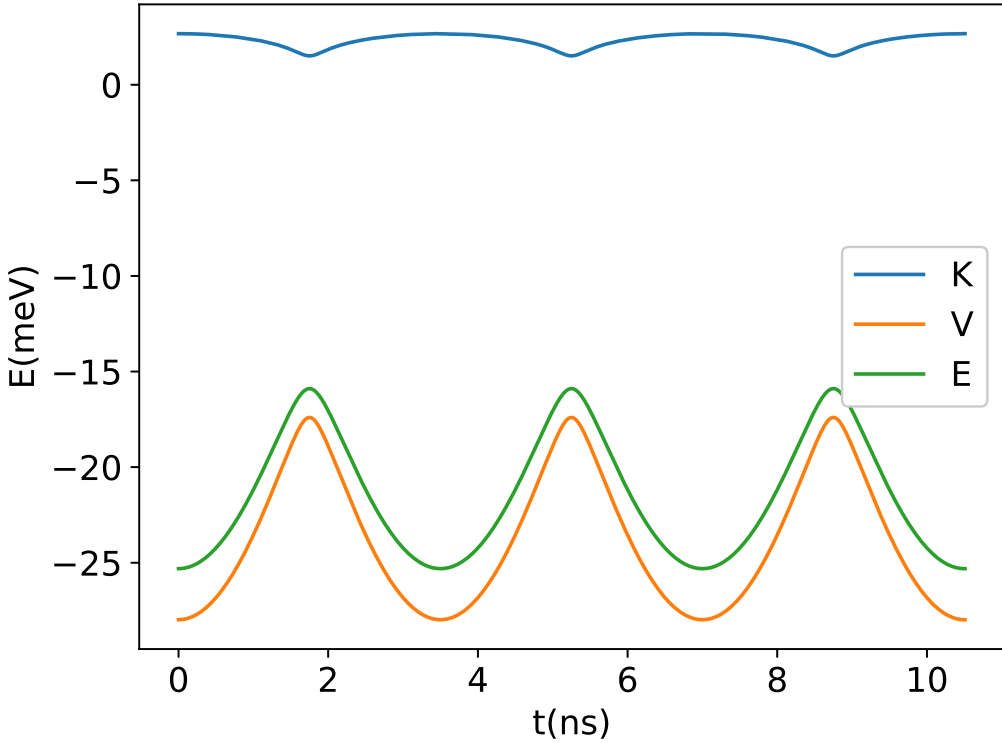


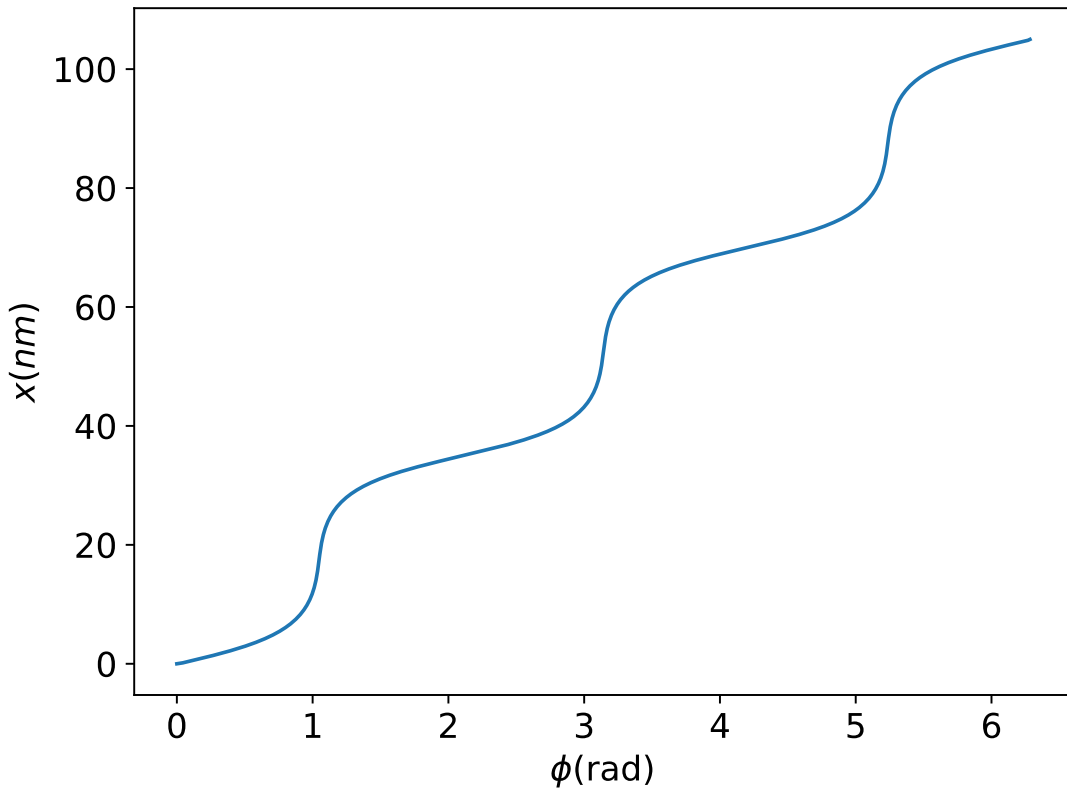
Figure A.1: For $N = 3$, the kinetic energy (blue), the potential energy (orange), and the total energy (green) of electron during conveyor-belt shuttling for a distance of one unit cell, i.e. 105 nm for $N = 3$. with linearly varying phase.

The simplest way is to update the phase linearly with time, i.e. $\phi(t) = k t$, where k is the rate of change of phase. The periods of the sinusoidal pulses in the time domain are then $2\pi/k$ and the average shuttling speed is $v_{avg} = k \frac{L}{2\pi}$, where L is the length of the unit cell.

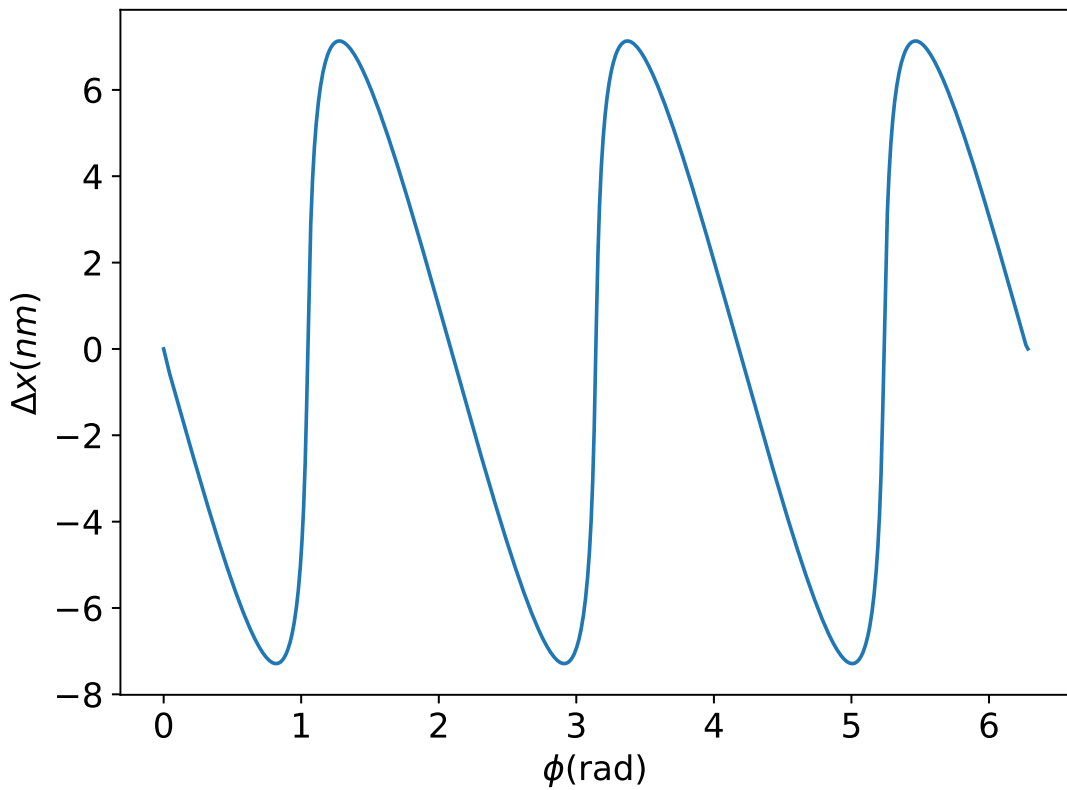
Nevertheless, the instantaneous speed is not constant, as the position of the minimum of the potential energy does not depend linearly on the phase but instead varies as shown in Figure A.2a, which can be further decomposed as a sum of a linear function and a periodic perturbation (with period $2\pi/N$ for N electrodes) in Figure A.2b.

We can use a non-linear phase function $\phi(t)$ to shuttle the electron along an arbitrary trajectory, $x(t)$. Suppose that f is a function mapping the phase to the position of the minimum of potential energy, i.e. $x = f(\phi)$ with its shape presented in Figure A.2a. For any position x , one can use the inverse function f^{-1} as a

(a)



(b)



(c)

DRAFT Printed on December 3, 2025

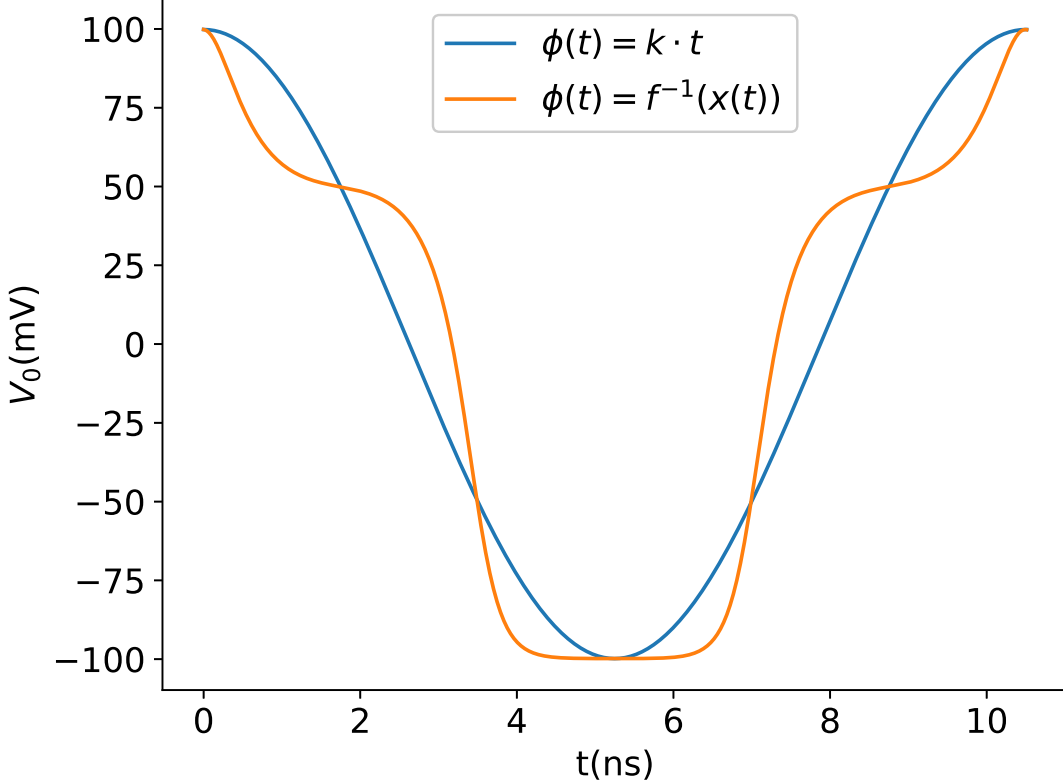


Figure A.3: An example of voltage signal on the 1st gate in the unit cell for different choices of phase variation $\phi(t)$, i.e. linearly increasing phase, and phase generated by the look-up table (orange line). This is the same as the inset of Figure 2.3c

look-up table to find the corresponding phase; thus, given an arbitrary trajectory $x(t)$ one can find the corresponding phase at each time step $\phi(t) = f^{-1}(x(t))$. Here, we implement this approach for shuttling with constant speed: $x(t) = vt$.

Figure A.3 shows the voltage signal at the first gate in the unit cell for the two phase variations $\phi(t)$: the blue line represents linear phase variation and the orange line represents shuttling at a strictly constant speed (with $v_{avg} = 10$ m/s in both cases). Signals can also be generated for more general $x(t)$, such as trajectories involving either constant or time-dependent accelerations.

For the noiseless shuttling up to the distance of $8.4\ \mu\text{m}$ ($A = 100$ mV, $v = 10$ m/s), both phase variation methods yielded loss probability below 1.5×10^{-11} and excitation fraction below 5×10^{-7} . Furthermore, we found no qualitative difference in these important metrics and no clear trend as to which profile gives better results. Since it is easier to generate sinusoidal pulses than more complicated

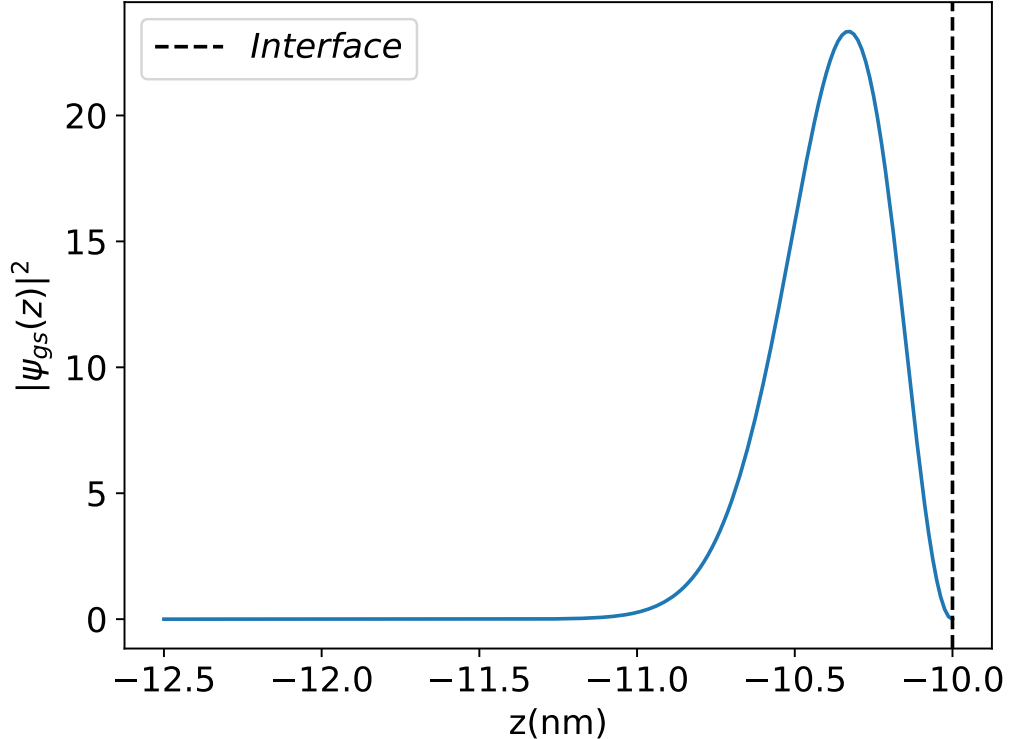


Figure A.4: Probability density of the ground state in the z-direction (blue line). Probability density exists only in $z < -10$ nm, where there is a silicon layer. The probability density tails off at -11 nm, which makes the confinement length 1 nm below the interface (dotted line).

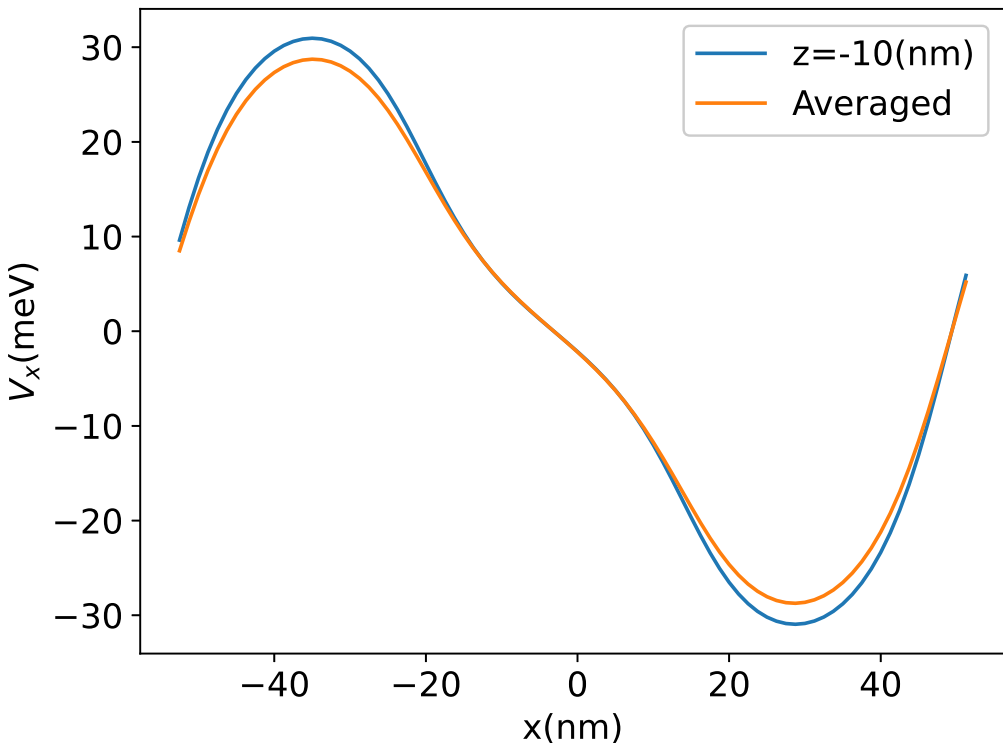
pulses with several frequency components, we chose the linearly varying phase as the default for the rest of the paper.

A.1.3 The Effect of Finite Extent of the QD in the perpendicular direction

Our shuttling model is perfectly two-dimensional and therefore ignores the finite extent of the quantum dots in the direction perpendicular to the interface. In this section we explore the averaging of the electrostatic potential as a result of this finite thickness.

Figure A.5 shows the spatial variation of two potentials, both along the channel and across it. One potential is sampled directly at the Si/SiO₂ interface and the other is obtained by averaging over the probability density of the ground state in

(a)



(b)

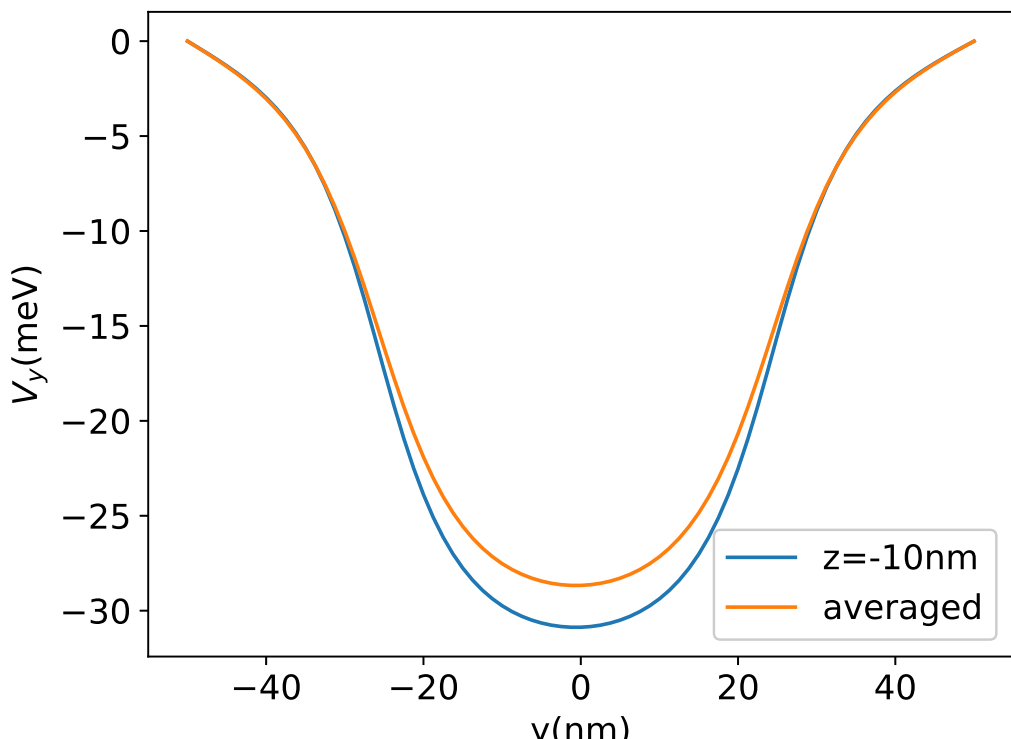


Figure A.5: Cross-section of potentials on (a) the $y = 0$ nm and (b) $x = 27.5$ nm planes for the potential sampled at $z = -10$ nm (blue line) and the potential averaged over the probability density of the ground state in the z -direction for the thickness of 1 nm (orange line).

the z-direction, assuming that the confinement length of the QD is 1 nm, using an Airy function of the first kind, truncated up to the last x-intercept, as the ground state as shown in Figure A.4.

Note that the difference between the depths of the potential is about 7% of the well depth of potential, and the effect of the averaging is similar to a rescaling of the gate voltages at the gates. Given these relatively small differences, we use the potential sampled directly at the interface in the remainder of the paper.

A.1.4 The Comparison of 1D and 2D Simulations for the Shuttling

We found both the loss probability and the excitation fraction has an order of magnitude difference. For the noiseless shuttling for a distance of $1.4\mu\text{m}$ ($A = 100\text{ mV}$, $v = 10\text{ m/s}$), the loss probability in the case of Note that the energy gap of the 1D potential (6.38 meV), is smaller than the energy gap of the 2D potential (3.837 meV). This is because the first excited state of the 2D potential is in the y-direction as shown in Figure A.6.

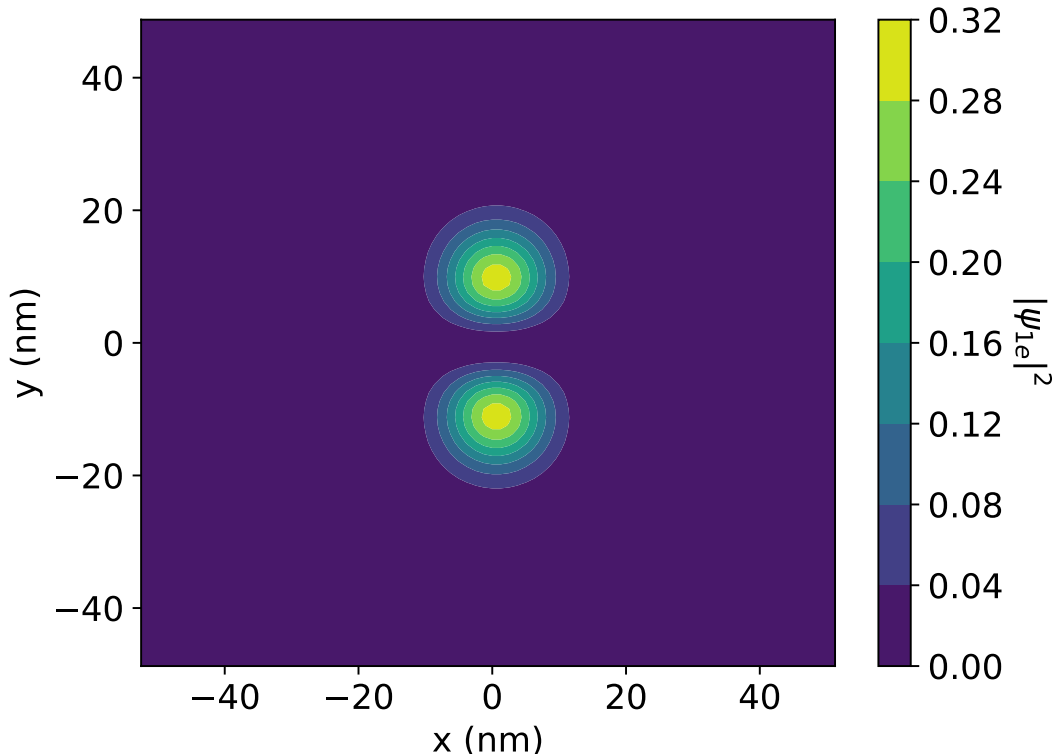
A.2 Details of Numerical Simulations

A.2.1 Boundary Conditions

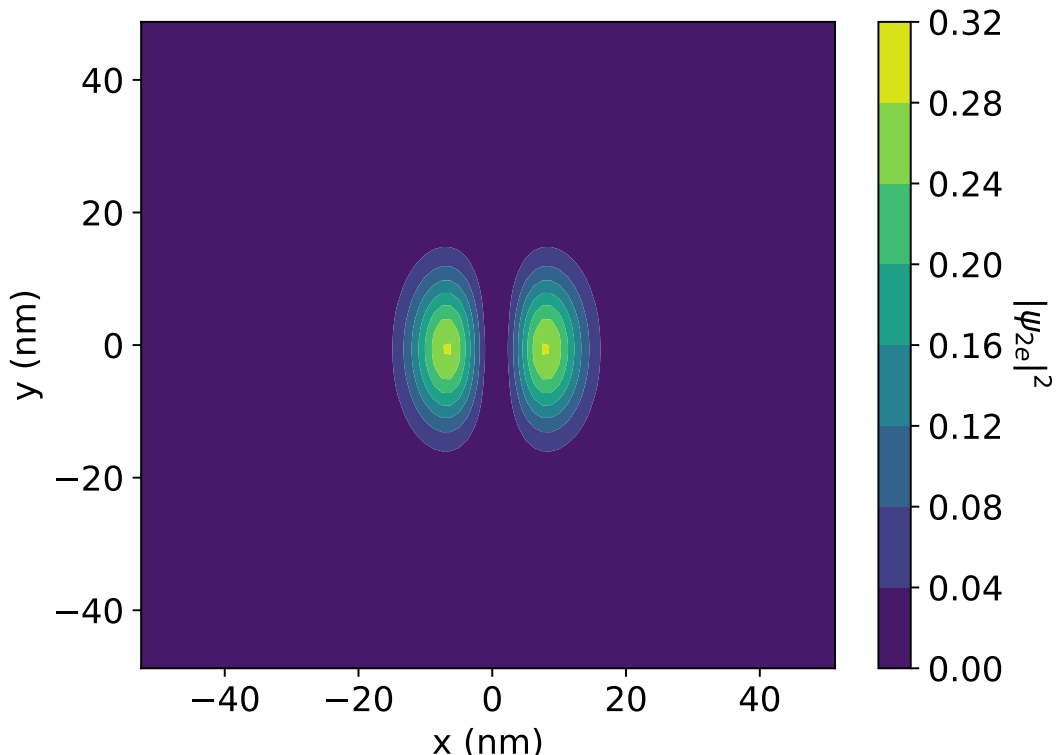
In this section, we outline the boundary conditions to solve the Laplace and time-dependent Schrödinger equations, explain the numerical methods and techniques for both cases, and, finally, state the set of hyper-parameters in the simulations, which we define as the *model*.

As noted in section 2.2 and section 2.3, we make two assumptions that allow us to use periodic boundary condition in the shuttling direction (the $+x$ direction): (1) there is an infinite line of clavier gates along the axis and (2) there are N independent voltage signals applied to the gates. These allow us to limit our domain to solve the Laplace equation to one unit cell of the device. Thus, the boundary conditions of the system are as follows:

(a)



(b)



(c)

Periodic Boundary Conditions

Since the unit cell repeats along the x axis, we used periodic boundary condition along this axis, i.e. $\Phi(x, y, z) = \Phi(x + d, y, z)$, where d is the length of the unit cell in the x-axis.

Dirichlet Boundary Conditions

On the $y = \pm 50$ nm planes, Dirichlet boundary conditions were imposed such that $\Phi(x, y = \pm 50 \text{ nm}, z) = 0$ for the Laplace solver. These boundary conditions are reasonable because the potential energy barrier from the confinement gates is an order of magnitude greater than the characteristic energy gap in the y -direction, which is the energy gap between the ground and first excited states (see Figure A.6a), so the precise form of the top of the barrier is not critical: specifically, for our default setting of $A = 100$ mV at the gates, the height of the potential energy is 8.5 times bigger than the characteristic energy gap. When the gate voltage amplitude is smaller, the height of the potential barrier becomes only twice as big as the characteristic energy gap for $A = 6.24$ mV. However, such small amplitudes were only used for the simulation of noiseless shuttling cases in section 2.6. In these cases, the excitation fraction, defined in section 2.5, is as low as approximately 5×10^{-3} in the worst-case scenario (see section 2.6 for more details). In addition, hard-wall boundary conditions were imposed in the time-dependent Schrödinger solver, i.e. the wave function is always zero on $y = \pm 50$ nm planes, so that there is no loss of probability outside the well in the y -direction.

For the bottom surface of the device, i.e. $z = -60$ nm, Dirichlet boundary condition was imposed such that $\Phi(x, y, z = -60 \text{ nm}) = 0$. The position of the bottom surface doesn't change the overall physics: We found that the depth of potential energy changed about 1-2% when the bottom surface of the device was 540 nm below the gates instead of 60 nm. Moreover, the electrode regions, represented as yellow boxes in Figure 2.2, have Dirichlet conditions applied at their boundaries fixing the potential at the voltages applied to individual gates.

Neumann Boundary Conditions

In Figure 2.2b, at $z = 15$ nm, in the gaps between the electrodes, Neumann boundary conditions were imposed such that $\frac{\partial \Phi}{\partial z} = 0$. This is to reflect that the electric fields between two clavier gates should be parallel to the X-Y plane. At the interface between the Si and SiO_2 , i.e. $z = -10$ nm, the displacement field should be continuous, and, thus, a Neumann boundary condition was imposed such that $\epsilon_{\text{ox}} \frac{\partial \Phi_{\text{ox}}}{\partial z} = \epsilon_{\text{Si}} \frac{\partial \Phi_{\text{Si}}}{\partial z}$.

A.2.2 Numerical Methods

The numerical methods consist of two parts: a Laplace solver to obtain a time-dependent potential from the gates and a Schrödinger solver to simulate the dynamics of the electron state in the shuttling device.

We used successive over-relaxation (SOR)[3, 4] to obtain the time-dependent potential in the unit cell in Figure 2.2. Instead of solving the Laplace equation to obtain the potential at every time step, we used the fact that any potential can be expressed as a linear combination of individual contributions from the gates[102]:

$$\Phi(x, y, z, t) = \sum_{i=1}^N u_i(t) \phi_i(x, y, z), \quad (\text{A.1})$$

where N is the number of gates in the unit cell, and $\{\phi_i\}_{i=1..N}$ are the solutions to the Laplace equation when only one of the gates in the unit cell is turned on and the potentials on the others are zero. $u_i(t)$ is the voltage applied to the i th gate as a function of time. Moreover, the periodic boundary condition along the x -axis means the solutions ϕ_i for different electrodes can be generated from one another by simple translations. Figure 2.4 shows two examples of the potential energy obtained by the Laplace solver, at the points of maximum and minimum curvature $\kappa(\phi)$ near the potential minimum.

We used the split operator method[5] with symmetric Strang splitting[6, 7] to solve the time-dependent Schrödinger equation. By using the fact that kinetic

energy operator is diagonal in k-space and the potential operator is diagonal in position space, the state of an electron was propagated as follows:

$$\begin{aligned}\hat{U}_r(\Delta t) &= e^{\frac{i}{\hbar}e\Phi(\vec{r},t)\Delta t} \\ \hat{U}_k(\Delta t) &= e^{-\frac{i\hbar k^2 \Delta t}{2m}} \\ \psi(\vec{r}, t + \Delta t) &= \hat{U}_r\left(\frac{\Delta t}{2}\right) F^{-1}[\hat{U}_k(\Delta t) F[\hat{U}_r\left(\frac{\Delta t}{2}\right) \psi(\vec{r}, t)]],\end{aligned}\quad (\text{A.2})$$

where F and F^{-1} are Fourier and inverse Fourier transform to move from position space to the k-space, and $\hat{U}_r(\Delta t)$ and $\hat{U}_k(\Delta t)$ are propagators in position space and k-space, respectively.

Since we imposed hard-wall boundary condition on ψ at the planes $y = \pm 50$ nm to mimic the effect of the confinement gates, we used a discrete sine transform (DST) to perform the Fourier transform in the y -direction. The DST allows us to impose the boundary condition, i.e. $\psi(x, y = \pm 50 \text{ nm}, t) = 0$, at the boundaries.

A.2.3 Definition of Model

The model is defined as a set of hyper-parameters with which the full simulation can be reproduced. These include: (1) the choice of the unit system to map the simulation results to real systems; (2) parameters used in the numerical algorithms to simulate the dynamics, such as the step sizes of the grid; (3) device-specific parameters, such as the dimensions of the gates and permittivity of the device materials; (4) parameters to specify the shuttling scenarios, such as the distance, speed, acceleration of the electron as a function time.

In the Schrödinger solver, we set the reduced Planck constant, electric charge constant, and the mass of the free electron to one, i.e. $\hbar = e = m_{e,0} = 1$. With the remaining degree of freedom, we chose our length unit to be 10 nm. From the constraint $\hbar = 1$, the time unit and energy unit are uniquely determined to be 0.8637 ps and 0.762 meV. Below are the equations to derive the time unit and energy units:

$$1(\text{time unit}) = \frac{m_e \times 1(\text{length unit})^2}{\hbar} = 0.8637 \text{ ps}$$

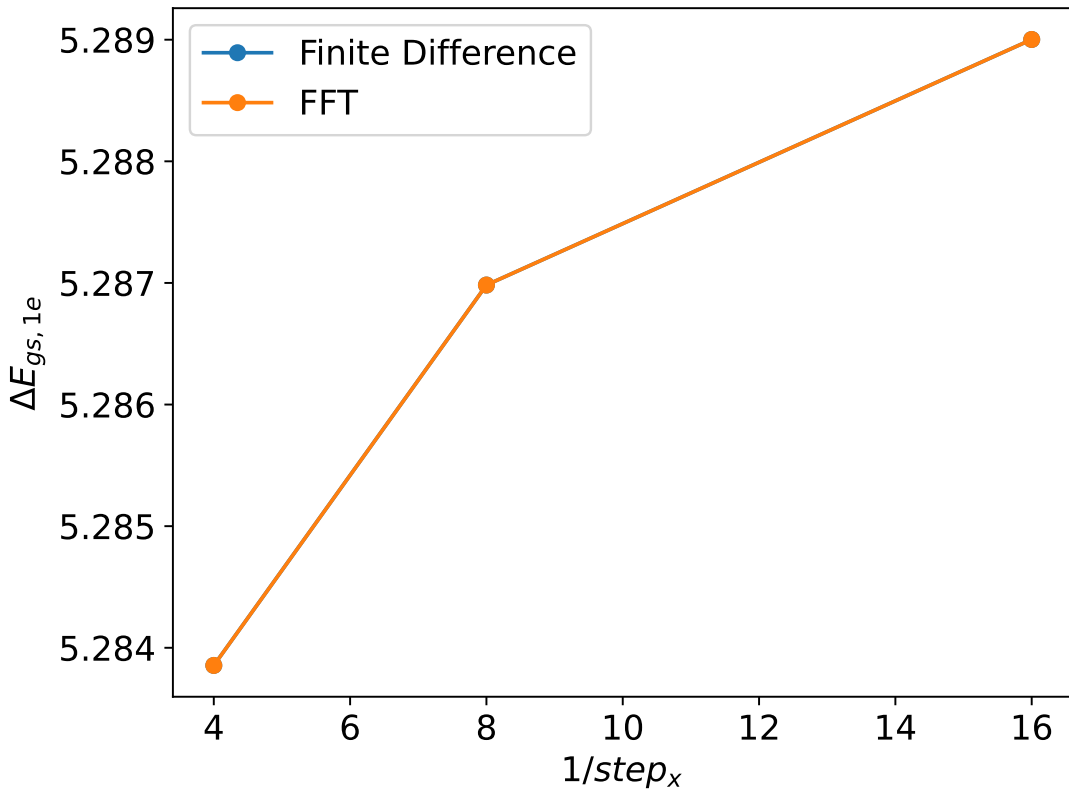
$$1(\text{energy unit}) = \frac{\hbar}{1(\text{time unit})} = 0.762 \text{ meV}. \quad (\text{A.3})$$

The spatial grid spacing used in the Laplace solver and Schrödinger solver were 0.125 for both x and y directions while the time step was 0.003125. The convergence of the solvers was tested as described in Appendix A.2.4. The relaxation parameter of the SOR in Laplace solver, ω , was 1.9, which controls the rate of convergence. The dimensions of the gates are outlined in section 2.2 while 3.9 and 11.69 were taken as permittivity of Si and SiO₂, respectively. Furthermore, the transverse electron mass in Si, $m_{e,t}^* = 0.19m_{e,0}$, was used for the motion in the 2D plane of the device (corresponding to population of the $\pm z$ valleys).

The default target distance and speed were set to 1.4 μm and 10 m/s. These choices were made because the length of one unit cell in the x -direction is an integer multiple of 35 nm, and the optimal speed of shuttling suggested by previous analytical calculations is around 10 m/s[1].

All our models approximate reality by the discretization of space and time; remaining sources of significant error are the Trotterization error of the split operator method[5] in the Schrödinger solver, and the error below the tolerance threshold of SOR in the Laplace solver. As we reduce the step sizes in our model, it becomes a better representation of reality but the computational cost grows by $\mathcal{O}(N_p N_{iter})$ [103] for the SOR and $\mathcal{O}(N_p \log N_p)$ for the split operator method, where N_p is the number of spatial grid points, and N_{iter} is the number of SOR loops, which grows with increasing N_p . For both SOR and split operator method, the complexity grows only linearly with the number of grid points in time, i.e. $\mathcal{O}(N_t)$. For the specific choices made in our model, the numerical artefacts are explained in more detail in Appendix A.2.5.

(a)



(b)

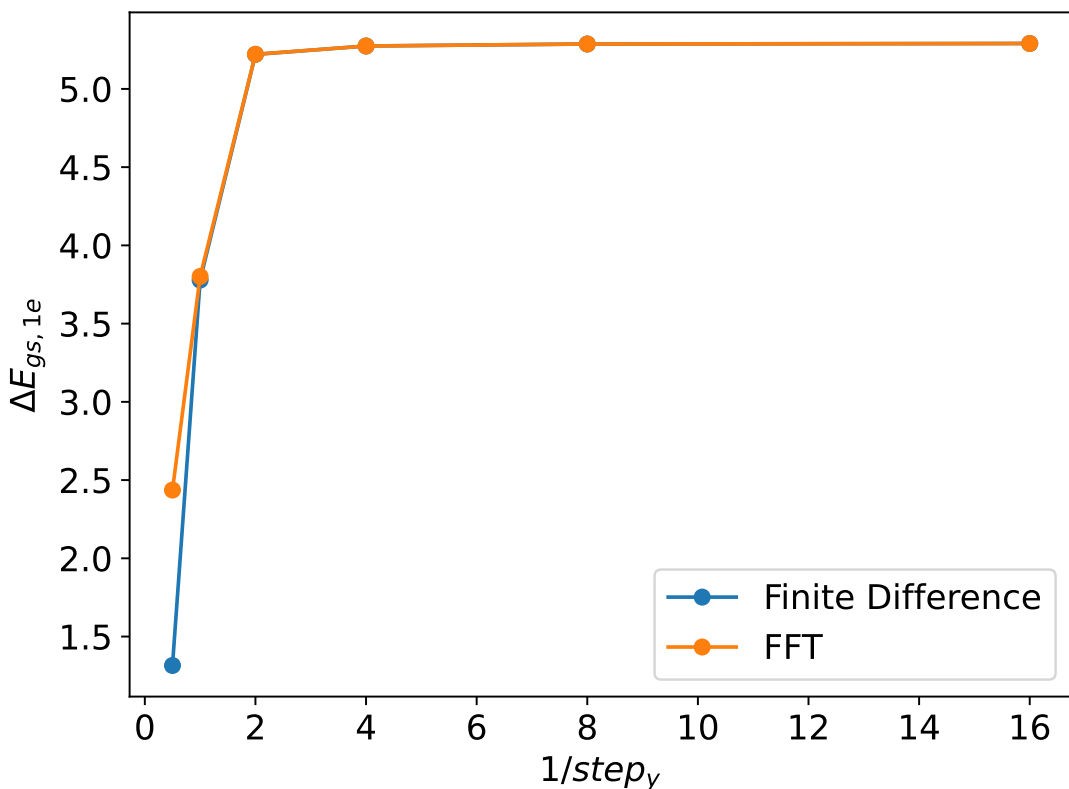
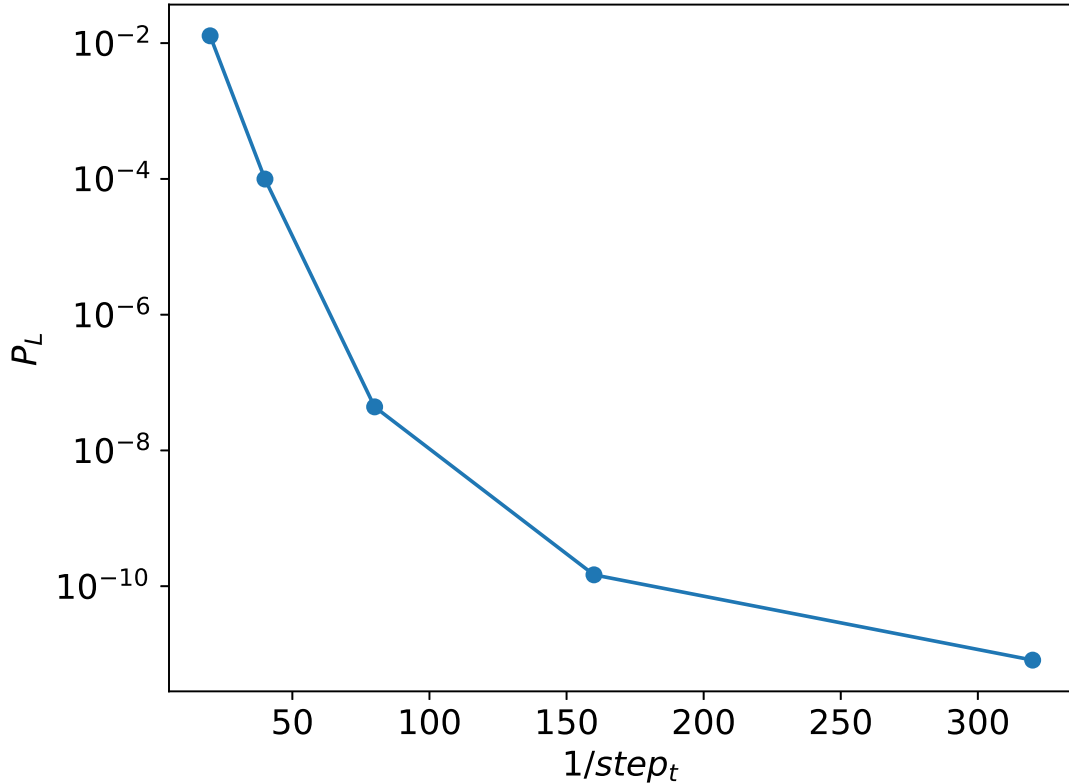


Figure A.7: Convergence studies for the spatial resolution: The energy gap of the initial Hamiltonian obtained with different step sizes in (a) x and (b) y direction for $N = 5$.

(a)



(b)

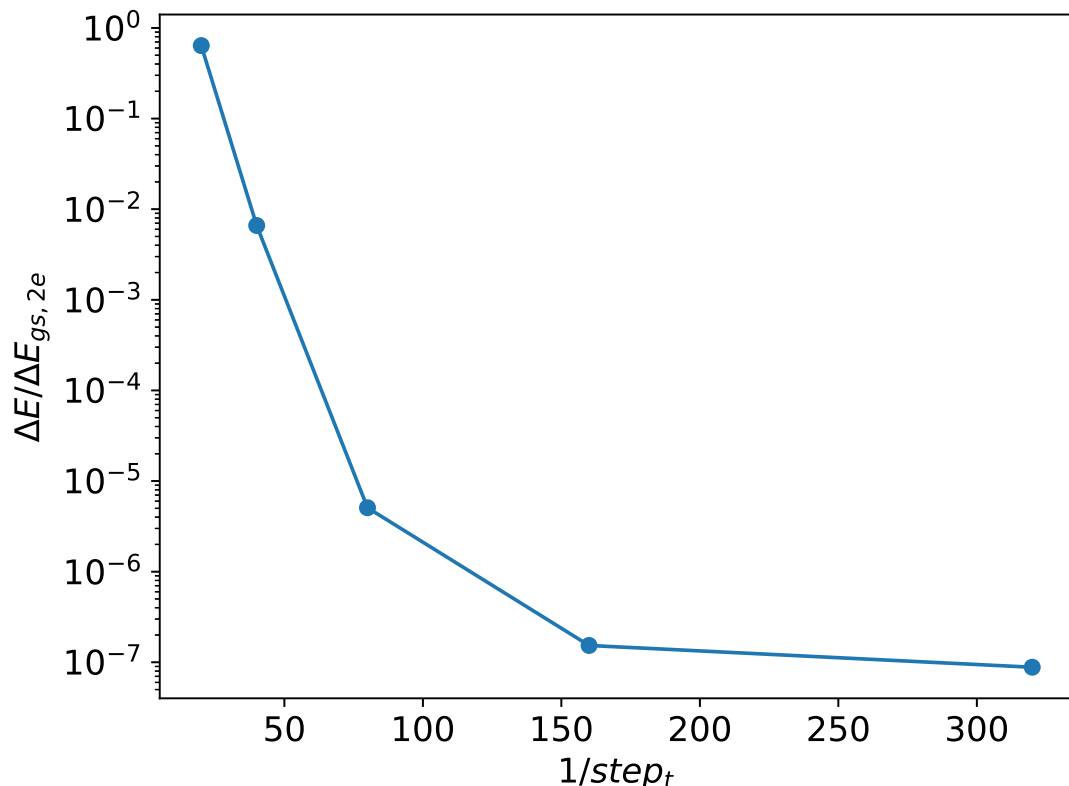


Figure A.8: Convergence studies for the temporal resolution. For $N = 4$, (a) the loss probability and (b) excitation fraction obtained after the shuttling of $2.1\ \mu\text{m}$.

A.2.4 Convergence Studies of the model

The model consists of the Laplace solver to obtain the time-dependent potential in the device and the time-dependent Schrödinger solver to obtain the evolution of the state forward in time.

For this numerical model, appropriate spatial and temporal step sizes had to be chosen. The metric used to determine the convergence for the spatial resolution was the energy gap between the ground state and the first excited state for the initial Hamiltonian ($t=0$). The energy gap was first obtained by diagonalizing the Hamiltonian matrix, whose size is determined by the step sizes in x and y directions. These points were plotted in Figure A.7 with blue dots. Secondly, using the normalized initial and first excited states obtained by the diagonalization, the energy gap was once again obtained by evaluating the expectation values of the initial Hamiltonian. These points were plotted with orange dots in Figure A.7.

By fixing the step y to be 0.125, the convergence tests of step x were performed, whose results are shown in Figure A.7a. When step x changes from 0.125 (second point) to 0.0625 (last point), energy gap changes by 0.038 %. Thus, 0.125 was chosen to be the step size in the x direction.

Similarly, the convergence tests of step y were performed by fixing the step x to be 0.125, and the results are shown in Figure A.7b. When step y changes from 0.125 (second to the last point) to 0.0625 (last point), energy gap changes by 0.063 %. Thus, 0.125 was chosen to be the step size in the y direction.

Given the spatial resolutions of x and y directions, the convergence tests were performed for the temporal step size. The test was performed by shuttling the electron $2.1\ \mu\text{m}$ from its initial position and calculating the loss probability and excitation fraction at the end of the shuttling. The results are shown in Figure A.8 with the y-axis in log scale. Even though the excitation fraction in Figure A.8b converges at the step size of 0.00625 (second to the last point), the corresponding loss probability in Figure A.8a only starts to converge at the step size of 0.003125 (last point). There is an order of magnitude change in the loss probability when

step size changes from 0.00625 to 0.003125. Thus, 0.003125 was chosen to be the temporal step size.

A.2.5 Numerical Precision

Results of Stationary Evolution

To benchmark the results of simulations of conveyor-belt shuttling, we performed stationary evolution of the initial state with initial potential for the same time duration as the duration of shuttling 140 nm with the speed of 10 m/s and amplitude of $A = 100$ mV, for $N = 3$ without noise. The loss probability was 4.43×10^{-11} , and the excitation fraction was 5.52×10^{-8} , which is smaller than the loss probability and excitation fraction for the corresponding shuttling scenario.

When there was a noise with the same parameters as the ones used in section 2.7, for one random run, the loss probability was 4.82×10^{-8} , and the excitation fraction was 5.12×10^{-8} . While the loss came out to be slightly bigger, the excitation fraction resulted in a smaller value. This shows that the noise changes the overall shape of the potential energy, changing the energy value of the ground state and characteristic energy gap in such a way that the excitation fraction came out to be slightly smaller.

Normalization Drift and Energy Oscillation

The sources of error are the trotterization error in the split operator method and the error below the tolerance threshold in the SOR. We observed two numerical artefacts: the normalization drift and the energy oscillation in the stationary potential. The simulation of shuttling with the target distance of 2.1 μm and the target speed 10 m/s was performed, and the normalization of the state during the entire process was recorded. At the end of the shuttling, there are additional 5000 time steps to do the stationary evolution with the final potential. During this additional 5000 time steps, the expectation value of energy was noted. In contrast to the reality, the normalization drifts from one by 10^{-8} during around 8×10^7 time steps. Furthermore, the energy expectation value after the shuttling oscillates by the scale of 10^{-8} meV.

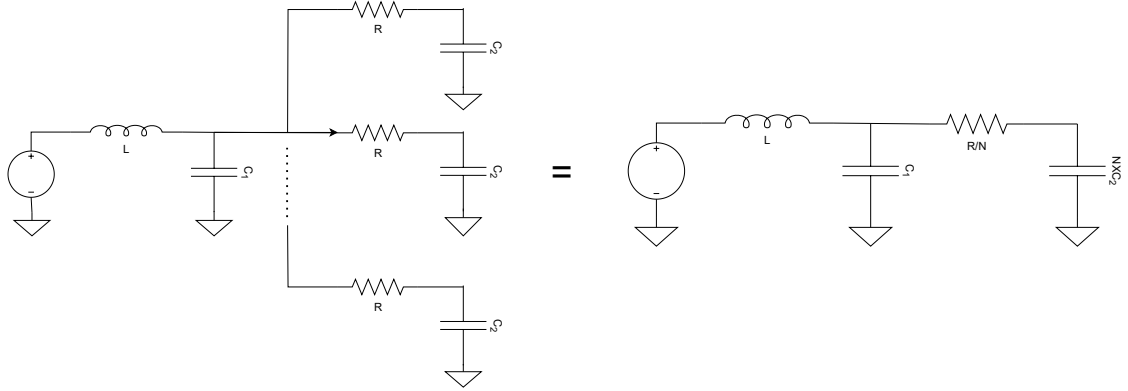


Figure A.9: (a) and (b) are equivalent circuits for lumped element model of a voltage source connected to N clavier gate(s) via a single bondwire. L is the inductance of the bondwire. C_1 is the capacitance of the bondpad, and C_2 is the capacitance of the clavier gates. R is the resistance of the metal connection from the bondpad to the gate.

Such artefacts set the guideline on how small a number should be to be considered as *numerical error*. The normalization drift is relevant to the loss probability as it calculates the probability of loss, i.e. the fraction of normalization outside of the potential well. The energy oscillation is relevant to the excitation fraction as the final energy is precise only up to the amplitude of oscillation. We claim that any number below these artefacts can be considered as a negligible quantity. One example is the probability of loss in shuttling of any distance in Figure 2.6b with no noise and no digitization.

A.2.6 Lumped Element Model of a Voltage Source connected to Clavier Gates

Figure A.9 shows the lumped element model, i.e. a simplified model, of a voltage source connected to the clavier gates for shuttling. Multiple clavier gates of capacitance, C_2 , are connected to a bondpad of capacitance, C_1 through metal connections of resistance, R . The bondpad is then connected to the voltage source via a bondwire of inductance L . The voltage source creates sinusoidal voltage pulses to the clavier gates as shown in Figure 2.3b. Due to thermal agitation, Johnson-Nyquist noise appear in the voltage pulse at the clavier gates, whose power spectral density is given by equation (2.5) at room temperature and equation (2.8) at cryogenic temperatures. For each element in Figure A.9, we estimated typical

values of the elements as $L = 1 \text{ nH}$, $C_1 = 5 \text{ fF}$, and $C_2 = 100 \text{ aF}$. The resistance was varied in the range of 100Ω to $2 \text{ M}\Omega$ to vary the cut-off frequency, γ .

A.2.7 Generation of Johnson-Nyquist Noise

Given the temporal step size, dt , in the time-dependent Schrödinger solver, one can obtain a discretized power spectral density with the grid spacing of $2\pi/(N_t \cdot dt)$, where N_t is the number of time steps of the entire shuttling process.

We first take the square root of the power spectral density to obtain the magnitudes of the modes at different frequencies. Then, we multiply each frequency mode by a random phase factor $e^{i\phi_j}$, where $\phi_j \in [0, 2\pi]$, and $j = 1, 2, \dots, N_t$. Finally, we perform a Fast Fourier transform of the modes to produce a random time series $X(t)$, with the normalisation chosen to ensure Parseval's theorem is obeyed, i.e. $\int dt |X(t)|^2 = \int d\omega S(\omega)$. The integrals were approximated by Riemann sums $\int dt |X(t)|^2 \approx \sum_{i=0}^{N_t} |X_i|^2 \Delta t$.

A.3 Additional Results of the Conveyor-Belt Mode Shuttling

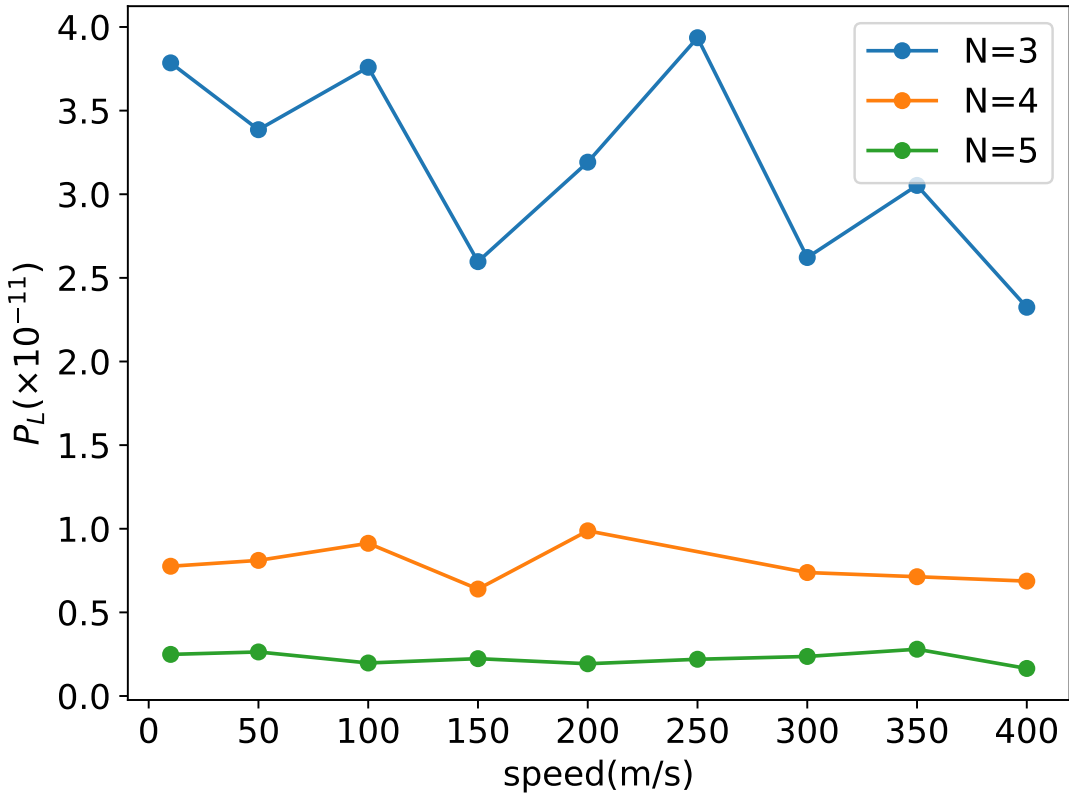
A.3.1 Noise-free Shuttling: Target Speed

Figure A.10 shows the loss probability and excitation fraction with different target speeds. The shuttling distance and the amplitude of signals were fixed to $1.4 \mu\text{m}$ and 100 mV , respectively. While there is no clear trend of increase or decrease of loss probability with increasing target speed, the excitation fraction shows an upward trend with increasing target speeds. In all of the cases, the loss probability is bounded by 4×10^{-11} and the excitation fraction is bounded by 1×10^{-5} .

A.3.2 Sensitivity to step-changes in voltage control

Since the majority of the results with smoothly varying potential without any noise proved to be good shuttling scenarios, we investigated how the abrupt changes in voltage control affect the loss probability and excitation fraction. In particular, we considered the scenario where we have a finite number of voltage settings at

(a)



(b)

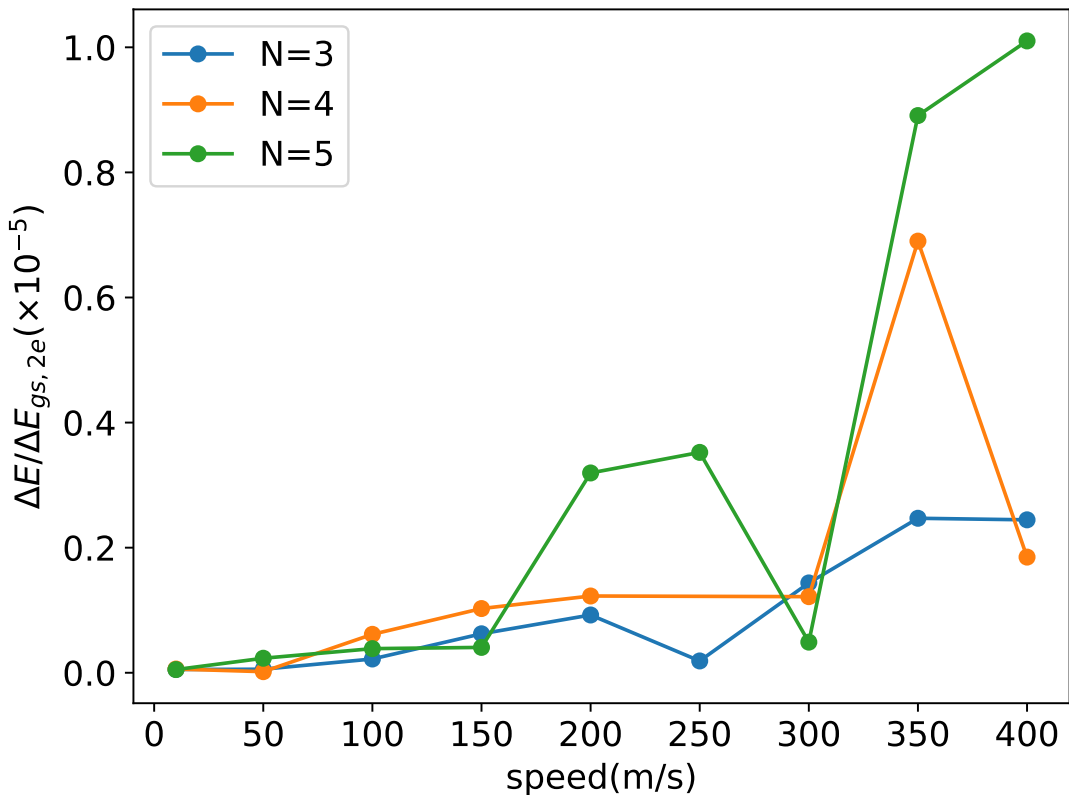
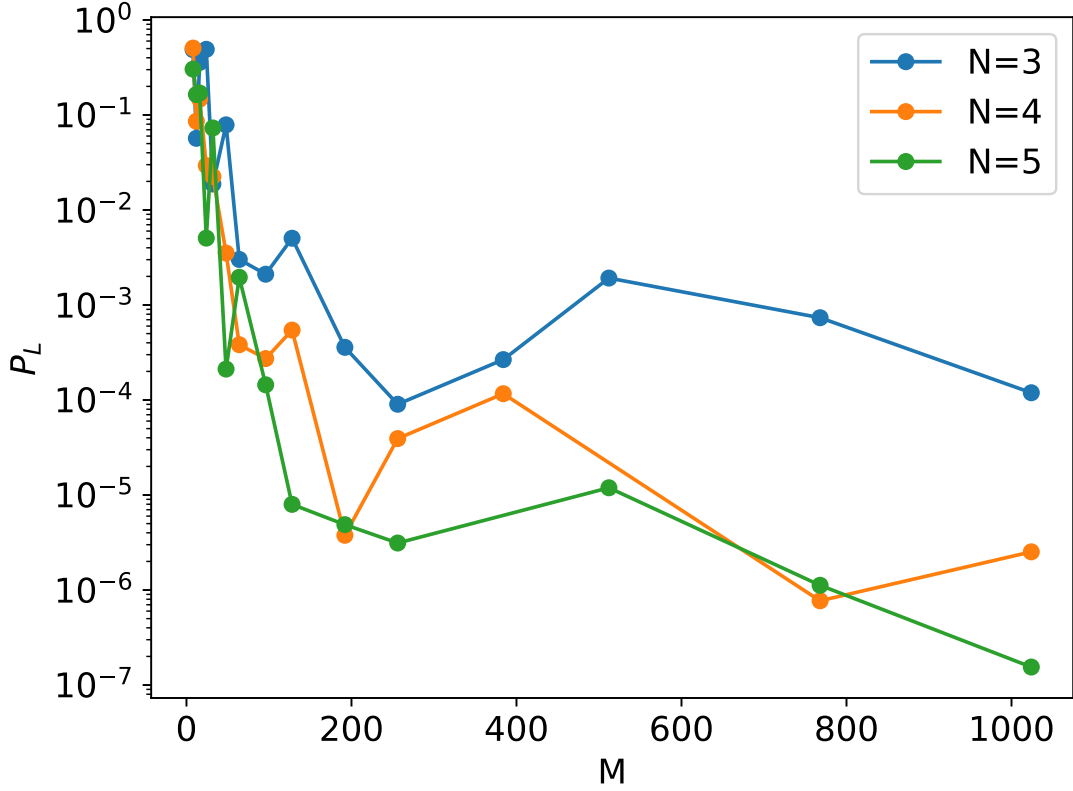


Figure A.10: (a) The loss probability and (b) excitation force with varying target speeds and the number of gates per unit cell.

(a)



(b)

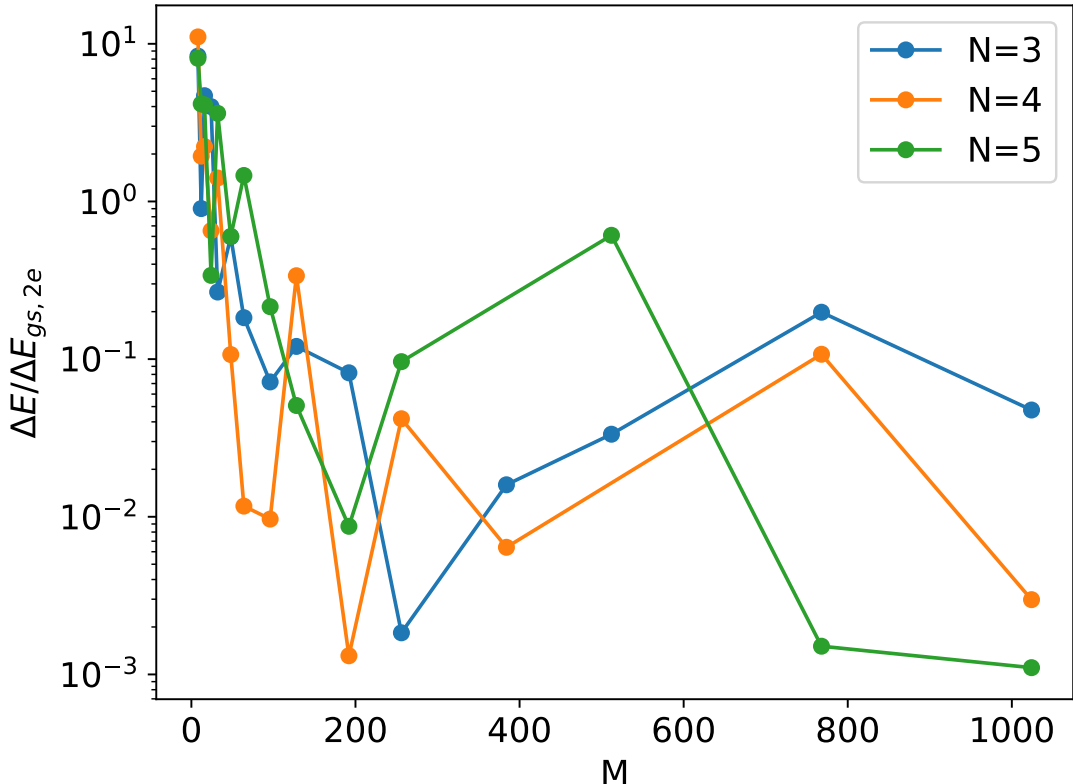
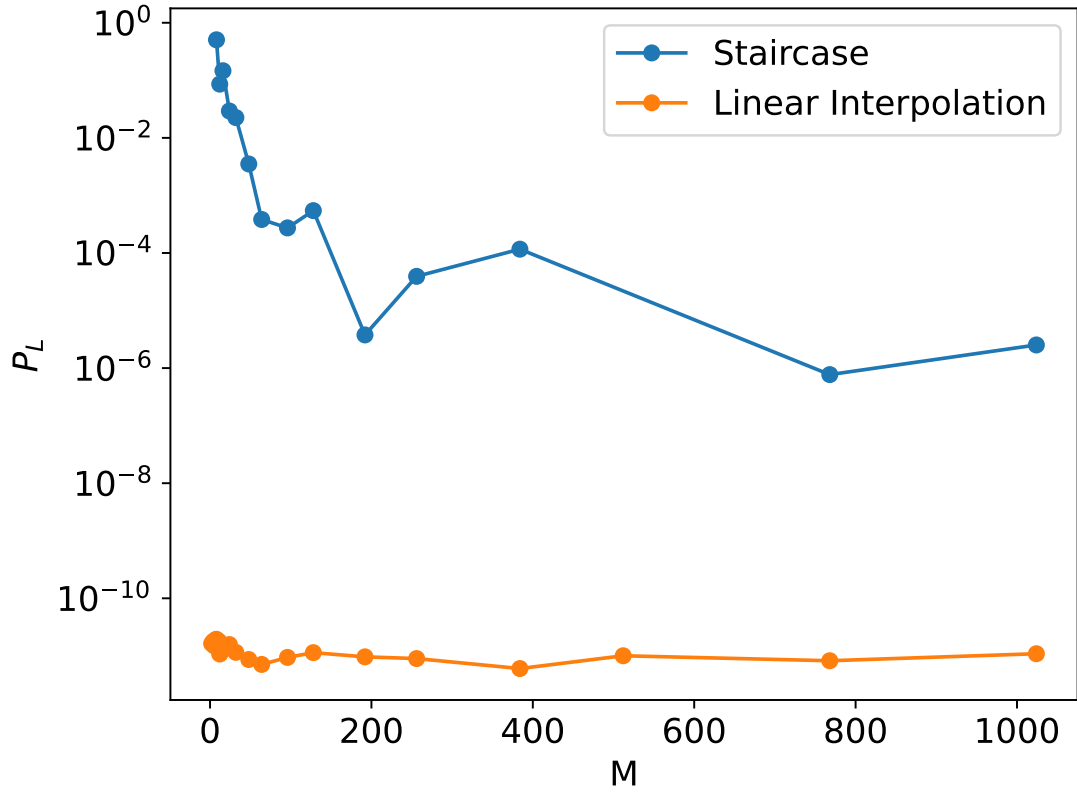


Figure A.11: (a) The loss probability and (b) excitation fraction with varying number of fixed potential settings and the number of gates per unit cell.

(a)



(b)

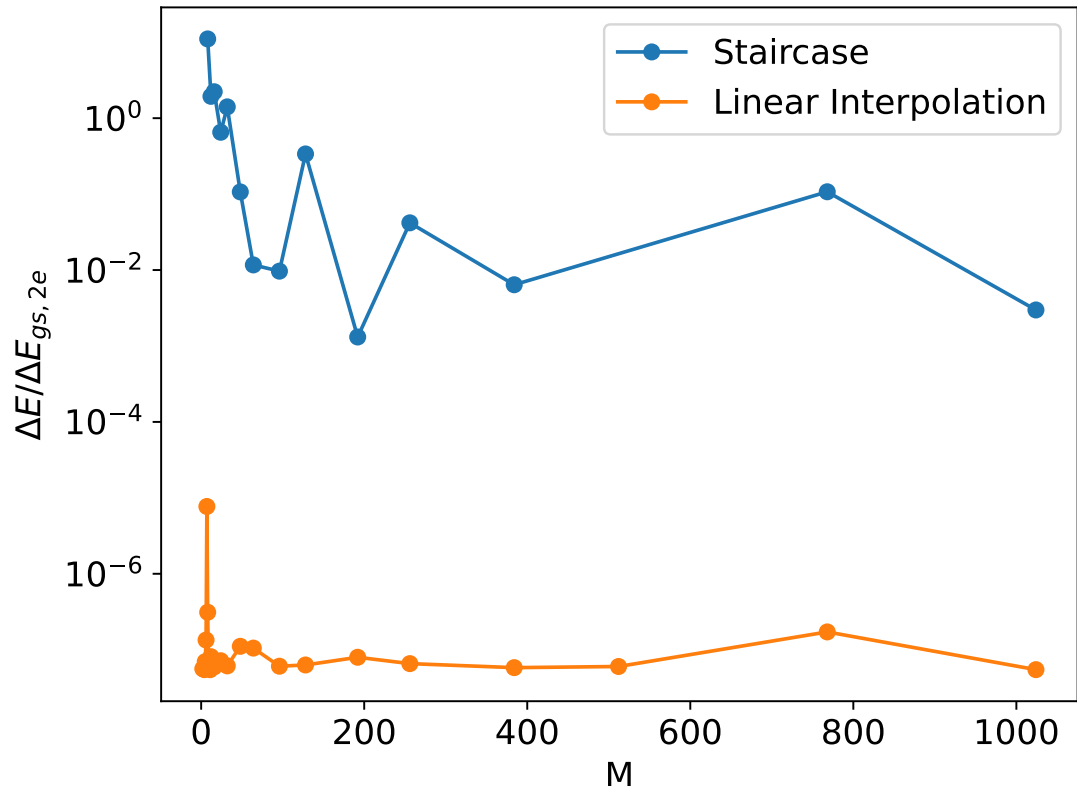


Figure A.12: (a) The loss probability and (b) excitation fraction of digitization mode 1 (Staircase) and digitization mode 2 (Linear Interpolation)

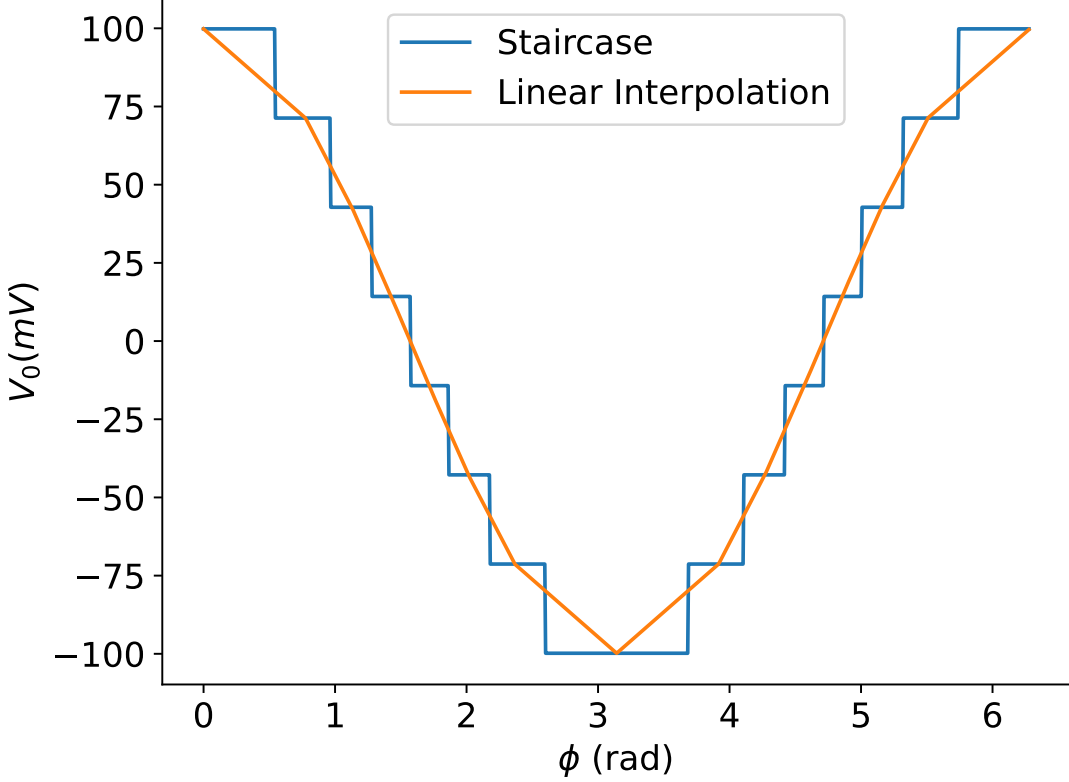


Figure A.13: An example of voltage signal on the 1st gate in the unit cell for digitization mode 1(blue line) and mode 2(orange line).

hand as if the voltage signals are digitized. While the phase varies linearly like in section 2.6, the sinusoidal voltage signals are mapped to the nearest voltage in the list of voltage settings:

$$m_*^i(t) = \underset{m}{\operatorname{argmin}} |A \cos\left(\phi(t) - \frac{2\pi i}{N}\right) - V_m| \quad (\text{A.4})$$

$$V^i(t) = V_{m_*^i(t)},$$

where N is the number of gates per unit cell, $\{V_m\}_{n=0,\dots,M-1}$ is the set of voltage settings, the superscript denotes the gate to which the voltage signal is applied and the subscript represents the voltage in the set of voltage settings. Thus, the voltage signals are step functions in time, which have step-changes in the voltage control. The blue line in figure A.13 shows an example of such voltage signal.

On the other hand, we investigated another way of using the finite number of voltage settings such that the voltage is linearly interpolated between the two nearest

voltage settings. To be specific, the voltage signals are made by linearly interpolating the mid points of the steps in the prior case as the orange line shows in figure A.13. Such signal is the opposite extreme from the prior case as there is no step-change in the voltage signal. Let's call the two methods digitization-mode 1 and 2, respectively.

Figure A.12 shows the loss probability and excitation fraction of digitization mode 1 and 2 with different number of settings, M . This shows that the abrupt change in the voltage signal is detrimental to the quality of shuttling such that digitization-mode 2 with only two settings works as good as any other number of settings, i.e. $P_L \lesssim 2 \times 10^{-11}$. In contrast, the loss probability is 0.5 when there are only two settings.

In this section, we conclude that discontinuities in voltage signals, such as the steps in staircase-like potential, significantly degrades the quality of shuttling, and this was observed by comparing the two digitization modes. Despite of this conclusion, we invented our new non-adiabatic shuttling method, which uses discontinuous updates of the potential (See section 2.9). Furthermore, this new method allows arbitrarily fast shuttling speeds, which can be controlled by the number of updates per unit cell and the strength of the gate voltages. This suggests that, while discontinuities in the voltage signals should be avoided, they can be useful when they are made at the right timings like our new method.

A.3.3 Sensitivity to Classical Johnson Nyquist Noise

In this section, we present simulation results of shuttling with classical Johnson-Nyquist noise, whose power spectral density is given by equation 2.5 without the quantum correction factor. Note that the classical Johnson-Nyquist noise formula is only valid when the cut-off frequency and temperature satisfies $\gamma \lesssim \frac{k_B T}{\hbar}$.

Figure A.14a and Figure A.14c show the loss probability and excitation fraction for different cut-off frequencies, γ , and different numbers N of electrodes per unit cell. The temperature was chosen to be 4 K, which resulted in RMS noise of 0.118 meV. Figure A.14a shows that shuttling is sensitive to high frequency noise ($\omega/2\pi > 1$ THz) as the loss probability reaches 10^{-4} for both $N = 4$ and

$N = 5$ when the cut-off frequency reaches 10 THz, i.e. $\gamma = 10$ THz. Note that the characteristic energy gap is 6.02 meV, which corresponds to the frequency of 1.46 THz, i.e. $\omega_c/2\pi = \Delta E_{gs,2e}/h = 1.46$ THz. Thus, we conclude that the effect of noise becomes severe as the cut-off frequency becomes comparable to the characteristic energy gap. Furthermore, the shuttling process is more resilient to the noise when there are more gates per unit cell. This is because the QD becomes deeper, and the inter-dot distance becomes longer, for more number of electrodes per unit cell. The inter-dot distance is equal to the length of unit cell, which is $(35 \times N)$ nm in our case. The depths of QD for $N = 3, 4, 5$ are 49 mV, 69.5 mV, and 71.5 mV, respectively. Thus, given the same cut-off frequency, the loss probability goes down by couple of orders of magnitude as N increases from 3 to 5. The excitation fraction does not reduce as dramatically as the loss probability when N increases; hence, the primary motivation to use more of electrodes per unit cell is to reduce the loss probability.

Figures A.14b and A.14d show the loss probability and excitation fraction as a function of temperature for different cut-off frequencies, i.e. $\gamma = 10, 100, 1000$ GHz. As the temperature increases, the RMS noise increases (equation 2.6); to avoid growth in the loss probability and excitation fraction, it is therefore beneficial to perform shuttling at low temperature with large number of electrodes.

Figure A.15 shows the probability of excitation to the eigenstates of the instantaneous Hamiltonian at the end of the shuttling process for the case of three gates per unit cell. The dominant excitation are to the second excited state and seventh excited states, which are the first and second excited states in the direction of shuttling (See Figure A.6). With increasing cut-off frequencies and higher temperatures, we can see that the probability to remain in the ground state decreases while the probability of excitation to the second excited increases.

A.3.4 Speed Vs. Adiabaticity

Figure A.16 shows the probability of excitation outside of the ground state and the excitation fraction with 5 different shuttling speeds, i.e. 10, 50, 100, 300, 500 m/s.

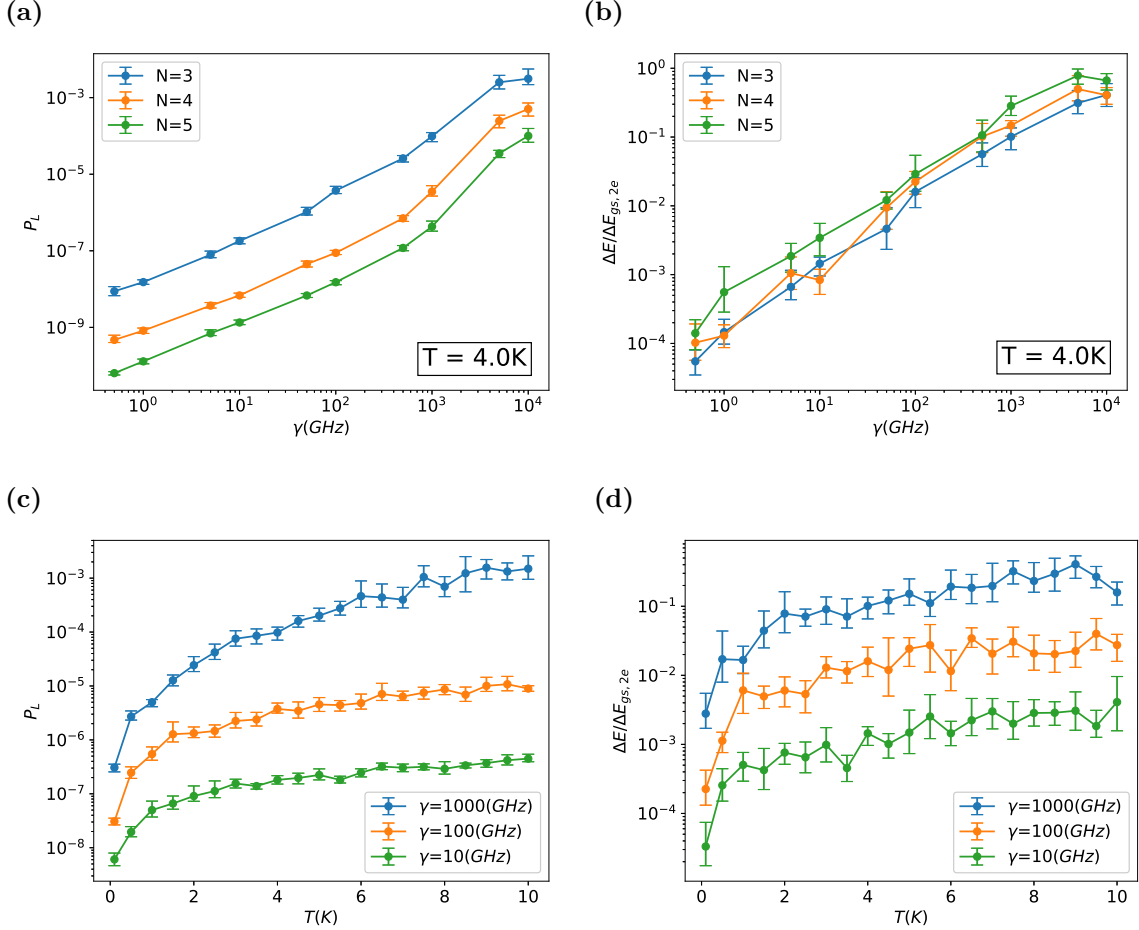
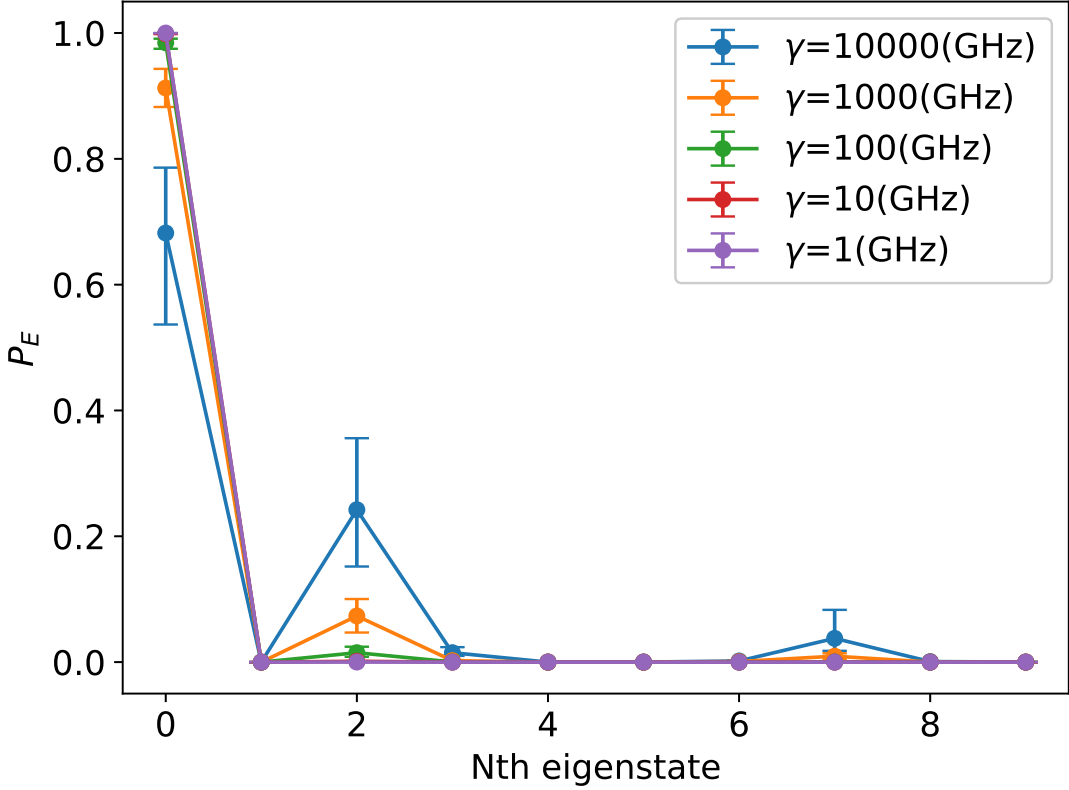


Figure A.14: The loss probability and excitation fraction for classical Johnson-Nyquist noise: (a) loss probability and (b) excitation fraction as a function of cut-off frequency γ , at $T = 4\text{K}$; (c) loss probability and (d) excitation fraction as a function of temperature with three different cut-off frequencies, $\gamma = 10, 100, 1000\text{GHz}$.

Other parameters were chosen realistically, $A = 50\text{mV}$, $T = 2\text{K}$, and $N = 3$. Data for 10 m/s are identical to those of Figure 2.9 in section 2.10: The probability of excitation and excitation fraction at 10 m/s shows a regular behaviour of increase from 0 to 1.3×10^{-5} for the excitation probability and around 10^{-6} . In contrast, we observed irregular behaviours, which could be a sign of non-adabaticity, such that there are sharp peaks at $D = 0.47\mu\text{m}$ and $D = 1.35\mu\text{m}$ for speeds greater than or equal to 50 m/s. The height of the peak increase as the shuttling speed increases, and the excitation fraction goes up to 10^{-3} for 300 m/s. This suggests that the impact of orbital excitation to the spin grows with the shuttling speed as more orbital excitation happens with higher excitation speed resulting in higher

(a)



(b)

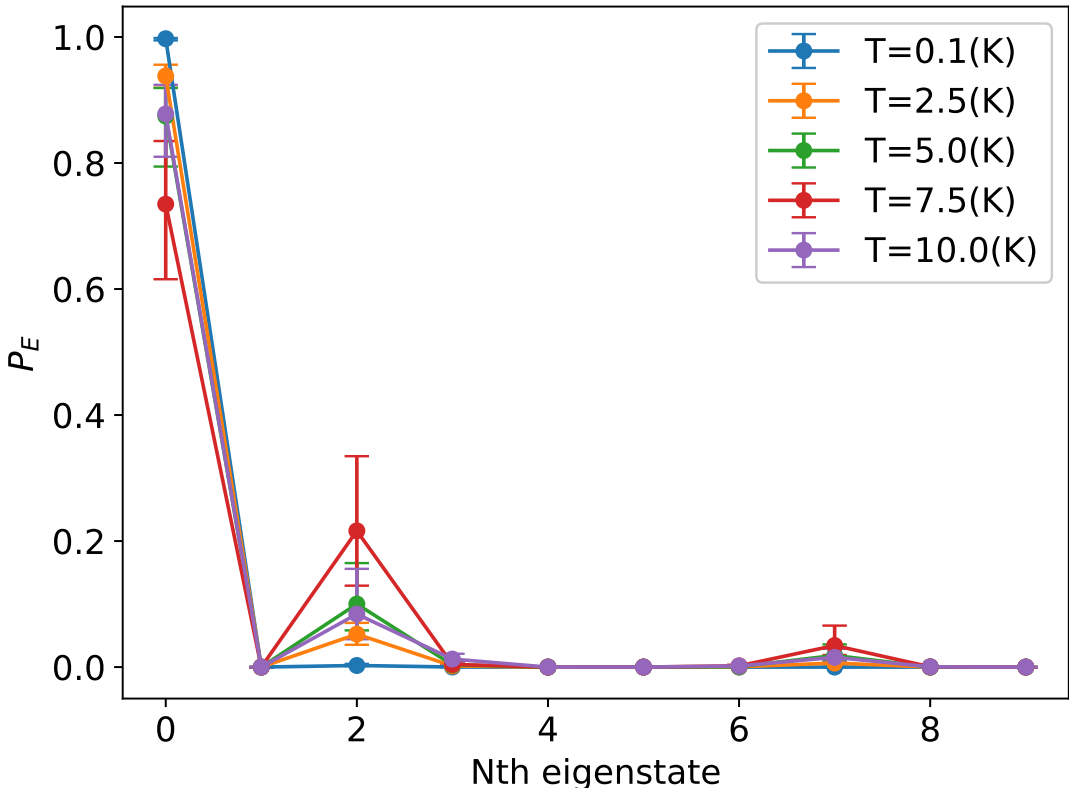
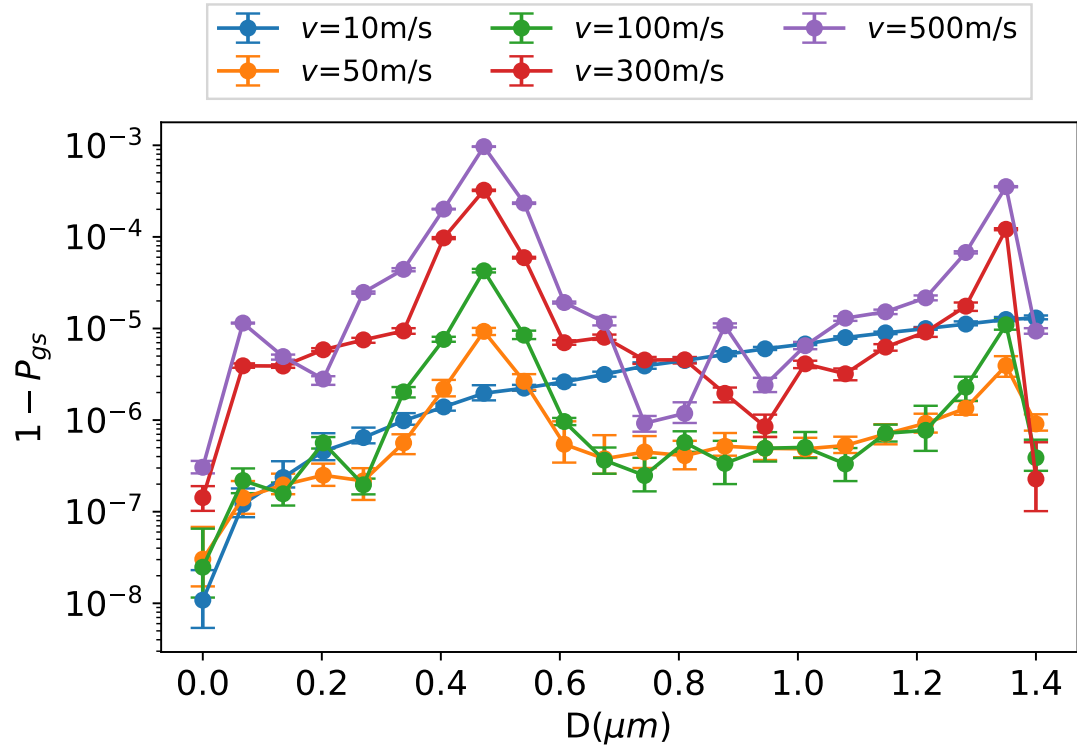
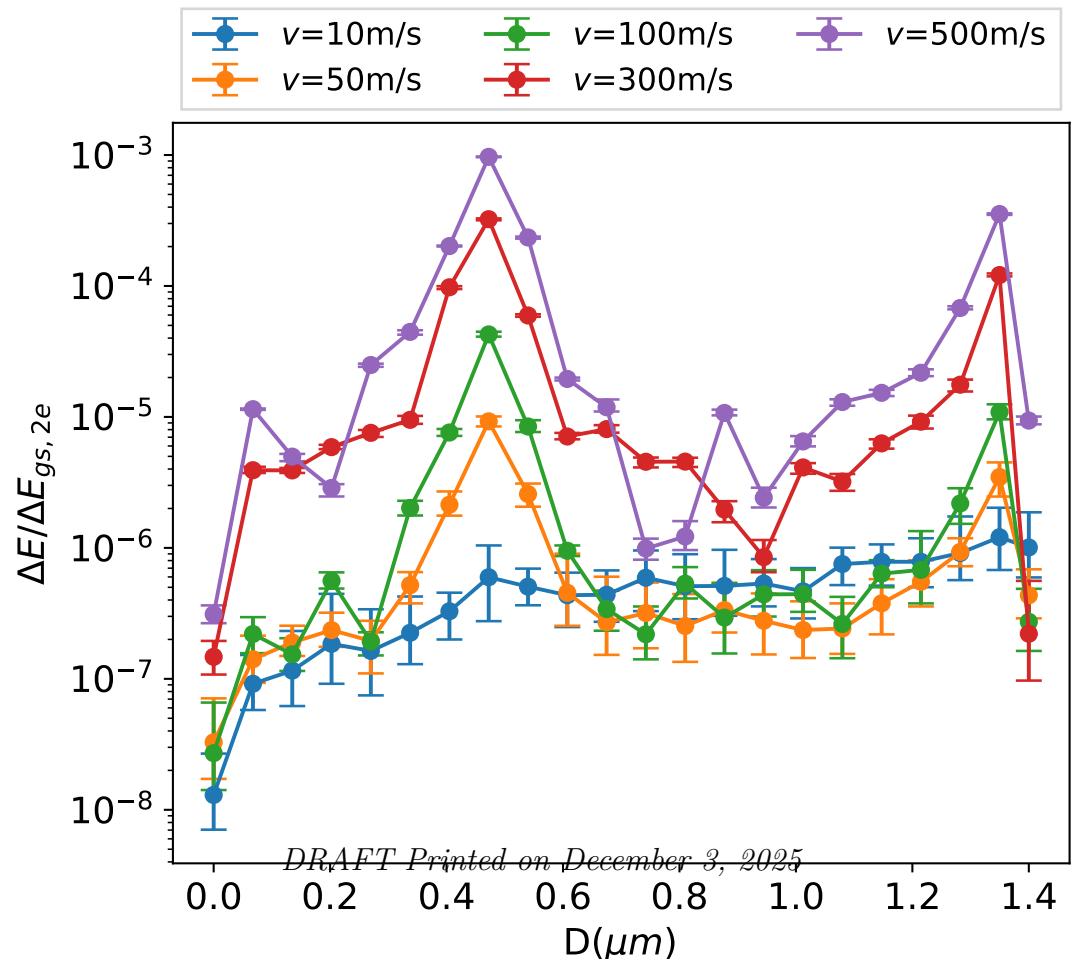


Figure A.15: The probability P_E of excitation to eigenstates of the instantaneous Hamiltonian for various (a) noise fractions and (b) cut-off frequency.

(a)



(b)



change of random phonon relaxation happening during the shuttling. The causes of the peaks at those particular positions could be studied in future works.

A.3.5 Sensitivity to Charge Defects: Two Defects of Varying Separations.

Figure A.17 shows the probability amplitude of the electron when it tunnels through the barrier created by two charge defects of varying separations $\Delta y = 2, 12, 25$, and 30 nm . The images were taken at the time step when the expectation value of position in x-axis coincides with the x-axis coordinate of the defects. When two charge defects are close to each other, there is enough room for the electron to move around the central barrier at the sides of the channel. When two charge defects are far enough from each other, the central barrier is low enough for the electron to pass through the middle of the channel. However, when the distance between the defects makes both of these options hard, passage over the barrier produces significant excitation in the electron state.

A.4 Results of Advanced Non-Adiabatic Ultra-fast shuttling

In this section, we present the results and analysis of simulation of the new non-adiabatic shuttling method, namely the snap method, proposed in section 2.9. This scheme depends on how closely the trough of the potential energy can be approximated by an SHO potential in the range $x \in [x_0 - \Delta x, x_0 + \Delta x]$, where x_0 is the current position of the minimum of the potential energy: if the potential is perfectly harmonic, the displaced ground state forms a coherent state that moves in the potential without changing its spatial form, and step (3) exactly recovers the ground state of the final potential.

As the channel is placed deeper (i.e. more negative z), the shape of the potential becomes more harmonic, while the amplitude of the signal at the channel decreases. While the approach of the potential to the SHO potential limit benefits the shuttling,

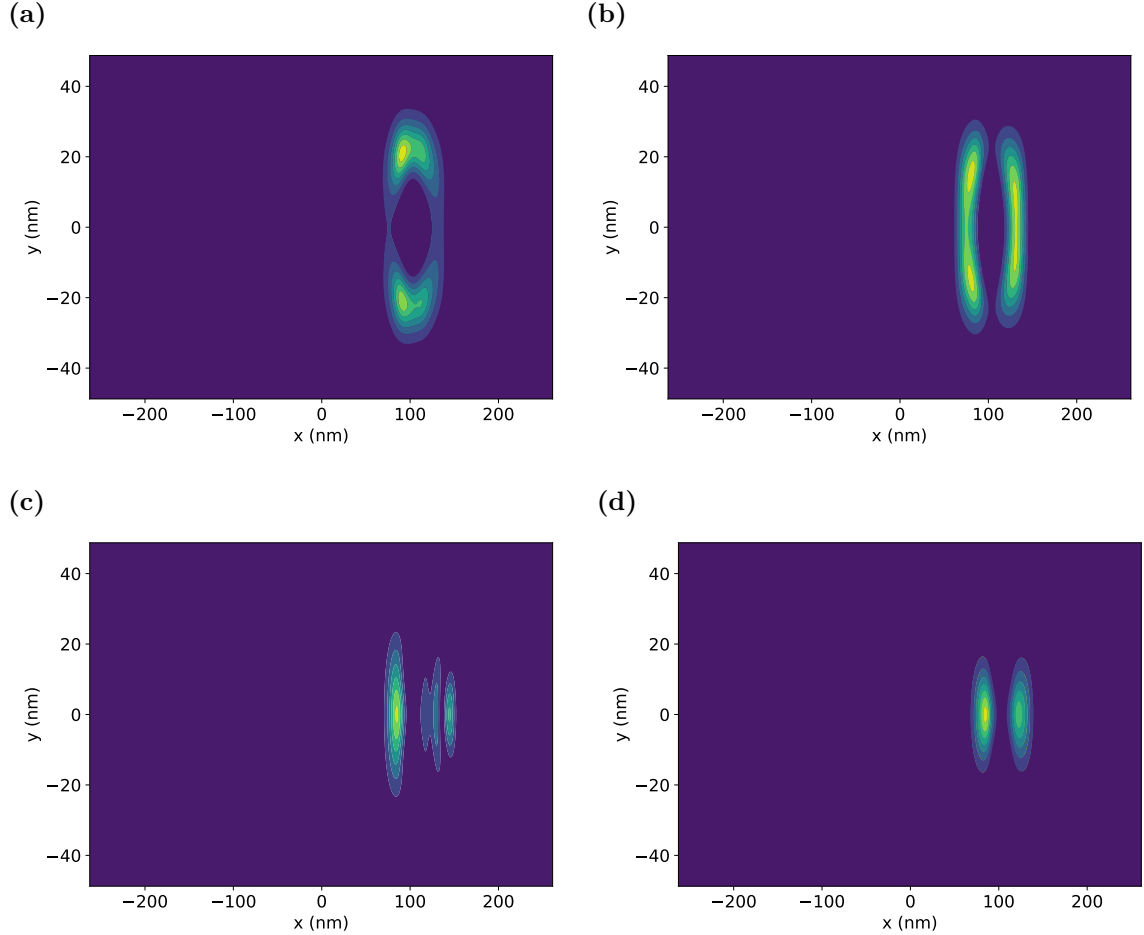


Figure A.17: Contour plots of probability amplitudes of the electron moving through two charge defects for (a) $\Delta y = 2 \text{ nm}$, (b) $\Delta y = 12 \text{ nm}$, (c) $\Delta y = 25 \text{ nm}$, (d) $\Delta y = 30 \text{ nm}$. When the separation of two charge defects is small, ($\Delta y = 2, 12 \text{ nm}$), the electron moves around the defects as in (a) and (b). When the separation is large ($\Delta y = 30 \text{ nm}$) the electron moves through the middle without significant excitation as in (d). When neither of these actions is easy (e.g. $\Delta y = 25 \text{ nm}$), the tunneling through the barrier produces significant excitation in the state, as in (c).

the smaller amplitude makes the loss probability bigger. Thus, these two factors compete with each other as the channel is placed deeper.

If the target distance is a multiple of the length of one unit cell, we can have a finite set of Δt and Δx such that it can be repeatedly used after shuttling the electron by the length of one unit cell. Let M be the number of instantaneous changes in potential while traversing one unit cell; as M increases, the average speed of shuttling decreases with both increasing M and increasing depth, as shown in Figure A.18, because the interval between changes is set by the curvature

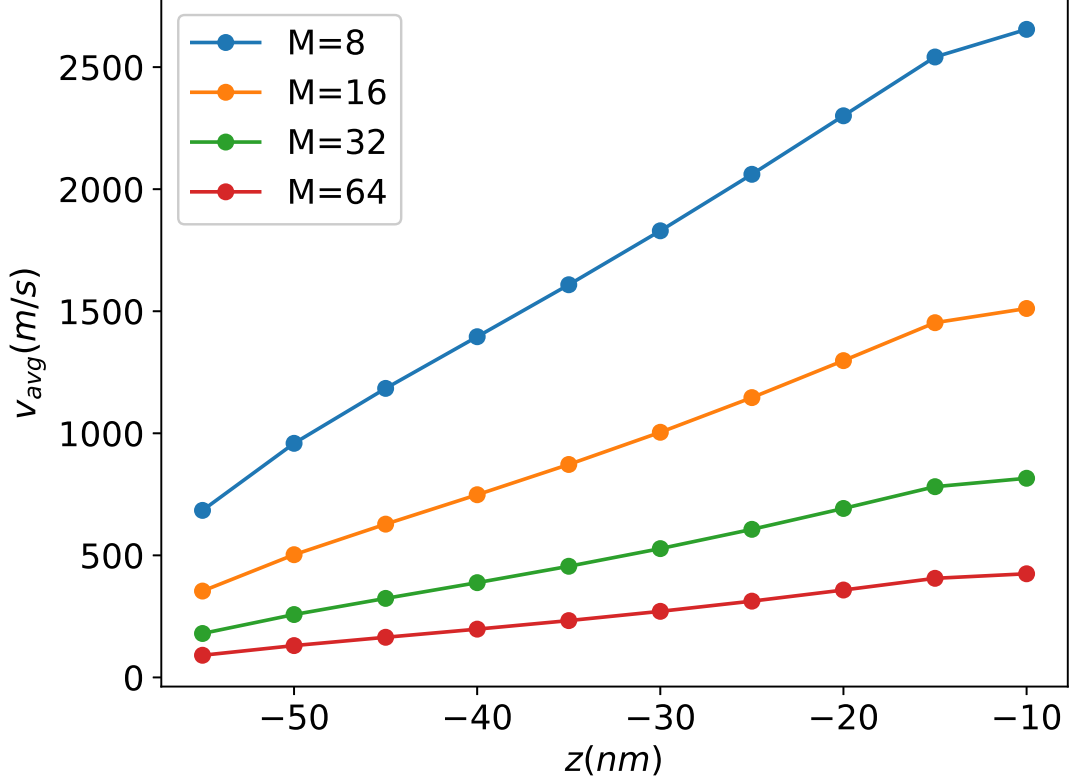


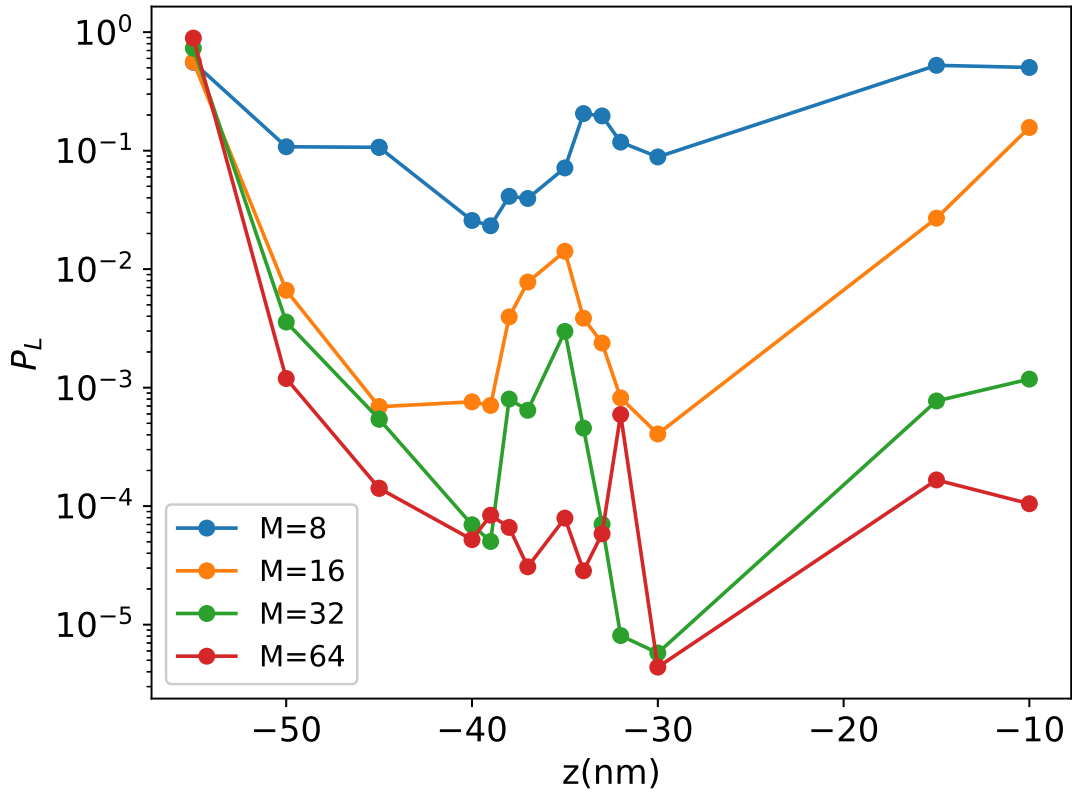
Figure A.18: The average speed of adiabatic shuttling at varying depths with different number of instantaneous updates of the potential(M).

of the potential minimum.

Figure A.19a shows the competition of the two factors: closeness to the SHO potential (See Figure A.21) and the amplitude of the voltage signal. The amplitude of the gate voltage was fixed at 100 mV. As z becomes more negative, the loss probability and excitation fraction initially decrease, then increase beyond a certain point, e.g. at $z = -30$ nm for $M = 64$ (red line). In the range $z = -30$ nm to $z = -40$ nm, there is a local maximum in both loss and excitation for all M ; for $M = 64$, this maximum takes the form of a sharp peak at $z = 32$ nm, followed by oscillations in the loss probability. We can see similar local maxima and oscillation of excitation fraction in Figure A.19b.

While this could be understood as another manifestation of the trade-off between the two factors mentioned earlier, it means that small errors in the timings of instantaneous changes to the potential (the ‘snaps’) can lead to large changes in the

(a)



(b)

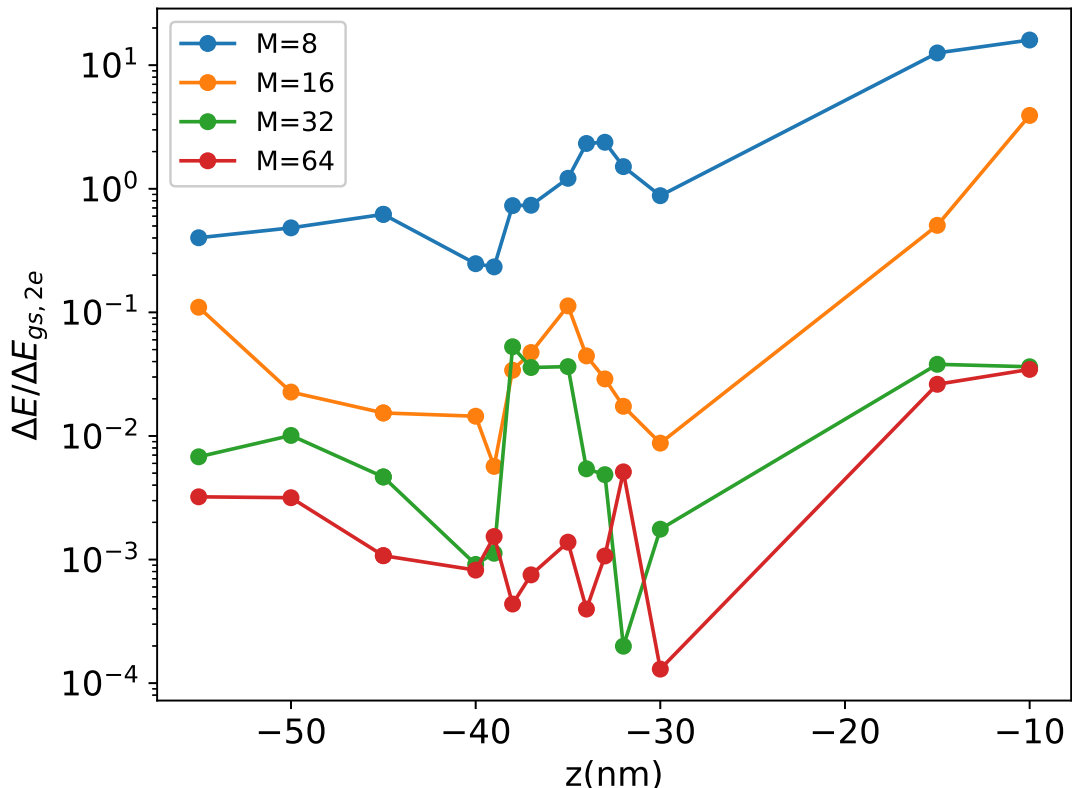


Figure A.19: (a) Loss probability and (b) Decimation fraction of the non-adiabatic shuttling at the varying depth(z) with different number of instantaneous updates of the potential(M).

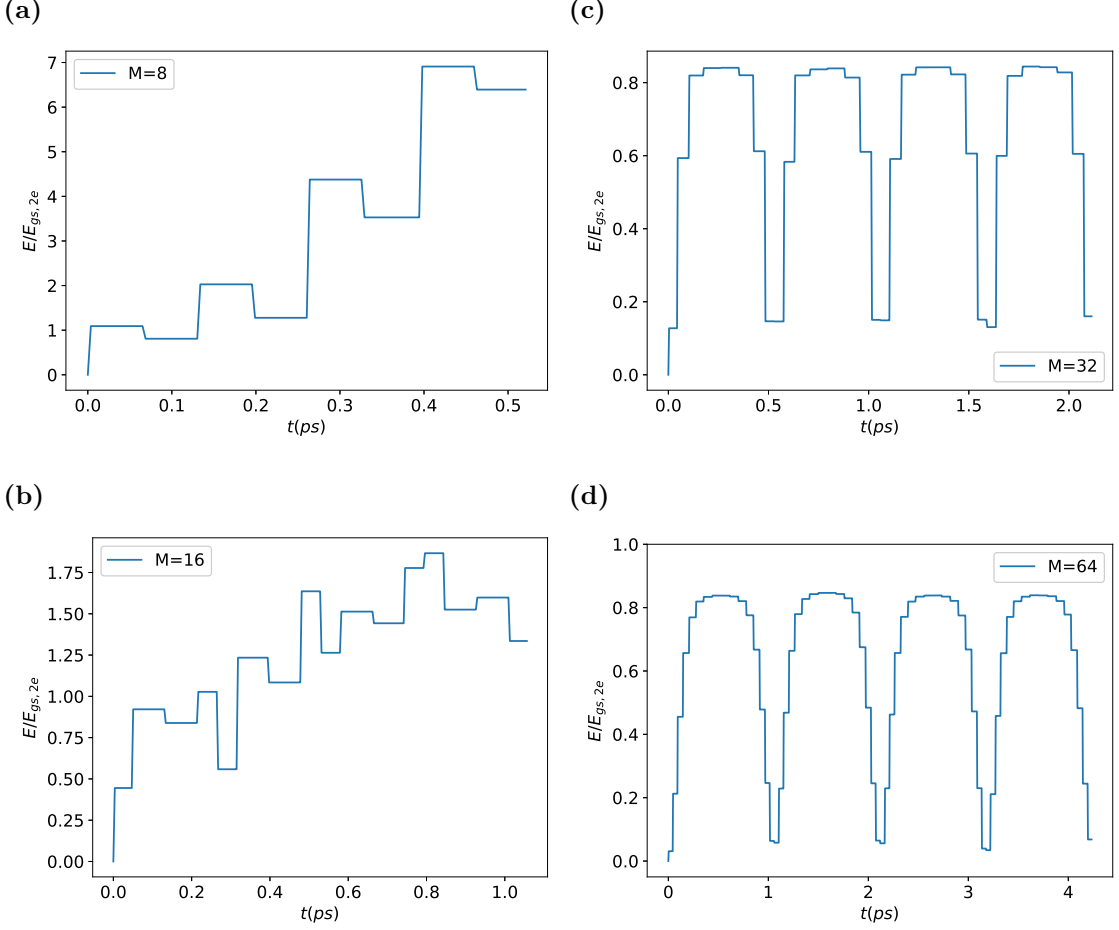
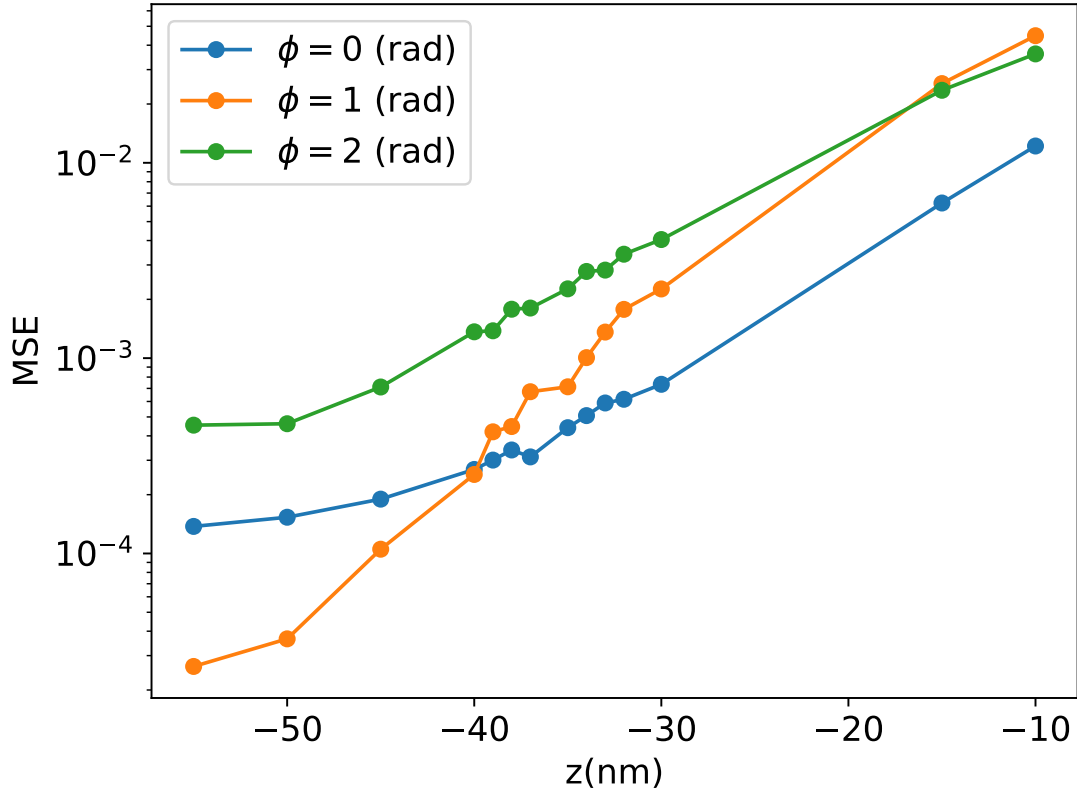


Figure A.20: Fractional excitation energy in the fast non-adiabatic shuttling method for different values of M : (a) $M = 8$, (b) $M = 16$, (c) $M = 32$, (d) $M = 64$. The method becomes more stable and have a periodic behaviour as the number of instantaneous changes, M , per unit cell increases.

quality of the shuttling. Errors in the update timings can lead to a de-synchronising between the electron's motion and the updates to the potential, and consequent excitation out of the desired mode.

As one might expect, it is possible to systematically optimise beyond the initial timings obtained from the idealised analytic model. We explored this using Limited-memory BFGS (L-BFGS)[90], and setting the final energy of the shuttling as a target function. Optimisation led to improvement in both the loss probability and excitation fraction. In the chosen scenario, the number of electrodes used was $N = 4$, the number of instantaneous changes within one unit cell was set to $M = 8$, the amplitude of voltage at the gate was set to $A = 100$ mV, while the position of

(a)



(b)

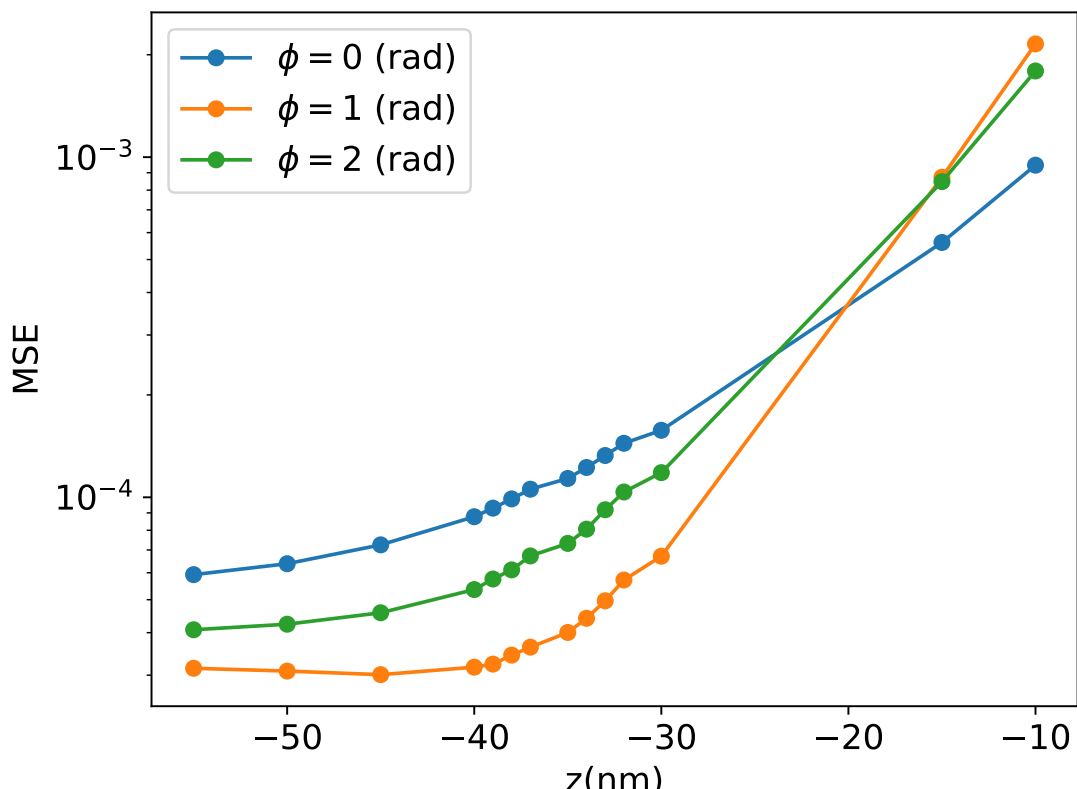


Figure A.21: The mean squared error (MSE) between the normalized potential, i.e. $\max|V_\phi(x)| = 1$ and two different functions: (a) $\cos(x)$ and (b) the quadratic fit at the bottom at three different phases, $\phi = 0, 1, 2$ rad. This shows that the potential becomes more like a sinusoidal function and that quadratic fit becomes better when the potential

the channel was $z = -30 \text{ nm}$. With the default convergence criteria of the Scipy implementation[104] adopted, we observed a reduction of the final loss probability by about 25 % (from 0.089 to 0.066) and a reduction of 40 % in the excitation fraction (from 0.88 to 0.53). No doubt further improvements could be made via other methods or other cost functions, e.g. excitation fraction or final loss probability.

Aside from optimising the ‘snap’ event time intervals, a basic challenge for this non-adiabatic shuttling scheme is that the voltage changes are faster than the limits with current technology (around 14 mV/ps). In our model, the minimum rate of voltage change for $M = 64$ at $z = -10 \text{ nm}$ was 5 V/ps, which is around 400 times higher than the 14 mV/ps. Further investigation can be made with slower voltage change: However, we expect that it would deteriorate the overall performance as the timings of instantaneous changes should be exact to seamlessly transport the electron. Furthermore, the presence of charge defects will make this method worse as the timings of instantaneous changes are affected by them. In particular, when the electron is near the charge defect and repelled by the Coulomb repulsion, the electron will linger longer to tunnel through the potential barrier.

Given these limitations, this ‘snap’ method seems unrealistic for implementation with foreseeable technologies. However, in an era where silicon-based quantum devices are mature it might perhaps be an exploitable concept.

Cor animalium, fundamentum est vitæ, princeps omnium, Microcosmi Sol, a quo omnis vegetatio dependet, vigor omnis & robur emanat.

The heart of animals is the foundation of their life, the sovereign of everything within them, the sun of their microcosm, that upon which all growth depends, from which all power proceeds.

— William Harvey [harvey_exercitatio_1628]



Appendix of Noise-aware Time-optimal Quantum Control

Contents

B.1 Commutation between unitary and dissipative part	100
B.2 Commutation and Fidelity of Pauli channel	101
B.2.1 Pauli channel from Lindblad master equation	101
B.2.2 Transformation between Pauli transfer matrix and Pauli channels	103
B.2.3 Example: dephasing noise	104
B.2.4 Group channels	105
B.2.5 Example: Depolarising channel	107
B.2.6 Example: Two-qubit Dipole-Dipole Noise Channel	108
B.2.7 The Application of Noise channels for Gate Compilation	108
B.3 Choi States	109
B.4 Numerical Simulations	110
B.4.1 Implementation of CRAB and TCRAB	110
B.4.2 Hyper-parameters	114
B.5 Additional Numerics	115
B.6 Oscillation of Optimised Fidelity	115
B.7 Identity Test	118

B.1 Commutation between unitary and dissipative part

The Liouville form of the Lindblad master's equation is

$$\frac{d}{dt}|\rho\rangle\langle\rho| = \mathcal{L}|\rho\rangle\langle\rho| = (\mathcal{L}_H + \mathcal{L}_D)|\rho\rangle\langle\rho|$$

where

$$\begin{aligned}\mathcal{L}_H &= -i(I \otimes H - H \otimes I) \\ \mathcal{L}_D &= \sum_k \left(L_k^* \otimes L_k - \frac{1}{2} \left(I \otimes L_k^\dagger L_k \right) - \frac{1}{2} \left((L_k^\dagger L_k)^* \otimes I \right) \right).\end{aligned}$$

Hence, the commutator between the unitary and dissipative part is

$$\begin{aligned}[\mathcal{L}_H, \mathcal{L}_D] &= -i \sum_k \{ [I \otimes H, L_k^* \otimes L_k] - [H \otimes I, L_k^* \otimes L_k] \} \\ &\quad + \frac{i}{2} \sum_k \left\{ [I \otimes H, I \otimes L_k^\dagger L_k] - [H \otimes I, (L_k^\dagger L_k)^* \otimes I] \right\} \\ &= -i \sum_k \{ L_k^* \otimes [H, L_k] - [H, L_k^*] \otimes L_k \} \\ &\quad + \frac{i}{2} \sum_k \left\{ I \otimes [H, L_k^\dagger L_k] - [H, (L_k^\dagger L_k)^*] \otimes I \right\}\end{aligned}$$

Let us define $C_k = [H, L_k]$, we then have:

$$\begin{aligned}[H, L_k^*] &= [H, L_k]^* = C_k^* \\ [H, L_k^\dagger] &= -[H, L_k]^\dagger = -C^\dagger \\ [H, L_k^\dagger L_k] &= L_k^\dagger [H, L_k] + [H, L_k^\dagger] L_k = L_k^\dagger C_k - C_k^\dagger L_k \\ [H, (L_k^\dagger L_k)^*] &= (L_k^\dagger C_k)^* - (C_k^\dagger L_k)^*\end{aligned}$$

$$\begin{aligned}[\mathcal{L}_H, \mathcal{L}_D] &= -i \sum_k \{ L_k^* \otimes C_k - C_k^* \otimes L_k \} \\ &\quad + \frac{i}{2} \sum_k \left\{ I \otimes (L_k^\dagger C_k - C_k^\dagger L_k) - ((L_k^\dagger C_k)^* - (C_k^\dagger L_k)^*) \otimes I \right\}\end{aligned}$$

In this form, we can see that one possible way for this to be zero is to have

$$C_k = [H, L_k] = \lambda_k L_k \tag{B.1}$$

for some real number λ_k , which can be verify by direct substitution. Physically this means that the jump operator L_k will take an eigenvector $|E\rangle$ of H with energy E to another (unnormalised) eigenvector $L_k|E\rangle$ of energy $E + \lambda_k$:

$$\begin{aligned}[H, L_k]|E\rangle &= HL_k|E\rangle - L_kH|E\rangle = \lambda_kL_k|E\rangle \\ HL_k|E\rangle &= (E + \lambda_k)L_k|E\rangle\end{aligned}$$

Note that Eq. (B.1) also implies

$$[H, L_k^\dagger L_k] = L_k^\dagger C_k - C_k^\dagger L_k = 0.$$

This is a weaker condition than Eq. (B.1) and thus does not guarantee the commutation between \mathcal{L}_D and \mathcal{L}_H . It ensures the forward plus backward jump preserves the eigenbasis of H , but not necessarily for individual jumps. Note that $L_k^\dagger L_k$ physically correspond to the decoherence rate of the k th decoherence process and its commutation with H means it does not change with time.

B.2 Commutation and Fidelity of Pauli channel

B.2.1 Pauli channel from Lindblad master equation

The set of Pauli operators is denoted as $\mathbb{G} = \{G_k\}_{k=0}^{4^N-1}$ with $G_0 = I$. For a given Pauli operator G_k , we can denote the correponding Pauli superoperator \mathcal{G}_k acting on the incoming operator ρ as $\mathcal{G}_k(\rho) = G_k\rho G_k^\dagger$. In this way, we can write the Lindblad master equation with Pauli jump operators $L_k = \sqrt{\gamma_k/2}G_k$ as:

$$\mathcal{L}_D = \sum_{k=0}^{4^N-1} \frac{\gamma_k}{2} (\mathcal{G}_k - \mathcal{I}) \quad (\text{B.2})$$

Do note that the contribution from the $k = 0$ term is always 0 since $\mathcal{G}_0 = \mathcal{I}$, thus we can set γ_0 to any number we want without affecting the dynamics.

In the rest of section, we will use the formalism of Pauli transfer matrix, which is essentially the matrix representation of the superoperator in the Pauli basis $\{2^{-N/2}|G_k\rangle\}$, where the factor of $2^{-N/2}$ is to normalise the Pauli basis such that $2^{-N}\langle\langle G_k | G_k \rangle\rangle = 1$. We will further use

$$\eta_{jk} = \eta(G_j, G_k) = G_k G_j G_k^{-1} G_j^{-1}$$

to denote the commutator between G_j and G_k .

In this way, the action of \mathcal{G}_k in the Pauli transfer matrix formalism is given by:

$$\begin{aligned} \mathcal{G}_k |G_j\rangle\langle G_j| &= \begin{cases} |G_j\rangle\langle G_j| & \eta_{jk} = +1 \\ -|G_j\rangle\langle G_j| & \eta_{jk} = -1 \end{cases} \\ \Rightarrow \quad \mathcal{G}_k &= 2^{-N} \sum_{j=0}^{4^N-1} \eta_{jk} |G_j\rangle\langle G_j| \end{aligned} \quad (\text{B.3})$$

Substituting back into Eq. (B.2), we have:

$$\begin{aligned} \mathcal{L}_D &= 2^{-N} \sum_{j=0}^{4^N-1} \sum_{k=0}^{4^N-1} \frac{\gamma_k}{2} (\eta_{jk} - 1) |G_j\rangle\langle G_j| \\ &= 2^{-N} \sum_{j=0}^{4^N-1} (-\lambda_j) |G_j\rangle\langle G_j| \end{aligned} \quad (\text{B.4})$$

where

$$\lambda_j = \sum_{k=0}^{4^N-1} (1 - \eta_{jk}) \frac{\gamma_k}{2} = \sum_{k, \eta_{jk}=-1} \gamma_k. \quad (\text{B.5})$$

i.e. the dissipative Lindbladian is diagonalised in the Pauli basis, each associated with a decay constant λ_j given by the sum of the strength of the individual noise components that anti-commute with G_j . Note that again the factor 2^{-N} is here to normalise the Pauli basis, i.e. the set of orthonormal basis is $\{2^{-N/2}|G_j\rangle\}$, it is not part of the eigenvalue. Since this is a diagonal matrix, it can be directly exponentiated to obtain the action of the resultant Pauli channel from the Lindbladian:

$$e^{\mathcal{L}_D T} = 2^{-N} \sum_{j=0}^{4^N-1} e^{-\lambda_j T} |G_j\rangle\langle G_j| \quad (\text{B.6})$$

In this way, we can calculate the fidelity between the noisy output state and the target state as:

$$\langle\langle \rho_g | e^{\mathcal{L}_D T} | \rho_f \rangle\rangle = 2^{-N} \sum_{j=0}^{4^N-1} e^{-\lambda_j T} \langle\langle \rho_g | G_j \rangle\rangle \langle G_j | \rho_f \rangle\rangle \quad (\text{B.7})$$

This is the extreme case in which all γ_k are very different. In practice, there will be a lot of similar γ_k and thus similar λ_j . The Pauli basis with the same λ_j can be grouped together.

Any unitary part \mathcal{L}_H that is block diagonal in the same way as the degenerate subspaces of \mathcal{L}_D will commute with \mathcal{L}_D since \mathcal{L}_D is proportional to identity in these subspaces.

In another word, for \mathcal{L}_H to commute with \mathcal{L}_D , for any given of Pauli basis G_i and G_j we require either $\lambda_i = \lambda_j$, or

$$\begin{aligned}\langle G_i | \mathcal{L}_H | G_j \rangle &= \text{Tr}(G_i \mathcal{L}_H(G_j)) \\ &= -i(\text{Tr}(G_i G_j H) - \text{Tr}(G_j G_i H)) = 0.\end{aligned}$$

A set of sufficient (but not necessary) conditions for the above equation to be true is

$$\left. \begin{array}{l} \lambda_i = \lambda_j \\ \text{or } [G_i, G_j] = 0 \\ \text{or } [G_i, H] = 0 \\ \text{or } [G_j, H] = 0 \\ \text{or } \text{Tr}(G_i G_j H) = 0 \end{array} \right\} \forall i, j \Rightarrow [\mathcal{L}_H, \mathcal{L}_D] = 0 \quad (\text{B.8})$$

B.2.2 Transformation between Pauli transfer matrix and Pauli channels

From the definition of the commutator between Pauli operators, we have:

$$\begin{aligned}\sum_{k=0}^{4^N-1} \eta_{ik} \eta_{jk} &= \sum_{k=0}^{4^N-1} \eta(G_i, G_k) \eta(G_j, G_k) \\ &= \sum_{k=0}^{4^N-1} \eta(G_i G_j, G_k) \\ &= 4^N \delta_{ij}\end{aligned} \quad (\text{B.9})$$

i.e. $2^{-N} \eta_{jk}$ is a orthogonal matrix, it is actually the $2N$ qubit Hadamard matrix with some column/row permutation.

From Eq. (B.3), we know how to decompose a Pauli superoperator into the basis of the Pauli transfer matrix:

$$\mathcal{G}_k = 2^{-N} \sum_{j=0}^{4^N-1} \eta_{jk} |G_j\rangle \langle G_j| \quad (\text{B.10})$$

Using Eq. (B.9), we can also perform the reverse transformation:

$$\begin{aligned} 2^{-N} \sum_{k=0}^{4^N-1} \eta_{ik} \mathcal{G}_k &= \sum_{j=0}^{4^N-1} \left(4^{-N} \sum_{k=0}^{4^N-1} \eta_{ik} \eta_{jk} \right) |G_j\rangle\langle G_j| \\ &= |G_i\rangle\langle G_i| \end{aligned} \quad (\text{B.11})$$

i.e. the orthogonal matrix $2^{-N} \eta_{jk}$ can transform between the pauli transfer matrix basis $\{|G_j\rangle\langle G_j|\}$ and the standard Pauli channel basis $\{\mathcal{G}_k\}$ (or equivalently between $\{2^{-N}|G_j\rangle\langle G_j|\}$ and $\{2^{-N}\mathcal{G}_k\}$).

We can use this to rewrite the resultant Pauli channel from the master's equation in B.6 into the standard form:

$$\begin{aligned} e^{\mathcal{L}_D T} &= 2^{-N} \sum_{j=0}^{4^N-1} e^{-\lambda_j T} |G_j\rangle\langle G_j| \\ &= 2^{-N} \sum_{j=0}^{4^N-1} e^{-\lambda_j T} \left(2^{-N} \sum_{k=0}^{4^N-1} \eta_{jk} \mathcal{G}_k \right) \\ &= 4^{-N} \sum_{k=0}^{4^N-1} \left(\sum_{j=0}^{4^N-1} \eta_{jk} e^{-\lambda_j T} \right) \mathcal{G}_k \end{aligned} \quad (\text{B.12})$$

i.e. the error probability of the k th Pauli operator is

$$p_k = 4^{-N} \sum_{j=0}^{4^N-1} \eta_{jk} e^{-\lambda_j T} \quad (\text{B.13})$$

B.2.3 Example: dephasing noise

For single-qubit dephasing channels, we simply have $\gamma_Z = \gamma$ and $\gamma_I = \gamma_X = \gamma_Y = 0$, and γ here is the dephasing rate we input into our numerical simulation. Using Eq. (B.5), we thus have $\lambda_I = \lambda_Z = 0$ and $\lambda_X = \lambda_Y = \gamma$. Following Eq. (B.6), we have the Pauli transfer matrix representation of the channel:

$$e^{\mathcal{L}_D T} = \frac{1}{2} (|I\rangle\langle I| + |Z\rangle\langle Z|) + \frac{1}{2} e^{-\gamma T} (|X\rangle\langle X| + |Y\rangle\langle Y|) \quad (\text{B.14})$$

Using Eq. (B.13), we have

$$\begin{aligned} p_I &= 4^{-N} (1 + e^{-\gamma T} + e^{-\gamma T} + 1) = \frac{1 + e^{-\gamma T}}{2} \\ p_X &= 4^{-N} (1 + e^{-\gamma T} - e^{-\gamma T} - 1) = 0 \\ p_Y &= 4^{-N} (1 - e^{-\gamma T} + e^{-\gamma T} - 1) = 0 \\ p_Z &= 4^{-N} (1 - e^{-\gamma T} - e^{-\gamma T} + 1) = \frac{1 - e^{-\gamma T}}{2} \end{aligned}$$

Thus the corresponding Pauli channel following Eq. (B.12) is

$$e^{\mathcal{L}_D T} = \frac{1 + e^{-\gamma T}}{2} \mathcal{I} + \frac{1 - e^{-\gamma T}}{2} \mathcal{Z} \quad (\text{B.15})$$

When we have N qubits with individual qubits undergoing dephasing noise, the jump operators in the Master's equation are simply all single-qubit Z operators with the coefficient $\sqrt{\gamma}$, and no other jump operators. Looking back at the gate Hamiltonian in Eq. (3.18), we see that these jump operators commute with all the bases in the Hamiltonian, thus Eq. (B.1) is satisfied and we can study the unitary part and the noise part of the evolution separately. The Pauli transfer matrix of the resultant N -qubit channel from local dephasing is simply given as the tensor product of Eq. (B.14), which is

$$e^{\mathcal{L}_D T} = 2^{-N} \sum_{w=0}^N e^{-w\gamma T} \sum_{j: \text{wt}_X(G_j)=w} |G_j\rangle\langle G_j|$$

where $\text{wt}_X(G_j)$ is the weight of the X string of G_j in the symplectic representation, i.e. the number of qubits that is acted non-trivially by X or Y . The corresponding standard form of the Pauli channel is given by the tensor product of Eq. (B.15).

For example, for two qubits, we have its Pauli transfer matrix as:

$$\begin{aligned} e^{\mathcal{L}_D T} = & \frac{1}{4} (|I\rangle\langle I| + |Z_1\rangle\langle Z_1| + |Z_2\rangle\langle Z_2| + |Z_1Z_2\rangle\langle Z_1Z_2|) \\ & + \frac{e^{-\gamma T}}{4} (|X_1\rangle\langle X_1| + |X_2\rangle\langle X_2| + |Y_1\rangle\langle Y_1| + |Y_2\rangle\langle Y_2| \\ & \quad + |Z_1X_2\rangle\langle Z_1X_2| + |X_1Z_2\rangle\langle X_1Z_2| \\ & \quad + |Y_1Z_2\rangle\langle Y_1Z_2| + |Z_1Y_2\rangle\langle Z_1Y_2|) \\ & + \frac{e^{-2\gamma T}}{4} (|X_1X_2\rangle\langle X_1X_2| + |Y_1Y_2\rangle\langle Y_1Y_2| \\ & \quad + |X_1Y_2\rangle\langle X_1Y_2| + |Y_1X_2\rangle\langle Y_1X_2|) \end{aligned}$$

B.2.4 Group channels

A specific type of Pauli channel we want to discuss here is the group channel [87]. Let $\tilde{\mathbb{F}}$ be a set of independent Pauli operators and $\mathbb{F} = \langle \tilde{\mathbb{F}} \rangle$ to be the group of Pauli operator generated by this set, where all operators and composition here are defined without the irrelevant phase factors (modulo phase). The maximal group

channel for the group of Pauli operator \mathbb{F} is defined as the channel in which all of the elements in the group happen with equal probability:

$$\mathcal{J}_{\mathbb{F}} = \frac{1}{|\mathbb{F}|} \sum_{F_k \in \mathbb{F}} \mathcal{F}_k = \prod_{\tilde{F}_k \in \tilde{\mathbb{F}}} \frac{1 + \tilde{\mathcal{F}}_k}{2}.$$

We can see that when this channels acts on the different Pauli operators, we have:

$$\mathcal{J}_{\mathbb{F}}(G_j) = \begin{cases} G_j & G_j \text{ commute with all elements in } \tilde{\mathbb{F}} \\ 0 & \text{Otherwise} \end{cases} \quad (\text{B.16})$$

Equivalently, we can also write it in the Pauli transfer matrix form as:

$$\mathcal{J}_{\mathbb{F}} = 2^{-N} \sum_{G_j \in \mathbb{G}_{\mathbb{F},+}} |G_j\rangle\langle G_j| \quad (\text{B.17})$$

where $\mathbb{G}_{\mathbb{F},+}$ is the set of Pauli operators that commute with all elements in $\tilde{\mathbb{F}}$ (and thus \mathbb{F}). This is actually a projection operator onto the subspace spanned by $\mathbb{G}_{\mathbb{F},+}$.

A general group channel of error probability p simply means that there is probability p that the maximal group error happens:

$$\mathcal{J}_{\mathbb{F},p} = (1 - p)\mathcal{I} + p\mathcal{J}_{\mathbb{F}}$$

Such group channels arise from the dissipative part of the master equation when the jump operators are $\sqrt{\frac{\gamma}{|\mathbb{F}|}}F_k$ for all elements in the group \mathbb{F} : Hence, in the superoperator form we have:

$$\begin{aligned} \mathcal{L}_D &= \frac{\gamma}{|\mathbb{F}|} \sum_{F_k \in \mathbb{F}} (\mathcal{F} - \mathcal{I}) \\ &= -2^{-N}\gamma \sum_{G_j \notin \mathbb{G}_{\mathbb{F},+}} |G_j\rangle\langle G_j| \end{aligned}$$

Compared to Eq. (B.4), we see that this means

$$\lambda_j = \begin{cases} 0 & G_j \in \mathbb{G}_{\mathbb{F},+} \\ \gamma & G_j \notin \mathbb{G}_{\mathbb{F},+} \end{cases} \quad (\text{B.18})$$

Hence, using Eq. (B.6), the resultant noise channel from the dissipator after time T is given as:

$$\begin{aligned}
& e^{\mathcal{L}_D T} \\
&= 2^{-N} e^{-\gamma T} \sum_{G_j \notin \mathbb{G}_{\mathbb{F},+}} |G_j\rangle\langle G_j| + 2^{-N} \sum_{G_j \in \mathbb{G}_{\mathbb{F},+}} |G_j\rangle\langle G_j| \\
&= 2^{-N} e^{-\gamma T} \sum_j |G_j\rangle\langle G_j| + 2^{-N} (1 - e^{-\gamma T}) \sum_{G_j \in \mathbb{G}_{\mathbb{F},+}} |G_j\rangle\langle G_j| \\
&= e^{-\gamma T} \mathcal{I} + (1 - e^{-\gamma T}) \mathcal{J}_k
\end{aligned} \tag{B.19}$$

i.e. this is a group channel with the maximal group error \mathcal{J}_k occurring with the probability $(1 - e^{-\gamma T})$.

The fidelity between the noisy output state and the target state is:

$$\begin{aligned}
& \langle\langle \rho_g | e^{\mathcal{L}_D T} | \rho_f \rangle\rangle \\
&= 2^{-N} e^{-\gamma T} \sum_{G_j \notin \mathbb{G}_{\mathbb{F},+}} \langle\langle \rho_g | G_j \rangle\rangle \langle G_j | \rho_f \rangle\rangle \\
&\quad + 2^{-N} \sum_{G_j \in \mathbb{G}_{\mathbb{F},+}} \langle\langle \rho_g | G_j \rangle\rangle \langle G_j | \rho_f \rangle\rangle \\
&= e^{-\gamma T} \langle\langle \rho_g | \rho_f \rangle\rangle + 2^{-N} (1 - e^{-\gamma T}) \sum_{G_j \in \mathbb{G}_{\mathbb{F},+}} \langle\langle \rho_g | G_j \rangle\rangle \langle G_j | \rho_f \rangle\rangle
\end{aligned} \tag{B.20}$$

B.2.5 Example: Depolarising channel

For global depolarising channels, the noise group being the entire Pauli group $\mathbb{F} = \mathbb{G}$, thus the commuting basis consists of only the identity operator: $\mathbb{G}_{\mathbb{F},+} = \{I\}$.

Hence, using Eq. (B.18), we have

$$\lambda_0 = 0$$

$$\lambda_j = \gamma \quad \forall j \neq 0$$

Looking back at Eq. (B.8), we have:

$$\left. \begin{array}{l} i = 0 \text{ or } j = 0 \Rightarrow [G_i, G_j] = 0 \\ i \neq 0 \text{ and } j = 0 \Rightarrow \lambda_i = \lambda_j \end{array} \right\} \Rightarrow [\mathcal{L}_H, \mathcal{L}_D] = 0$$

for any \mathcal{L}_H . Thus, the depolarising channel commutes with all unitary parts of the

master equation and the resultant fidelity following Eq. (B.20) is given by:

$$\begin{aligned} & \langle\langle \rho_g | e^{\mathcal{L}_D T} | \rho_f \rangle\rangle \\ &= e^{-\gamma T} \langle\langle \rho_g | \rho_f \rangle\rangle + 2^{-N} (1 - e^{-\gamma T}) \langle\langle \rho_g | I \rangle\rangle \langle\langle I | \rho_f \rangle\rangle \\ &= e^{-\gamma T} \langle\langle \rho_g | \rho_f \rangle\rangle + 2^{-N} (1 - e^{-\gamma T}). \end{aligned}$$

B.2.6 Example: Two-qubit Dipole-Dipole Noise Channel

By dipole-dipole channel, we mean the Pauli channel with the noise group

$$\mathbb{F} = \{I, Z_1 Z_2\}. \quad (\text{B.21})$$

which leads to the jump operators:

$$\begin{aligned} L_0 &= \sqrt{\frac{\gamma}{2}} I \\ L_1 &= \sqrt{\frac{\gamma}{2}} Z_1 Z_2 \end{aligned}$$

Here γ is the decay rate.

Looking back at the gate Hamiltonian in Eq. (3.19), we see that these jump operators commute with all the basis in the Hamiltonian, thus Eq. (B.1) is satisfied and we can study the unitary part and the noise part of the evolution separately. This means the resultant fidelity follows Eq. (B.20). All we need to do is to obtain $\mathbb{G}_{\mathbb{F},+}$, which is the Pauli operators that commute with the noise group \mathbb{F} . It consists of all Pauli operators that have even weights in the X part of the symplectic representation, which is generated by

$$\tilde{\mathbb{G}}_{\mathbb{F},+} = \{Z_1, Z_2, X_1 X_2\} \quad (\text{B.22})$$

B.2.7 The Application of Noise channels for Gate Compilation

When we use the scheme using the Choi state of the channel as noted in Sec. B.3, we need to modify the definition of the noise channels in Sec. B.2.6 and Sec. B.2.3 because the number of qubits of the Choi state is twice the size of the number of

qubits the gates are acted upon. Thus, for example for two-qubit gate compilations, the Choi state will be a four-qubit state.

Since the error channel and the unitary operation are performed on the two original qubits before the bending of the quantum circuit in Fig. B.1, the operations should be acted on either all odd-numbered qubits or all even-numbered qubits of the Choi state. In this paper, we chose the convention of performing operations on all odd-numbered qubits. The target state would be the same except we perform the target gate on all odd-numbered qubits.

This changes the error channels to be four-qubit channels instead of the original two-qubit channels with the identity operators included in between the original operations. For example, the dipole-dipole error channel would be modified to a four-qubit channel as below:

$$\begin{aligned} \mathcal{Z}_{DD}(\rho) = & (1 - \frac{p}{2})I^{\otimes 4}\rho I^{\otimes 4} \\ & + \frac{p}{2}(Z_1 \otimes I \otimes Z_3 \otimes I)\rho(Z_1 \otimes I \otimes Z_3 \otimes I). \end{aligned} \quad (\text{B.23})$$

The evolution of the density matrix would still follow the general arguments given in Sec. B.1 and Sec. B.2.

B.3 Choi States

The Choi-Jamiolkowski isomorphism tells us that, for any completely positive trace-preserving map, \mathcal{E} , there is a corresponding Choi state, $(\mathcal{E} \otimes \mathcal{I})(|\omega\rangle\langle\omega|)$, where $|\omega\rangle$ are Bell pairs. When the map \mathcal{E} is a unitary channel $\mathcal{E}(\rho) = U\rho U^\dagger$, the Choi state becomes a pure state $(U \otimes I)|\omega\rangle$. We used this to map the gate compilation problems to state-to-state transfer problems, such that the initial state is the Bell pairs and the final state is the Choi state of the target gate, i.e. the CZ gate. See Fig. B.1 to see the tensor diagram representation of this scheme. The gate fidelity between two unitary operations, $\tilde{U}(T, \vec{\alpha})$ and U_{target} , is equivalent to the state fidelity between $\tilde{U}|\omega\rangle$ and $U|\omega\rangle$:

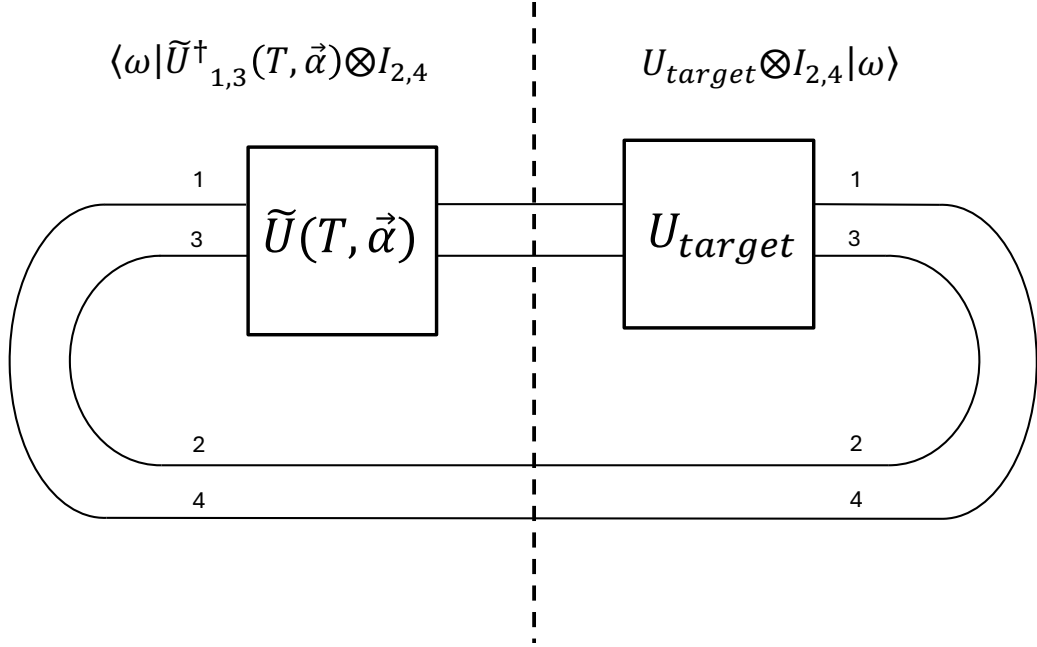


Figure B.1: The tensor network diagram to compare the gate fidelity of two 2-qubit gates, i.e. $\tilde{U}(T, \vec{\alpha})$ and U_{target} , using the Choi state $U_{target} |\omega\rangle$. For 2-qubit gates, $|\omega\rangle$, is two Bell pairs, i.e. $|\Psi^+\rangle \otimes |\Psi^+\rangle$. The subscripts of the gates denote the qubits that the gate is acting on.

$$\begin{aligned} & \frac{1}{2^N} \text{Tr}(\tilde{U}^\dagger(T, \vec{\alpha}) U_{target}) \\ &= \langle \omega | (\tilde{U}^\dagger(T, \vec{\alpha}) \otimes I)(U_{target} \otimes I) |\omega \rangle, \end{aligned}$$

where N is the number of qubits. Since we assume the error channels commuting with the Hamiltonian, we can use the results of Sec. 3.2.2 to obtain the gate fidelity of $\tilde{U}(T, \vec{\alpha})$ and U_{target} subject to error channels (See Sec. B.2.7 for more details).

B.4 Numerical Simulations

B.4.1 Implementation of CRAB and TCRAB

The numerical integration in Eq. (3.4) is performed by first-order Trotterisation with time step size Δt .

In TCRAB, we optimise $F(T, \vec{\alpha})$ over both T and $\vec{\alpha}$. We employed two different optimisation methods: Basin-hopping with L-BFGS-B as its local optimiser and bisection method. In basin-hopping, we optimise T and $\vec{\alpha}$ simultaneously as

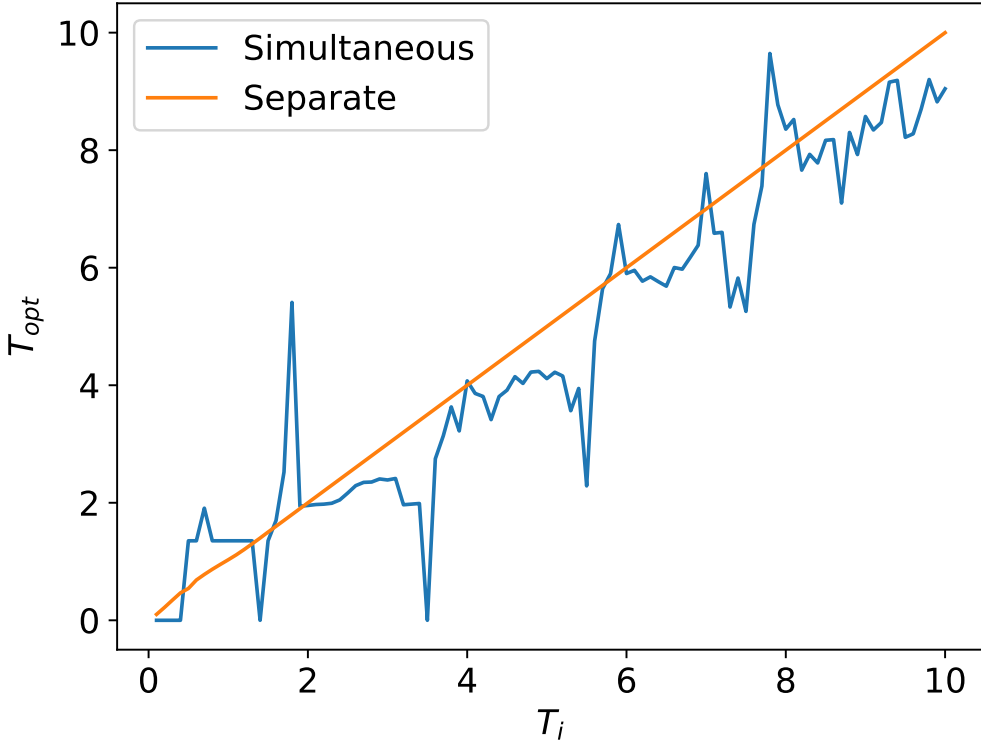


Figure B.2: The optimal time, T_{opt} , obtained by the TCRAB algorithm with simultaneous (blue line) and separate (orange line) optimisation of T and $\vec{\alpha}$, for varying initial guesses of evolution time, T_i . The simultaneous optimisation yields more variation in optimal time than the separate optimisation, and it is more likely to be stuck at the local minima for the separate optimisation. The optimisations were performed for entanglement generation of two capacitively coupled Josephson charge qubits (See Sec. 3.3.1.). Note that we used a local optimiser, L-BFGS-B, with 2000 as its maximum number of function evaluations.

we observed that optimising $\vec{\alpha}$ first and optimising T later resulted in a local minimum that cannot be escaped for the temporal optimisation. We performed both simultaneous and separate optimisation of T and $\vec{\alpha}$ for the entanglement generation of two capacitively coupled Josephson charge qubits (See Sec. 3.3.1.). Fig. B.2 shows the optimal evolution time obtained by L-BFGS-B from the simultaneous and separate optimisation of parameters, $\vec{\alpha}$ and T , with different initial guesses, T_i . For the separate optimisation, the maximum change of evolution time from its initial value was 0.085, and changes of evolution time were in the order of 10^{-3} or below when T_i was bigger than 1.0. In contrast, for the simultaneous optimisation, the change of evolution time was more drastic so the maximum change of evolution time was around 3.61.

Starting from an initial search interval, the bisection method finds the root of a function by iteratively narrowing down the search interval. The function we optimise is the derivative of the optimised infidelity by the evolution time, i.e. $F_{opt}(T)$ in Eq. (3.13). Like in basin-hopping, we used L-BFGS-B for local optimisation at each evolution time when evaluating $F_{opt}(T)$. We used the first-order finite difference approximation to estimate the derivative of $F_{opt}(T)$.

The goal of our simulations is to benchmark the ability of TCRAB to find the optimal parameters, i.e. $\vec{\alpha}_{opt}, T_{opt}$, at the global minimum of the infidelity. Algorithm 1 shows the pseudo-code of the benchmark. We take N_S equal time slices in the range of possible evolution time, i.e. $[0, T_{max}]$: $\mathbb{T}_{init} = \{T_{max}/N_S, 2T_{max}/N_S, \dots, T_{max}\}$. \mathbb{T}_{init} is a set of initial evolution times for each run of CRAB and TCRAB. The frequencies of the truncated basis, $\{\omega\}_{m=1\dots M}$, were taken to be the same for each run of CRAB and TCRAB.

We first run CRAB optimisation on the problem of interest. In particular, we sweep the evolution time, i.e. $T_i \in \mathbb{T}_{init}$ for each CRAB run. We can infer the optimal time by identifying the evolution time of the CRAB run that resulted in the lowest infidelity. In practice, we draw a plot of the infidelity against the evolution time, denoted as plot 1 in Algorithm 1 of Algorithm 1. Since time is not optimised for the runs of CRAB, the optimal time can be inferred from this plot by finding the evolution time where the final infidelity is the lowest. Note that the optimal time identified with CRAB runs is always an element in \mathbb{T}_{init} , and it only serves the purpose of identifying the rough region where the true optimal time will be. The true optimal time will be inferred from TCRAB.

We run TCRAB optimisation on the same problem for both basin-hopping and the bisection method. The results of basin-hopping can vary due to the initial guess of optimal time. As we previously swept the evolution time of CRAB runs, we swept the initial guess of optimal evolution time, $T_i \in \mathbb{T}_{init}$. Note that TCRAB optimises the evolution time, and it is the initial guesses of evolution time, but not the evolution times themselves, that are swept. Then, we identify the optimal evolution time by finding the evolution time of the basin-hopping run that resulted

Algorithm 1 Benchmark of TCRAB

- 1: **for** $i = 1, 2, \dots, N_s$ **do**
 - 2: Select the i th element of \mathbb{T}_{init} to be the time of evolution, i.e. $T_i = T_{\max}/N_s \times i$.
 - 3: Perform the CRAB with the evolution time T_i .
 - 4: Perform the TCRAB with the evolution time T_i as the initial guess of optimal time in Basin-hopping.
 - 5: **end for**
 - 6: Perform TCRAB using the bisection method until convergence.
 - 7: Among N_s runs of TCRAB with different initial guesses of evolution times, T_i , the result with the lowest infidelity becomes the optimal time and the corresponding optimal pulse. Note down the occurrence of this optimal time in plot 3 of Algorithm 1.
 - 8: Using the optimisation results of CRAB and TCRAB, generate three plots:
 - (**Plot 1**): Final infidelity after optimisation vs. initial evolution time, i.e. T_i , using N_s runs of CRAB. In the same plot, draw optimal time and infidelity found by TCRAB with two optimisation methods, i.e. basin-hopping and bisection method.
 - (**Plot 2**): The number of function evaluations vs. initial evolution time, T_i . (Only for CRAB and basin-hopping)
 - (**Plot 3**): Histogram of final optimised time of the basin-hopping runs.
 - 9: Refer to plot 1 of Algorithm 1 to compare the optima found by TCRAB with N_s runs of CRAB. Check if the optimal time and infidelity found by TCRAB roughly match those of the CRAB run that resulted in the lowest infidelity.
-

in the lowest infidelity. Furthermore, we check the fraction of basin-hopping runs that succeeded in obtaining the optimal time by looking at the histogram denoted as plot 3 in the Algorithm 1 of Algorithm 1.

We set the initial search interval of the bisection method to be $[0, T_{\max}]$. We used two stopping conditions: tolerance of the derivative and the length of the interval. If the derivative is smaller than a threshold or if the length of the search interval is smaller than a threshold, the algorithm converges. We compare the optimal time and infidelity with the results of CRAB and basin-hopping.

B.4.2 Hyper-parameters

There is a set of hyper-parameters that the user has to specify to run either CRAB and TCRAB: The number of frequencies, M , the maximum frequency, ω_{max} , and the set of basis frequencies $\vec{\omega}$ selected based on these constraints. The number of frequencies determines the number of basis functions to express the pulse, which is $2 \times M$. For simulations in Sec. 3.3, we chose to use 8 basis functions, i.e. $M = 8$ with an exception to the LMG model in Sec. 3.3.1 where we chose $M = 10$. For simulations in Sec. 3.4, the number of frequencies was varied from 2 to 14. The maximum frequency is set to mimic realistic signal generators that are bandwidth-limited. Note that the frequencies, $\vec{\omega}$ were drawn from a uniform distribution in $[0, \omega_{max}]$. In all simulations, we set the maximum frequency to be 20, i.e. $\omega_{max} = 20$.

There are additional hyper-parameters to run basinhopping[88] with L-BFGS-B[89] as its local optimiser. Among many hyperparameters in the Scipy[104], we varied the following with the corresponding argument names in brackets: the maximum number of function evaluations (*maxfun*), lower and upper bounds of the optimisation parameters to define the search space of T and $\vec{\alpha}$ (*bounds*), the step size in numerical differentiation (*eps*), the tolerance levels for the stopping criteria based on the values of the function and gradient (*ftol*, *gtol*).

The maximum number of function evaluations was set to be 10000 for both CRAB and TCRAB. The search space of each component of $\vec{\alpha}$ was bounded by -100 and 100 such that $\vec{\alpha} \in [-100, 100]^{\otimes M}$, for both CRAB and TCRAB, and the search space of T was bounded by $[0, T_{max}]$, as noted in Sec. 3.2. We fixed the upper bound of the search space, T_{max} , to be 10 for all simulations. The step size was chosen as 10^{-6} . The tolerance levels, i.e. *ftol* and *gtol*, were 10^{-8} and 10^{-12} . Other parameters were left as the default values of the implementation of L-BFGS-B in Scipy[104].

There are three additional hyper-parameters to run the bisection method: the step size in time used to evaluate the derivative of $F_{opt}(T)$, the tolerance level for two stopping conditions, i.e. the absolute value of $\dot{F}_{opt}(T)$ and the length of search interval. For the entanglement generation using Josephson charge qubits in Sec. 3.3.1, the step size and the two tolerance levels were $1e-3$, $1e-6$, $1e-6$,

respectively. For the rest of the problems, the step size and the two tolerance levels were $1e-4$, $1e-6$, $1e-4$, respectively.

There are hyper-parameters of the state vector simulation. The number of time steps, N_t , was chosen to be 300. Furthermore, we chose decay factors such that the decaying effect is visible in the search space. The step size of time chosen to sweep the search space was 0.1 such that $\mathcal{I}_{100} = \{0.1, 0.2, \dots, 10\}$.

B.5 Additional Numerics

In Figs. B.3 to B.6, we present the additional numerics we perform alongside the results in Sec. 3.3.

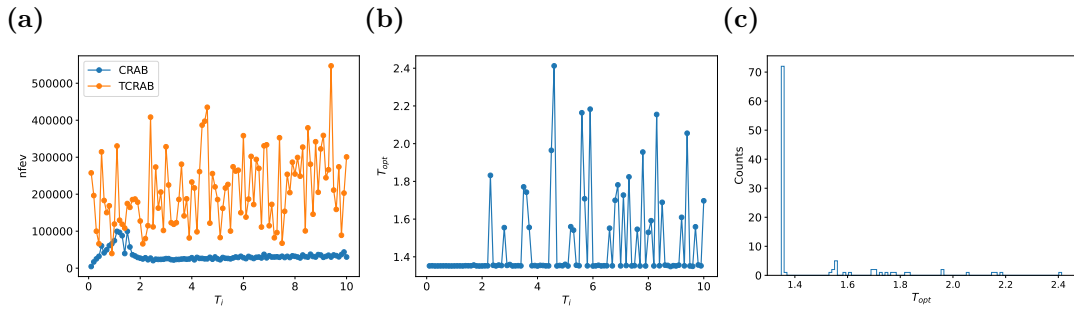


Figure B.3: Results of the entanglement generation of two capacitively coupled Josephson charge qubits are shown: (a) The number of function evaluations, n_{fev} , to reach the convergence, and (b) The resulting optimal time, T_{opt} , for each initial evolution time (CRAB)/ initial guess of optimal time (TCRAB), T_i . (c) The distribution of optimal time, T_{opt} , found by the TCRAB scheme.

B.6 Oscillation of Optimised Fidelity

The Liouville superoperator of the unitary part can be explicitly split into a term \mathcal{L}_0 that corresponds to the drift Hamiltonian H_0 in Eq. (3.1) and thus is independent of the evolution time t and the control parameters $\vec{\alpha}$, and another term \mathcal{L}_C that corresponds to the rest of the controlled Hamiltonian:

$$\mathcal{L}_H(\vec{\alpha}, t) = \mathcal{L}_0 + \mathcal{L}_C(\vec{\alpha}, t).$$

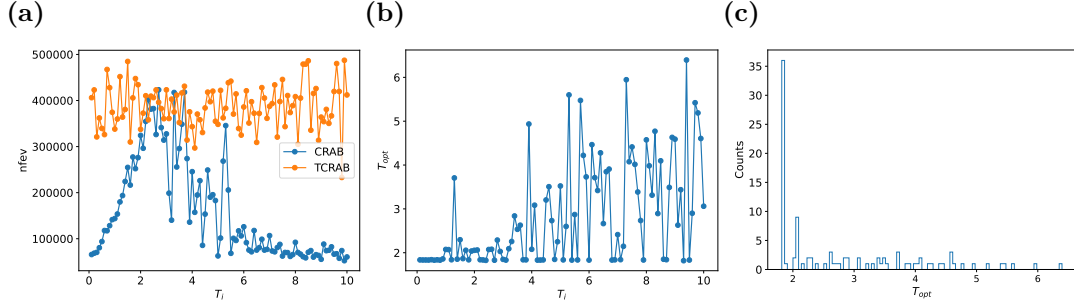


Figure B.4: Results of the state-to-state transfer from the ground state of paramagnetic phase to a ground state of ferromagnetic phase are shown: (a) The number of function evaluations, n_{fev} , to reach the convergence, and (b) The resulting optimal time, T_{opt} , for each initial evolution time (CRAB)/ initial guess of optimal time (TCRAB), T_i . (c) The distribution of optimal time, T_{opt} , found by the TCRAB scheme.

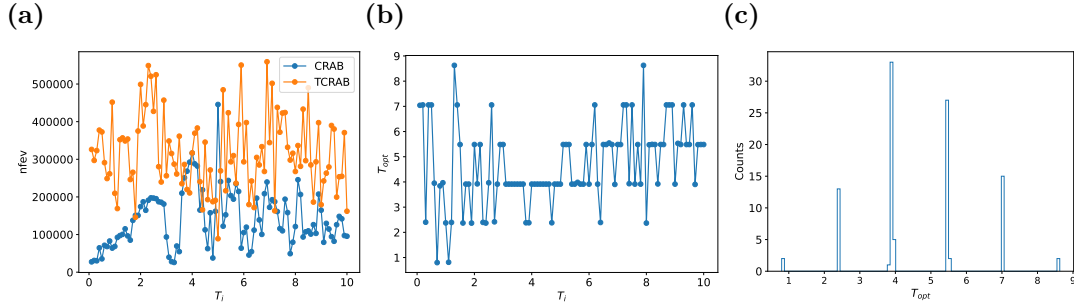


Figure B.5: Results of the gate compilation of CZ for $\Omega \ll J$ are shown: (a) The number of function evaluations, n_{fev} , to reach the convergence, and (b) The resulting optimal time, T_{opt} , for each initial evolution time (CRAB)/ initial guess of optimal time (TCRAB), T_i . (c) The distribution of optimal time, T_{opt} , found by the TCRAB scheme.

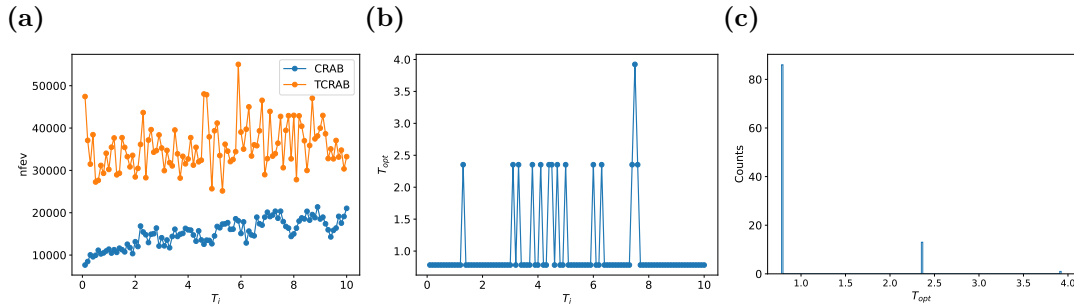


Figure B.6: Results of the gate compilation of CZ for $\Omega \gg J$ are shown: (a) The number of function evaluations, n_{fev} , to reach the convergence, and (b) The resulting optimal time, T_{opt} , for each initial evolution time (CRAB)/ initial guess of optimal time (TCRAB), T_i . (c) The distribution of optimal time, T_{opt} , found by the TCRAB scheme.

When the drift Hamiltonian H_0 in Eq. (3.1) commutes with all of the controlled Hamiltonian, then the evolution due to \mathcal{L}_0 and $\mathcal{L}_C(\vec{\alpha}, t)$ becomes separable and the final state can reach under the given Hamiltonian in the absence of noise can thus be written as:

$$|\rho_f(T, \vec{\alpha})\rangle\rangle = e^{\mathcal{L}_0 T} |\rho_c(T, \vec{\alpha})\rangle\rangle \quad (\text{B.24})$$

where ρ_c is the state obtained under the evolution caused by $\mathcal{L}_C(\vec{\alpha}, t)$, which is purely due to the control Hamiltonian, and $e^{\mathcal{L}_0 T}$ is the action due to purely the drift Hamiltonian.

In this way, the optimal fidelity for state-to-state transfer with evolution time T can be written as:

$$\begin{aligned} F_{\text{opt}}(T) &= F(T, \vec{\alpha}_T) = \langle\langle \rho_{g,\text{noi}}(T) | \rho_f(T, \vec{\alpha}_T) \rangle\rangle \\ &= \langle\langle \rho_{g,\text{noi}}(T) | e^{\mathcal{L}_0 T} | \rho_c(T, \vec{\alpha}_T) \rangle\rangle \\ &= \text{Tr}\left(\rho_{g,\text{noi}}(T) e^{-iH_0 T} \rho_c(T, \vec{\alpha}_T) e^{iH_0 T}\right) \end{aligned}$$

From here on, let us suppose H_0 is proportional to an involution operator $H_0 = \omega K_0$, i.e. it squares to I , which includes the Pauli operators. We then have $e^{\pm iH_0 T} = I \cos(\omega T) \pm iK_0 \sin(\omega T)$ and

$$\begin{aligned} F_{\text{opt}}(T) &= \text{Tr}(\rho_{g,\text{noi}} \rho_c) \cos^2(\omega T) + \text{Tr}(\rho_{g,\text{noi}} K_0 \rho_c K_0) \sin^2(\omega T) \\ &\quad - i[\text{Tr}(\rho_{g,\text{noi}} K_0 \rho_c) - \text{Tr}(\rho_{g,\text{noi}} \rho_c K_0)] \sin(\omega T) \cos(\omega T) \\ &= a(T) + b(T) \cos(2\omega T) + c(T) \sin(2\omega T) \end{aligned}$$

with

$$\begin{aligned} a(T) &= \frac{1}{2} (\text{Tr}(\rho_{g,\text{noi}} \rho_c) + \text{Tr}(\rho_{g,\text{noi}} K_0 \rho_c K_0)) \\ b(T) &= \frac{1}{2} (\text{Tr}(\rho_{g,\text{noi}} \rho_c) - \text{Tr}(\rho_{g,\text{noi}} K_0 \rho_c K_0)) \\ c(T) &= -\frac{i}{2} [\text{Tr}(\rho_{g,\text{noi}} K_0 \rho_c) - \text{Tr}(\rho_{g,\text{noi}} \rho_c K_0)] \end{aligned}$$

For general H_0 , we can still have oscillation, but more Fourier components will be involved [105].

However, commutation does not always mean there will be oscillation. For example, the control Hamiltonian can contain all of the basis of the drift Hamiltonian, which can then compensate for the effect of the drift Hamiltonian.

B.7 Identity Test

As described in Sec. 3.4, one can perform the identity test: The test to check whether the evolution operator can be the same as the identity operator with the given drift and control Hamiltonian, i.e. $U(T, \vec{\alpha}) = \mathcal{I}$. The identity test checks the maximum capability of the control Hamiltonian to compensate for the drift term within the evolution operator, which causes oscillation in the infidelity. For example, if the infidelity of the identity test is 0.4, this is the maximum capability of the control Hamiltonian as the control Hamiltonian cannot further suppress the drift term and make the infidelity lower.

For a state-to-state transfer problem, the identity test reduces to the compilation of identity for the given initial state, i.e. $|\langle \psi_i | U(T, \vec{\alpha}) | \psi_i \rangle|^2 = 1$. This shows that the time evolution operator, $U(T, \vec{\alpha})$, successfully acts like an identity operator for $|\psi_i\rangle$, but not necessarily for all states. In other words, for the given initial state, $|\psi_i\rangle$, the control Hamiltonian can fully suppress the oscillation by the drift term.

Note that this is a rough test of such capability, but this doesn't guarantee better performance in a specific problem, e.g. compilation of the CZ gate. This is because, depending on the target, one may need some effect of the drift term in addition to a specific form of the control pulse, which wouldn't be possible to obtain with the given set of basis functions and evolution time.

Fig. B.7 shows the results of the identity test for the four systems in Sec. 3.3: (a) Two capacitively coupled charge qubits, (b) the LMG model, and two spin qubits in Silicon quantum dots of two regimes: (c) $\Omega \ll J$ and (d) $\Omega \gg J$.

The capability to suppress the effect of the drift term is determined by the commutation relation of the drift term and the control Hamiltonian. For a state-to-state transfer problem, this capability also depends on the initial state and the target state.

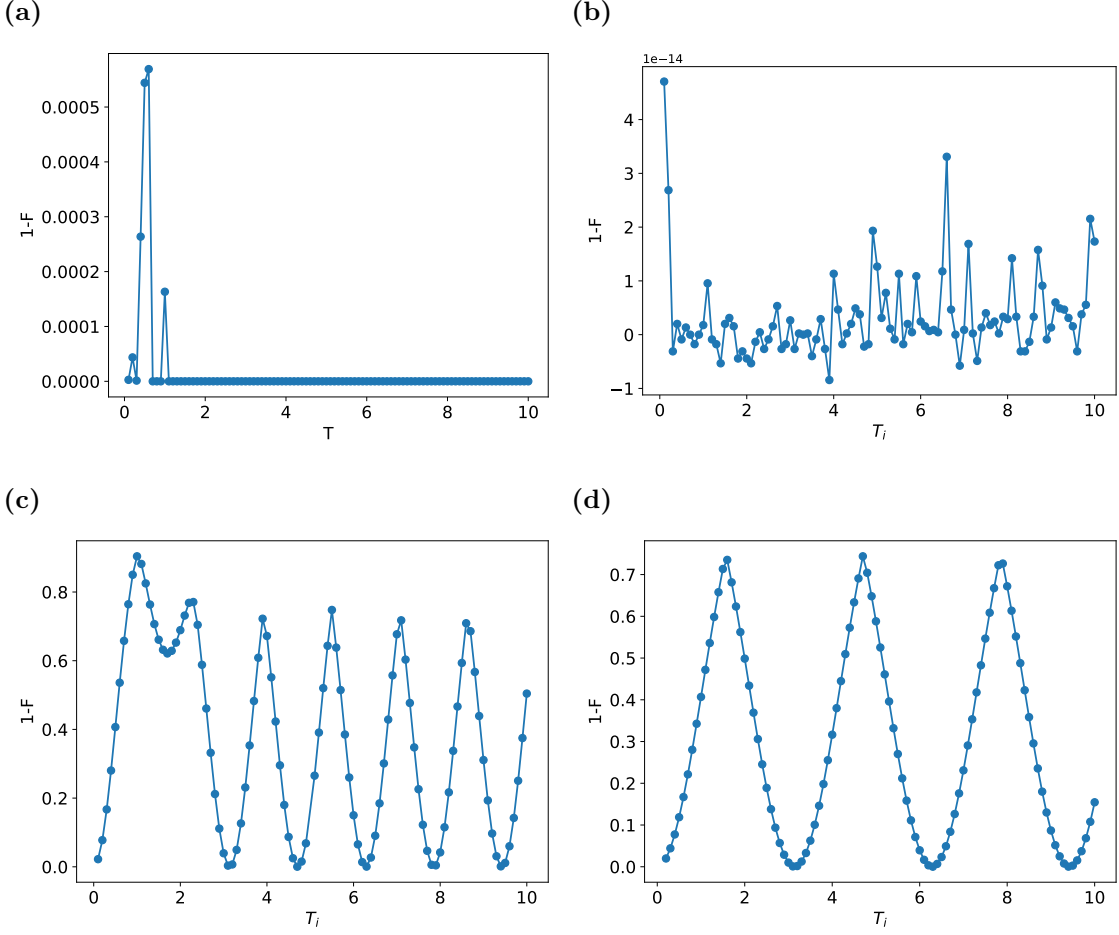


Figure B.7: Results of the identity test for (a) two capacitively coupled Josephson charge qubits, (b) the LMG model, and two spin qubits in Silicon quantum dots in the regime of (c) $\Omega \ll J$ and (d) $\Omega \gg J$. For all four cases, we performed CRAB with varying T_i for the gate compilation of the identity gate using the given drift and control Hamiltonians. For a state-to-state transfer problem, we only need to show the compilation of identity for the given initial state. Thus, we used the initial states specified in Sec. 3.3.1 and set the target states the same as the initial states. On the other hand, we used the Choi state scheme as explained for the gate compilation Sec. B.3.

The identity test for Josephson charge qubits in Fig. B.7a exhibits some peaks for low evolution times. While the control Hamiltonian, $\sigma_1^z \sigma_2^z$, anti-commutes with some parts of the drift term, i.e. σ_1^x and σ_2^x , it commutes with the other half of the drift terms, i.e σ_1^z and σ_2^z . The effect of commuting drift terms can still be compensated with the help of the anti-commuting drift Hamiltonian at the expense of longer evolution times. Nevertheless, The magnitudes of peaks are so small compared to the effects of decay and control terms, such that the cost

function in Fig. 3.1a doesn't exhibit oscillation for short evolution time for the given initial and target states, i.e. $|00\rangle$.

For the LMG model in Fig. B.7b, the infidelity is in the order of 10^{-14} for all evolution times, suggesting that the control pulse can successfully suppress the contributions from the drift term if necessary for the given initial state, $|000\rangle$. Thus, the cost function in Fig. 3.1b doesn't exhibit the oscillation.

Finally, the control Hamiltonians for spin qubits in Silicon quantum dots, i.e. SWAP for $\Omega \ll J$ and $Z_1 \otimes Z_2$, commute with the drift term, $(\Delta E_1 Z_1 + \Delta E_2 Z_2)/2$, which is a sum of two single-qubit Z gates. Thus, there is no way for the control Hamiltonians to compensate for the oscillation due to the drift Hamiltonian, and the cost functions in Fig. 3.1d and Fig. 3.1c exhibit oscillations.

The first kind of intellectual and artistic personality belongs to the hedgehogs, the second to the foxes ...

— Sir Isaiah Berlin [berlin_hedgehog_2013]

Bibliography

- [1] Veit Langrock et al. “Blueprint of a Scalable Spin Qubit Shuttle Device for Coherent Mid-Range Qubit Transfer in Disordered Si/SiGe/SiO₂”. In: *PRX Quantum* 4 (2 2023), p. 020305. URL: <https://link.aps.org/doi/10.1103/PRXQuantum.4.020305>.
- [2] Guido Burkard et al. “Semiconductor spin qubits”. In: *Rev. Mod. Phys.* 95 (2 2023), p. 025003. URL: <https://link.aps.org/doi/10.1103/RevModPhys.95.025003>.
- [3] David Young. “Iterative Methods for Solving Partial Difference Equations of Elliptic Type”. In: *Transactions of the American Mathematical Society* 76.1 (1954), pp. 92–111.
- [4] Stanley P. Frankel. “Convergence Rates of Iterative Treatments of Partial Differential Equations”. In: *Mathematical Tables and Other Aids to Computation* 4.30 (1950), pp. 65–75. URL: <http://www.jstor.org/stable/2002770> (visited on 03/07/2024).
- [5] R. Glowinski, S.J. Osher, and W. Yin. *Splitting Methods in Communication, Imaging, Science, and Engineering*. Scientific Computation. Switzerland: Springer International Publishing, 2017. URL: <https://books.google.co.uk/books?id=KHcTDAEACAAJ>.
- [6] Gilbert Strang. “On the Construction and Comparison of Difference Schemes”. In: *SIAM Journal on Numerical Analysis* 5.3 (1968), pp. 506–517. URL: <https://doi.org/10.1137/0705041>.
- [7] Gilbert Strang. *Essays in Linear Algebra*. Philadelphia, PA: Wellesley-Cambridge Press, 2012. URL: <https://pubs.siam.org/doi/abs/10.1137/1.9780980232769>.
- [8] C. H. Yang et al. “Spin-valley lifetimes in a silicon quantum dot with tunable valley splitting”. In: *Nature Communications* 4.1 (June 2013). URL: <http://dx.doi.org/10.1038/ncomms3069>.
- [9] M. Veldhorst et al. “Spin-orbit coupling and operation of multivalley spin qubits”. In: *Phys. Rev. B* 92 (2015), p. 201401. URL: <https://link.aps.org/doi/10.1103/PhysRevB.92.201401>.
- [10] Rusko Ruskov et al. “Electron g-factor of valley states in realistic silicon quantum dots”. In: *Phys. Rev. B* 98 (24 2018), p. 245424. URL: <https://link.aps.org/doi/10.1103/PhysRevB.98.245424>.
- [11] C. Euaruksakul et al. “Influence of Strain on the Conduction Band Structure of Strained Silicon Nanomembranes”. In: *Phys. Rev. Lett.* 101 (14 2008), p. 147403. URL: <https://link.aps.org/doi/10.1103/PhysRevLett.101.147403>.

- [12] E. Kawakami et al. “Electrical control of a long-lived spin qubit in a Si/SiGe quantum dot”. In: *Nature Nanotechnology* 9.9 (Aug. 2014), 666–670. URL: <http://dx.doi.org/10.1038/nnano.2014.153>.
- [13] J B Johnson. “Thermal Agitation of Electricity in Conductors”. In: *Nature* 119.2984 (Jan. 1927), pp. 50–51. URL: <https://doi.org/10.1038/119050c0>.
- [14] H. Nyquist. “Thermal Agitation of Electric Charge in Conductors”. In: *Phys. Rev.* 32 (1 1928), pp. 110–113. URL: <https://link.aps.org/doi/10.1103/PhysRev.32.110>.
- [15] Laszlo B Kish, Gunnar A Niklasson, and Claes G Granqvist. “Zero-point term and quantum effects in the Johnson noise of resistors: a critical appraisal”. In: *Journal of Statistical Mechanics: Theory and Experiment* 2016.5 (May 2016), p. 054006. URL: <http://dx.doi.org/10.1088/1742-5468/2016/05/054006>.
- [16] Peihao Huang and Xuedong Hu. “Spin qubit relaxation in a moving quantum dot”. In: *Physical Review B* 88.7 (Aug. 2013). URL: <http://dx.doi.org/10.1103/PhysRevB.88.075301>.
- [17] Brandon Buonacorsi et al. “Optimizing lateral quantum dot geometries for reduced exchange noise”. In: *arXiv* (2020). arXiv: 2012.10512.
- [18] Jan A. Krzywda. “Decoherence of electron spin qubit during transfer between two semiconductor quantum dots at low magnetic fields”. In: *Phys. Rev. B* 111 (11 2025), p. 115305. URL: <https://link.aps.org/doi/10.1103/PhysRevB.111.115305>.
- [19] Christiane P. Koch et al. “Quantum optimal control in quantum technologies. Strategic report on current status, visions and goals for research in Europe”. In: *EPJ Quantum Technology* 9.1 (11 July 2022), p. 115305. URL: <http://dx.doi.org/10.1140/epjqt/s40507-022-00138-x>.
- [20] M. M. Müller et al. “Room-temperature Rydberg single-photon source”. In: *Phys. Rev. A* 87 (5 2013), p. 053412. URL: <https://link.aps.org/doi/10.1103/PhysRevA.87.053412>.
- [21] Jonathon Brown, Mauro Paternostro, and Alessandro Ferraro. “Optimal quantum control via genetic algorithms for quantum state engineering in driven-resonator mediated networks”. In: *Quantum Science and Technology* 8.2 (11 2023), p. 025004. URL: <https://dx.doi.org/10.1088/2058-9565/acb2f2>.
- [22] Paraj Titum et al. “Optimal control for quantum detectors”. In: *npj Quantum Information* 7.1 (11 Mar. 2021), p. 115305. URL: <http://dx.doi.org/10.1038/s41534-021-00383-5>.
- [23] John F. Barry et al. “Sensitivity optimization for NV-diamond magnetometry”. In: *Rev. Mod. Phys.* 92 (1 2020), p. 015004. URL: <https://link.aps.org/doi/10.1103/RevModPhys.92.015004>.
- [24] Xikun Li. *Optimal control of quantum state preparation and entanglement creation in two-qubit quantum system with bounded amplitude*. 2023. arXiv: 2211.09323 [quant-ph]. URL: <https://arxiv.org/abs/2211.09323>.

- [25] Stefanie Günther, N. Anders Petersson, and Jonathan L. DuBois. “Quantum optimal control for pure-state preparation using one initial state”. In: *AVS Quantum Science* 3.4 (11 Dec. 2021), p. 043801. URL: <http://dx.doi.org/10.1116/5.0060262>.
- [26] Vadim N. Petruhanov and Alexander N. Pechen. “Optimal control for state preparation in two-qubit open quantum systems driven by coherent and incoherent controls via GRAPE approach”. In: *International Journal of Modern Physics A* 37.20n21 (11 July 2022), p. 115305. URL: <http://dx.doi.org/10.1142/S0217751X22430175>.
- [27] Prabin Parajuli, Anuvetha Govindarajan, and Lin Tian. “State preparation in a Jaynes-Cummings lattice with quantum optimal control”. In: *Scientific Reports* 13.1 (11 Nov. 2023), p. 19924. URL: <https://link.aps.org/doi/10.1103/PhysRevB.111.115305>.
- [28] Liam J. Bond, Arghavan Safavi-Naini, and Jiří Minář. “Fast Quantum State Preparation and Bath Dynamics Using Non-Gaussian Variational Ansatz and Quantum Optimal Control”. In: *Physical Review Letters* 132.17 (11 Apr. 2024), p. 115305. URL: <http://dx.doi.org/10.1103/PhysRevLett.132.170401>.
- [29] Jack Y. Araz et al. “State preparation of lattice field theories using quantum optimal control”. In: *Physical Review D* 111.3 (11 Feb. 2025), p. 115305. URL: <http://dx.doi.org/10.1103/PhysRevD.111.034506>.
- [30] Andrew Litteken et al. “Dancing the Quantum Waltz: Compiling Three-Qubit Gates on Four Level Architectures”. In: *Proceedings of the 50th Annual International Symposium on Computer Architecture*. Vol. 111. ISCA ’23. ACM, June 2023, 1–14. URL: <http://dx.doi.org/10.1145/3579371.3589106>.
- [31] Lennart Maximilian Seifert et al. “Exploring ququart computation on a transmon using optimal control”. In: *Physical Review A* 108.6 (11 Dec. 2023), p. 115305. URL: <http://dx.doi.org/10.1103/PhysRevA.108.062609>.
- [32] Stefanie Günther and N. Anders Petersson. *A practical approach to determine minimal quantum gate durations using amplitude-bounded quantum controls*. 2023. arXiv: 2307.13168 [quant-ph]. URL: <https://arxiv.org/abs/2307.13168>.
- [33] Yujin Cho et al. “Direct pulse-level compilation of arbitrary quantum logic gates on superconducting qutrits”. In: *Physical Review Applied* 22.3 (11 Sept. 2024), p. 115305. URL: <http://dx.doi.org/10.1103/PhysRevApplied.22.034066>.
- [34] Navin Khaneja et al. “Optimal control of coupled spin dynamics: design of NMR pulse sequences by gradient ascent algorithms.” In: *Journal of magnetic resonance* 172 2 (11 2005), pp. 296–305. URL: <https://link.aps.org/doi/10.1103/PhysRevB.111.115305>.
- [35] V. F. Krotov and I. N. Fel'dman. “An iterative method for solving optimal-control problems.” In: *Engrg. Cybernetics* 21 (11 1983), p. 123. URL: <https://link.aps.org/doi/10.1103/PhysRevB.111.115305>.
- [36] Matthias M Müller et al. “One decade of quantum optimal control in the chopped random basis”. In: *Reports on Progress in Physics* 85.7 (11 June 2022), p. 076001. URL: <http://dx.doi.org/10.1088/1361-6633/ac723c>.

- [37] Re-Bing Wu et al. “Learning robust and high-precision quantum controls”. In: *Physical Review A* 99.4 (11 2019), p. 115305. URL: <https://doi.org/10.1103%2Fphysreva.99.042327>.
- [38] Y.X. Zeng et al. “Quantum control based on machine learning in an open quantum system”. In: *Physics Letters A* 384.35 (11 2020), p. 126886. URL: <https://www.sciencedirect.com/science/article/pii/S0375960120307532>.
- [39] Tangyou Huang et al. “Machine-Learning-Assisted Quantum Control in a Random Environment”. In: *Phys. Rev. Appl.* 17 (2 2022), p. 024040. URL: <https://link.aps.org/doi/10.1103/PhysRevApplied.17.024040>.
- [40] Frank Schäfer et al. “A differentiable programming method for quantum control”. In: *Machine Learning: Science and Technology* 1.3 (11 2020), p. 035009. URL: <https://doi.org/10.1088%2F2632-2153%2Fab9802>.
- [41] M. Ostaszewski et al. “Approximation of quantum control correction scheme using deep neural networks”. In: *Quantum Information Processing* 18.5 (11 2019), p. 115305. URL: <https://doi.org/10.1007%2Fs11128-019-2240-7>.
- [42] Elija Perrier, Dacheng Tao, and Chris Ferrie. “Quantum geometric machine learning for quantum circuits and control”. In: *New Journal of Physics* 22.10 (11 2020), p. 103056. URL: <https://doi.org/10.1088%2F1367-2630%2Fabbf6b>.
- [43] Marin Bukov et al. “Reinforcement Learning in Different Phases of Quantum Control”. In: *Phys. Rev. X* 8 (3 2018), p. 031086. URL: <https://link.aps.org/doi/10.1103/PhysRevX.8.031086>.
- [44] Zheng An and D. L. Zhou. “Deep reinforcement learning for quantum gate control”. In: *Europhysics Letters* 126.6 (11 2019), p. 60002. URL: <https://dx.doi.org/10.1209/0295-5075/126/60002>.
- [45] Xiao-Ming Zhang et al. “When does reinforcement learning stand out in quantum control? A comparative study on state preparation”. In: *npj Quantum Information* 5.1 (11 2019), p. 85. URL: <https://doi.org/10.1038/s41534-019-0201-8>.
- [46] Yuval Baum et al. “Experimental Deep Reinforcement Learning for Error-Robust Gate-Set Design on a Superconducting Quantum Computer”. In: *PRX Quantum* 2 (4 2021), p. 040324. URL: <https://link.aps.org/doi/10.1103/PRXQuantum.2.040324>.
- [47] Murphy Yuezhen Niu et al. *Universal Quantum Control through Deep Reinforcement Learning*. 2018. arXiv: 1803.01857 [quant-ph]. URL: <https://link.aps.org/doi/10.1103/PhysRevB.111.115305>.
- [48] Zheng An et al. “Quantum optimal control of multilevel dissipative quantum systems with reinforcement learning”. In: *Phys. Rev. A* 103 (1 2021), p. 012404. URL: <https://link.aps.org/doi/10.1103/PhysRevA.103.012404>.
- [49] Philip Andreasson et al. “Quantum error correction for the toric code using deep reinforcement learning”. In: *Quantum* 3 (11 2019), p. 183. URL: <https://doi.org/10.22331%2Fq-2019-09-02-183>.
- [50] Jonas Schuff, Lukas J Fiderer, and Daniel Braun. “Improving the dynamics of quantum sensors with reinforcement learning”. In: *New Journal of Physics* 22.3 (11 2020), p. 035001. URL: <https://dx.doi.org/10.1088/1367-2630/ab6f1f>.

- [51] Tangyou Huang et al. “Time-optimal control of driven oscillators by variational circuit learning”. In: *Phys. Rev. Res.* 5 (2 2023), p. 023173. URL: <https://link.aps.org/doi/10.1103/PhysRevResearch.5.023173>.
- [52] Yuanyang Zhou et al. *Variational quantum compiling for three-qubit gates design in quantum dots*. 2024. arXiv: 2412.06276 [quant-ph]. URL: <https://arxiv.org/abs/2412.06276>.
- [53] V N Petruhanov and A N Pechen. “GRAPE optimization for open quantum systems with time-dependent decoherence rates driven by coherent and incoherent controls”. In: *Journal of Physics A: Mathematical and Theoretical* 56.30 (11 2023), p. 305303. URL: <https://dx.doi.org/10.1088/1751-8121/ace13f>.
- [54] Mohamed Abdelhafez, David I. Schuster, and Jens Koch. “Gradient-based optimal control of open quantum systems using quantum trajectories and automatic differentiation”. In: *Physical Review A* 99.5 (11 May 2019), p. 115305. URL: <http://dx.doi.org/10.1103/PhysRevA.99.052327>.
- [55] Hailan Ma, Chunlin Chen, and Daoyi Dong. “Differential Evolution with Equally-Mixed Strategies for Robust Control of Open Quantum Systems”. In: *2015 IEEE International Conference on Systems, Man, and Cybernetics, Kowloon Tong, Hong Kong, October 9-12, 2015*. Vol. 111. IEEE, 2015, pp. 2055–2060. URL: <http://dx.doi.org/10.1109/SMC.2015.359>.
- [56] Wenhao He et al. *Efficient Optimal Control of Open Quantum Systems*. 2024. arXiv: 2405.19245 [quant-ph]. URL: <https://link.aps.org/doi/10.1103/PhysRevB.111.115305>.
- [57] Ugo Boscain et al. “Minimal time trajectories for two-level quantum systems with two bounded controls”. In: *Journal of Mathematical Physics* 55.6 (11 June 2014), p. 062106. eprint: https://pubs.aip.org/aip/jmp/article-pdf/doi/10.1063/1.4882158/13907544/062106_1_online.pdf. URL: <https://doi.org/10.1063/1.4882158>.
- [58] Francesca Albertini and Domenico D’Alessandro. “Minimum time optimal synthesis for two level quantum systems”. In: *Journal of Mathematical Physics* 56.1 (11 Jan. 2015), p. 012106. eprint: https://pubs.aip.org/aip/jmp/article-pdf/doi/10.1063/1.4906137/15892395/012106_1_online.pdf. URL: <https://doi.org/10.1063/1.4906137>.
- [59] H Jirari. “Implementation of one-qubit gates using optimal control theory for a dissipative system”. In: *The European Physical Journal B* 94.10 (11 Oct. 2021), p. 217. URL: <https://link.aps.org/doi/10.1103/PhysRevB.111.115305>.
- [60] U. Boscain, M. Sigalotti, and D. Sugny. “Introduction to the Pontryagin Maximum Principle for Quantum Optimal Control”. In: *PRX Quantum* 2 (3 2021), p. 030203. URL: <https://link.aps.org/doi/10.1103/PRXQuantum.2.030203>.
- [61] Fahimeh Naghdi, Mohammad Ali Jafarizadeh, and Mohammad Reza Bazrafkan. “Time optimal control for spin I=1”. In: *Physics Letters A* 448 (11 2022), p. 128297. URL: <https://www.sciencedirect.com/science/article/pii/S0375960122003796>.

- [62] Chungwei Lin, Yanting Ma, and Dries Sels. “Application of Pontryagin’s maximum principle to quantum metrology in dissipative systems”. In: *Phys. Rev. A* 105 (4 2022), p. 042621. URL: <https://link.aps.org/doi/10.1103/PhysRevA.105.042621>.
- [63] Dionisis Stefanatos and Emmanuel Paspalakis. “Efficient generation of the triplet Bell state between coupled spins using transitionless quantum driving and optimal control”. In: *Phys. Rev. A* 99 (2 2019), p. 022327. URL: <https://link.aps.org/doi/10.1103/PhysRevA.99.022327>.
- [64] Mohammad Ali Jafarizadeh, Fahimeh Naghdi, and Mohammad Reza Bazrafkan. “Time optimal realization of two-qubit entangler”. In: *The European Physical Journal Plus* 137.6 (11 June 2022), p. 720. URL: <https://link.aps.org/doi/10.1103/PhysRevB.111.115305>.
- [65] Alberto Carlini et al. “Time-Optimal Quantum Evolution”. In: *Physical Review Letters* 96.6 (11 Feb. 2006), p. 115305. URL: <http://dx.doi.org/10.1103/PhysRevLett.96.060503>.
- [66] Alberto Carlini et al. “Time-optimal unitary operations”. In: *Phys. Rev. A* 75 (4 2007), p. 042308. URL: <https://link.aps.org/doi/10.1103/PhysRevA.75.042308>.
- [67] Tatsuhiko Koike. “Quantum brachistochrone”. In: *Philosophical Transactions of the Royal Society A: Mathematical, Physical and Engineering Sciences* 380.2239 (11 2022), p. 20210273. eprint: <https://royalsocietypublishing.org/doi/pdf/10.1098/rsta.2021.0273>. URL: <https://royalsocietypublishing.org/doi/abs/10.1098/rsta.2021.0273>.
- [68] Fu-Quan Dou, Min-Peng Han, and Chuan-Cun Shu. “Quantum Speed Limit under Brachistochrone Evolution”. In: *Phys. Rev. Appl.* 20 (1 2023), p. 014031. URL: <https://link.aps.org/doi/10.1103/PhysRevApplied.20.014031>.
- [69] Peter Morrison. *Time Optimal Qubit Computer*. 2023. arXiv: 2306.01223 [quant-ph]. URL: <https://arxiv.org/abs/2306.01223>.
- [70] Casey Jameson et al. “Time optimal quantum state transfer in a fully-connected quantum computer”. In: *Quantum Science and Technology* 9.1 (11 2023), p. 015014. URL: <https://dx.doi.org/10.1088/2058-9565/ad0770>.
- [71] Jun Zhang et al. “Geometric theory of nonlocal two-qubit operations”. In: *Phys. Rev. A* 67 (4 2003), p. 042313. URL: <https://link.aps.org/doi/10.1103/PhysRevA.67.042313>.
- [72] Chengming Tan et al. *Geometric Optimization of Quantum Control with Minimum Cost*. 2024. arXiv: 2409.14540 [quant-ph]. URL: <https://arxiv.org/abs/2409.14540>.
- [73] Ho Lun Tang et al. “Designing Globally Time-Optimal Entangling Gates Using Geometric Space Curves”. In: *Phys. Rev. Appl.* 19 (4 2023), p. 044094. URL: <https://link.aps.org/doi/10.1103/PhysRevApplied.19.044094>.
- [74] Christian Ventura Meinersen, Stefano Bosco, and Maximilian Rimbach-Russ. *Quantum geometric protocols for fast high-fidelity adiabatic state transfer*. 2024. arXiv: 2409.03084 [quant-ph]. URL: <https://arxiv.org/abs/2409.03084>.

- [75] S. Lloyd and S. Montangero. “Information Theoretical Analysis of Quantum Optimal Control”. In: *Phys. Rev. Lett.* 113 (1 2014), p. 010502. URL: <https://link.aps.org/doi/10.1103/PhysRevLett.113.010502>.
- [76] Matthias M Müller et al. “Information theoretical limits for quantum optimal control solutions: error scaling of noisy control channels”. In: *Scientific Reports* 12.1 (11 Dec. 2022), p. 21405. URL: <https://link.aps.org/doi/10.1103/PhysRevB.111.115305>.
- [77] Lu Hou, Yunfei Shi, and Chaoquan Wang. “The quantum speed limit time of a qubit in amplitude-damping channel with weak measurement controls”. In: *The European Physical Journal Plus* 138.5 (11 May 2023), p. 440. URL: <https://link.aps.org/doi/10.1103/PhysRevB.111.115305>.
- [78] Navin Khaneja, Roger Brockett, and Steffen J. Glaser. “Time optimal control in spin systems”. In: *Physical Review A* 63.3 (11 Feb. 2001), p. 115305. URL: <http://dx.doi.org/10.1103/PhysRevA.63.032308>.
- [79] Xikun Li. *Estimation of optimal control for two-level and three-level quantum systems with bounded amplitude*. 2023. arXiv: 2208.13377 [quant-ph]. URL: <https://arxiv.org/abs/2208.13377>.
- [80] Yang Dong et al. “Fast high-fidelity geometric quantum control with quantum brachistochrones”. In: *Phys. Rev. Res.* 3 (4 2021), p. 043177. URL: <https://link.aps.org/doi/10.1103/PhysRevResearch.3.043177>.
- [81] Yang Dong et al. “Time-optimal control of a solid-state spin amidst dynamical quantum wind”. In: *npj Quantum Information* 10.1 (11 Nov. 2024), p. 108. URL: <https://link.aps.org/doi/10.1103/PhysRevB.111.115305>.
- [82] Ji Bian et al. “Experimental observation of the effect of global phase on optimal times of SU(2) quantum operations”. In: *Phys. Rev. A* 100 (4 2019), p. 042315. URL: <https://link.aps.org/doi/10.1103/PhysRevA.100.042315>.
- [83] Christiane P Koch. “Controlling open quantum systems: tools, achievements, and limitations”. In: *Journal of Physics: Condensed Matter* 28.21 (11 May 2016), p. 213001. URL: <http://dx.doi.org/10.1088/0953-8984/28/21/213001>.
- [84] Tommaso Caneva, Tommaso Calarco, and Simone Montangero. “Chopped random-basis quantum optimization”. In: *Physical Review A* 84.2 (11 Aug. 2011), p. 115305. URL: <http://dx.doi.org/10.1103/PhysRevA.84.022326>.
- [85] Daniel Manzano. “A Short Introduction to the Lindblad Master Equation”. In: *AIP Advances* 10.2 (11 Feb. 2020), p. 25106. URL: <https://doi.org/10.1063/1.5115323>.
- [86] Daniel Greenbaum. “Introduction to Quantum Gate Set Tomography”. In: *arXiv* 111.arXiv:1509.02921 [quant-ph] (11 Sept. 2015), p. 115305. URL: <http://arxiv.org/abs/1509.02921>.
- [87] Zhenyu Cai. “Multi-Exponential Error Extrapolation and Combining Error Mitigation Techniques for NISQ Applications”. In: *npj Quantum Information* 7 (11 May 2021), p. 80. URL: <https://www.nature.com/articles/s41534-021-00404-3>.

- [88] Brian Olson et al. “Basin hopping as a general and versatile optimization framework for the characterization of biological macromolecules”. In: *Adv. in Artif. Intell.* 2012 (11 Jan. 2012), p. 115305. URL: <https://doi.org/10.1155/2012/674832>.
- [89] Ciyou Zhu et al. “Algorithm 778: L-BFGS-B: Fortran subroutines for large-scale bound-constrained optimization”. In: *ACM Trans. Math. Softw.* 23.4 (11 Dec. 1997), 550–560. URL: <https://doi.org/10.1145/279232.279236>.
- [90] Dong C. Liu and Jorge Nocedal. “On the limited memory BFGS method for large scale optimization”. In: *Mathematical Programming* 45.1 (11 1989), pp. 503–528. URL: <https://doi.org/10.1007/BF01589116>.
- [91] Guido Burkard et al. “Semiconductor Spin Qubits”. In: *Reviews of Modern Physics* 95.2 (11 June 2023), p. 25003. URL: <https://link.aps.org/doi/10.1103/RevModPhys.95.025003>.
- [92] Zhenyu Cai et al. “A Silicon Surface Code Architecture Resilient Against Leakage Errors”. In: *Quantum* 3 (11 Dec. 2019), p. 212. URL: <http://dx.doi.org/10.22331/q-2019-12-09-212>.
- [93] N. Rach et al. “Dressing the chopped-random-basis optimization: A bandwidth-limited access to the trap-free landscape”. In: *Physical Review A* 92.6 (11 Dec. 2015), p. 115305. URL: <http://dx.doi.org/10.1103/PhysRevA.92.062343>.
- [94] Vladimír Cerný. “Thermodynamical approach to the traveling salesman problem: An efficient simulation algorithm”. In: *Journal of Optimization Theory and Applications* 45 (11 1985), pp. 41–51. URL: <https://link.aps.org/doi/10.1103/PhysRevB.111.115305>.
- [95] Pradnya A. Vikhar. “Evolutionary algorithms: A critical review and its future prospects”. In: *2016 International Conference on Global Trends in Signal Processing, Information Computing and Communication (ICGTSPICC)*. Vol. 111. American Physical Society, 2016, pp. 261–265. URL: <https://link.aps.org/doi/10.1103/PhysRevB.111.115305>.
- [96] Haozhen Situ and Zhimin He. “Using simulated annealing to learn the SDC Quantum Protocol”. In: *The European Physical Journal Plus* 137.1 (11 2022), p. 115305. URL: <https://link.aps.org/doi/10.1103/PhysRevB.111.115305>.
- [97] Xiangzhen Zhou, Sanjiang Li, and Yuan Feng. “Quantum Circuit Transformation Based on Simulated Annealing and Heuristic Search”. In: *IEEE Transactions on Computer-Aided Design of Integrated Circuits and Systems* 39.12 (11 2020), pp. 4683–4694. URL: <https://doi.org/10.1109%2Ftcad.2020.2969647>.
- [98] Haozhen Situ and Daowen Qiu. “Simultaneous dense coding”. In: *Journal of Physics A: Mathematical and Theoretical* 43.5 (11 2010), p. 055301. URL: <https://doi.org/10.1088%2F1751-8113%2F43%2F5%2F055301>.
- [99] Gaurav Bhole, V. S. Anjusha, and T. S. Mahesh. “Steering quantum dynamics via bang-bang control: Implementing optimal fixed-point quantum search algorithm”. In: *Phys. Rev. A* 93 (4 2016), p. 042339. URL: <https://link.aps.org/doi/10.1103/PhysRevA.93.042339>.

- [100] Ehsan Zahedinejad, Sophie Schirmer, and Barry C. Sanders. “Evolutionary algorithms for hard quantum control”. In: *Phys. Rev. A* 90 (3 2014), p. 032310. URL: <https://link.aps.org/doi/10.1103/PhysRevA.90.032310>.
- [101] Deepak Khurana and T.S. Mahesh. “Bang-bang optimal control of large spin systems: Enhancement of ^{13}C - ^{13}C singlet-order at natural abundance”. In: *Journal of Magnetic Resonance* 284 (11 2017), pp. 8–14. URL: <https://www.sciencedirect.com/science/article/pii/S1090780717302306>.
- [102] Martin Gurtner, Kristian Hengster-Movric, and Zdeněk Hurák. “Green’s function-based control-oriented modeling of electric field for dielectrophoresis”. In: *Journal of Applied Physics* 122.5 (11 Aug. 2017), p. 115305. URL: <http://dx.doi.org/10.1063/1.4997725>.
- [103] Marcin Skotniczny et al. “Complexity of direct and iterative solvers on space–time formulations and time-marching schemes for h-refined grids towards singularities”. In: *Journal of Computational Science* 76 (11 2024), p. 102216. URL: <https://www.sciencedirect.com/science/article/pii/S1877750324000097>.
- [104] Pauli Virtanen et al. “SciPy 1.0: Fundamental Algorithms for Scientific Computing in Python”. In: *Nature Methods* 17 (11 2020), pp. 261–272. URL: <https://link.aps.org/doi/10.1103/PhysRevB.111.115305>.
- [105] Bálint Koczor and Simon C. Benjamin. “Quantum Natural Gradient Generalized to Noisy and Nonunitary Circuits”. In: *Physical Review A* 106.6 (11 Dec. 2022), p. 062416. URL: <https://link.aps.org/doi/10.1103/PhysRevA.106.062416>.